THERMAL CONTRACTION AND CRACK FORMATION

IN FROZEN SOIL

By

Hassan M. AL-Moussawi

A DISSERTATION

Submitted to
Michigan State University
in partial fulfillment of the requirements
for the degree of

DOCTOR OF PHILOSOPHY

Department of Civil and Environmental Engineering

1988

ABSTRACT

THERMAL CONTRACTION AND CRACK FORMATION IN FROZEN SOIL

By

Hassan M. AL-Moussawi

On cooling, frozen soil will contract if it is not constrained. If elastic soil behavior is assumed, a temperature drop of only 2 or 3 deg. C will produce significant tensile stresses with no observable strains. In tension, the soil will creep along with some stress relaxation. The creep deformation includes elastic, delayed elastic, and viscous flow (permanent deformation). The same soil on warming will expand, but the permanent deformation will remain. Subsequent cycles of cooling and warming allow the permanent deformation to accumulate followed by eventual rupture in tension at about one percent strain. During periods of decreasing winter temperatures, thermal contraction will increase tensile stresses creating the potential for crack formation, particularly in partially saturated, weaker frozen surface soils.

Duplication in the laboratory of field conditions responsible for crack formation requires facilities and equipment not available to most researchers. To simplify experimental work, a series of constant strain/stress relaxation tensile tests were conducted at a constant temperature. In addition, limited data were obtained on stress increase as a function of soil cooling rates for the same saturated frozen sand.

Linear thermal contraction/expansion coefficients were determined on duplicate samples so as to permit a more accurate analysis. Preliminary tests on fiber-reinforced sand suggests a technique by which crack formation may be controlled in frozen surface soils.

Crack formation in frozen surface soils may occur under two conditions: rapid cooling (severe winter storm) and contraction giving tensile stresses greater than the frozen soil strength, and the accumulation of permanent strain for a number of thermally induced load cycles leading to rupture at a relatively low total strain, less than one percent. Crack susceptibility will be greatest for partially saturated surface soils with lower tensile strengths, including landfill covers and highway subgrade materials. A numerical example illustrates that cracks propagating unstably through the frozen surface soils may extend deeper than the tensile stresses to which they owe their growth. The study shows that crack prevention will require soil enhancement (reinforcement) which will increase the tensile strength, increase the strain at failure, and reduce post-peak loss of strength.

In The Name of Allah

The Merciful, The Compassionate

"O my Lord! Advance me in knowledge"

To My Wife Hanan,

My Daughter Noor,

And My Son Ahmad

This dissertation is dedicated to my wife, Hanan Ali Alwahab. Without her encouragement, I would not have undertaken a doctoral program. Without her love, understanding, and hard work, completion of this study would not have been possible.

ACKNOWLEDGEMENTS

All praise and thanks are due to Allah, Lord of the Universe, for His merciful divine direction throughout my study.

The writer is deeply indebted to his major Professor, Dr. O. B. Andersland, Professor of Civil Engineering, for his continuous encouragement and assistance, and the time which he devoted most generously to discussions and consultations. Thanks are also due other members of the writer's doctoral committee: Dr. R. K. Wen, Professor of Civil Engineering; Dr. Larry J. Segerlind, Professor of Agricultural Engineering, Dr. T. V. Atkinson, Professor of Chemistry; and Dr. N. Altiero, Professor of Engineering Mechanics.

Thanks are also due the Ministry of Youth, Baghdad, IRAQ; for financial support throughout my study at Michigan State University, and the Division of Engineering Research and the Department of Civil and Environmental Engineering at Michigan State University for providing the instrumentation and materials which helped make this study possible. Thanks also due Mrs. Sun Young Ahn for typing the manuscript.

TABLE OF CONTENTS

LIST OF FIGURES

LIST OF TABLES

LIST OF SYMBOLS

A	a temperature-dependent proof stress evaluated at a strain rate of 1 sec^{-1}
A	cross-sectional area
B	Volumetric coefficient of expansion
C_a	apparent heat capacity of frozen soil
C_i	heat capacity of ice
C_{mi}	mass heat capacity of ice = 2.1 J/g °C
C_{ms}	mass heat capacity
C_p	mass heat capacity
C_s	heat capacity of the dry soil
C_u	heat capacity of the unfrozen water
C_u	uniformity coefficient
C_{vf}	volumetric heat capacity of frozen soil
C_{vu}	volumetric heat capacity of unfrozen soil
D	Diameter
E	Modulus of elasticity
E_i	initial tangent modulus
E_1	modulus of elasticity at 50% strength
F	air-freezing index

G average thermal gradient = 1.8 °C/100m

G shear moduli

G crack extension force

G_0 crack arresting force

G_c crack driving force

I_a Freezing index for the ground surface

I_m imaginary part of complex variable

K_I stress intensity factor

K_{IC} stress fracture toughness

K_r crack growth resistance

L latent heat

L_o length at some reference temperature

L' latent heat of water = 333.7 KJ/kg

L_f latent heat for frozen soil

ΔL change in length

N current no. of cycles

N^* no. of cycles to fracture

P step function (stress distribution)

Q linear stress distribution

R_e real part of complex variable

S specific surface area

S degree of soil saturation

T temperature

T loading time

T absolute temperature

T_0 initial uniform ground temperature

dT/dt temperature gradient

T_I air thaw index

T_i stress prependicular to crack surface

T_S surface temperature

$T(x,t)$ ground temperature at depth x, and time t

$\Delta T = T_2 - T_1$ change in temperature

$U(x,y)$ Airy stress function

V_0 volume at some reference temperature

V_0 mean annual site temperature

V_p compressional wave velocity

V_s shear wave velocity

V_s surface freezing index

ΔV change in volume

$W_u = w_u/w$ ratio of unfrozen to total water content

X frost depth

X_x stress in x-direction

X_y shear in y-direction

X_n component of the prescribed surface stress

Y_y stress in y-direction

Y_n component of the prescribed surface stress

$Z = \omega(\zeta)$ complex variable

a depth of stress distribution on the crack surface

a_0 initial crack length

a_c critical crack length

Δa change in crack length

b crack depth

c heat capacity

d inner diameter

d_{10} particle size at 10% finer

d_{60} particle size at 60% finer

$erf(x)$ error function

$f(s)$ complex function

f_1 complex function

f_2 complex function

k parameter has dimensions of stress and varies with temperature

k thermal conductivity

k_f frozen soil thermal conductivity

k_u unfrozen soil thermal conductivity

l fiber length

m proportionally constant

n dimensionless parameter

n slope of the straight line of logarithmic plot of strain versus time

n dimensionless conversion factor for air index to ground surface index

q amount of heat

r correlation coefficient

r radial distance from crack tip

t time greater than zero

t_R reference time greater than zero

t_B time under load

v displacement in y-direction

w water content

w displacement in z-direction

w_u unfrozen water content

Σ summation

Φ sample diameter (cm)

$\Phi_1(z)$ analytic function of the complex variable z

$\Psi_1(z)$ analytic function of the complex variable z

Ω fiber diameter

$\alpha = V_0/V_s$ thermal ratio

α linear thermal coefficient of expansion

α parameter

α parameter characteristic of soil type

α thermal diffusivity

α_{av} average thermal diffusivity

α_f thermal diffusivity of frozen soil

α_1 parameter

α_2 parameter

α_3 parameter

α_4 parameter

β parameter

β parameter characteristic of soil type

β_1 parameter

β_2 parameter

γ parameter

$\gamma(a/b)$ normalized stress intensity factor

γ_0 instantaneous deformation

γ_0^e instantaneous deformation

γ_0^p plastic deformation

γ_d dry density

γ_I deformation developing over period $0 < t \leq t_{ss}$

γ_{II} deformation developing over period $t_{ss} < t < t_{pr}$

γ_{III} deformation developing over period $t_{pr} < t < t_{fail}$

$\gamma(t)$ deformation which develops with time

δ parameter

ε_t failure strain

ε_x strain component in the x-direction

ε_y strain component in the y-direction

ε_z strain component in the z-direction

ε_t failure deformation

ε_1^m failure strain

ε_{f1} failure strain for 1 cycle

ε_{fn} failure strain for n cycle

$\dot{\varepsilon}$ strain rate

$\dot{\varepsilon}$ reference strain rate taken as 1 sec^{-1}

$\dot{\varepsilon}_R$ corresponding strain rate

η dummy variable

η curvilinear coordinate

θ parameter

θ temperature

θ angle measured from x-axis clockwise

θ_0 $= \cos^{-1}(a/b)$

λ coefficient takes into consideration the effect of temperature changes in the soil mass

μ fusion parameter

ν Poisson's ratio

ξ curvilinear coordinate

ρ density

ρ_2 dry density

σ compressive strength

σ stress on crack surface

σ_{ai} stress

σ_f failure stress

σ_{f1} failure stress for 1 cycle

σ_{fn} failure stress for 1 cycle

σ_i variable stress

σ_{max} maximum uniaxial compressive strength

σ_{max} tensile strength

σ_{net} tensile stress

σ_y stress component

σ_y yield strength

σ_{ys} 0.2% offset yield strength

σ_ξ curvilinear stress

σ_η curvilinear stress

$\sigma_0 = e^{i\theta_0}$ constant

σ_1 uniaxial stress

σ_1 axial creep stress

τ_R residual stress

$\tau_{(x)}$ tensile strength

$\tau^*_{(x)}$ thermal stress

$\tau_{\xi\eta}$ curvilinear shear stress

ω fatigue damage

CHAPTER 1

INTRODUCTION

During periods of decreasing winter temperatures, a reduction in ground surface temperatures will cause thermal contraction with an increase in tensile stresses in frozen soil surface layers. These temperature conditions occur annually in the northern tier of states in the continental U.S., Alaska, Canada, and large areas in Northern Europe and Asia. If elastic soil behavior is assumed, a drop of only 2 or 3 deg. C will generate significant tensile stresses. Soils above the ground water table, with only partial saturation, have lower tensile strengths creating the potential for severe crack formation. These frozen soil conditions are similar to those common for landfill covers, exposed soil liners, and highway subgrade soils in the cold regions of the world. The cracks would be distributed over the ground surface in a pattern such that tensile stresses are reduced below the frozen-soil tensile strength. On landfills, these cracks normally would not be observed because they occur during winter cold periods, may be quickly covered with drifting snow, and may partially close with warmer ground temperatures. Thus, the potential for and actual thermal cracking of landfill covers, exposed clay liners, and highway soil subgrades create expensive maintenance problems and show the need for design techniques which would mitigate the thermal cracking problem.

Ground surface temperatures are determined by air temperatures, heat flow from the interior of the earth, and soil thermal properties. Surface temperatures undergo periodic fluctuations on both a daily and an annual cycle. Thermal contraction and development of tensile stresses in frozen surface soils will be most critical during a period of relatively rapid decrease in temperature, a winter storm. With each cycle of temperature decrease and tensile stress increase, the frozen soil will experience elastic strain, delayed elastic strain, and viscous flow (permanent deformation). Rupture will occur if tensile stresses exceed the frozen soil tensile strength as shown in Chapter 3. The same sample on warming will expand, but the permanent deformation will remain. Subsequent winter storms with cycles of cooling and warming will allow the permanent deformation to accumulate. When the total deformation approaches about one percent strain, close to rupture in tension, a thermal crack is likely to form.

Thermal contraction behavior and tensile strength of frozen soils are dependent on several variables including soil type, ice and mineral volume fractions, temperature, and degree of ice saturation. Cohesion within a given material and adhesion at the interface between two materials provides the forces resisting separation during contraction. The ice matrix formed within the soil pores provides the cohesion. For soils above the water table with partial saturation, the continuity of this ice matrix can be reduced, which in turn reduces the tensile strength. These soils are the most vulnerable to rupture. The presence of clay particles with unfrozen films of water will also reduce the ice content and in turn tensile strength. Tensile tests on saturated frozen sand (Eckardt, 1982) and on saturated frozen silt (Yuanlin and Carbee,

1987) show failure strains ranging from 0.24 to 2.6 percent. At temperatures below about -2 deg. C, the failure strains for frozen silt averaged about 1.1 percent. Tensile strengths were dependent on loading rate with lower strengths reported for lower strain rates, closer to those which might occur in the field during a winter storm.

The mechanics of thermal contraction and cracking responsible for formation of ice wedge-polygons in Arctic areas has been studied in some detail by Lachenbruch (1962, 1963). The theory proposed for explaining the formation of the initial cracks and subsequent cracks leading to growth of an ice wedge has application to the current study. In analyzing the stress prior to fracture, the ground is taken as a homogeneous semi-infinite medium. The crack is generally initiated at the surface or near the ground surface where the greatest tensile stress generally occurs. The crack is propagated toward the interior of the medium where the tensile stress diminishes and ultimately passes into compression. The initial stress components vary only in the direction of crack depth. The crack will be considered as lying in the $y = 0$ plane in a strip, $0 < x < b$, for $x > 0$. The maximum principle stress will be represented by $\tau(x)$, which is directed parallel to the y axis and varies only with x.

Mathematical formulation, to study the stress around the crack tip, was based on the Airy function with utilization of complex variables to solve the differential equation (Muskhelishvili, 1963). This study can be visualized by taking the crack as two parallel lines in an infinite medium, then by pulling the centerline to the outside the shape of the crack will change to an ellipse. Working with the ellipse is difficult mathematically. Hence Muskhelishvili (1963) mapped the ellipse to a more convenient function, a circle. By solving the problem for circular cracks, mapping them back to an ellipse, and taking the limit of the minor axis of the ellipse, the problem is returned to the square one which is two parallel lines of cracks.

To obtain an approximate solution for a semi-infinite medium, the superposition concept was applied to the exact solution of an infinite medium. A complete solution for crack depth, spacing, and horizontal distance for stress relief is dependent on shape of the thermal stress distribution with respect to depth. Both a step function and a linear function for stress distribution are represented, which can be used to solve the complex problem. In the numerical example (Chapter V) a step function appears to describe the cracking phenomena in a frozen cohesionless soil.

The numerical example (Chapter V) shows that after a relatively short period of time and for temperatures typical of mid-winter for Fargo, ND, thermal stresses in the saturated frozen sand are higher than tensile strengths of the same sand to a depth of 30 cm. This indicates that a crack would form and would proceed down into the frozen sand. With the water table at some depth below the surface, in many cases below the frost depth, the granular surface soils will be only partially saturated. Soil tensile strengths are dependent on the degree of ice saturation. A lower soil strength will allow the thermal crack to penetrate to a greater depth. For the numerical example, initial soil temperatures were in the 0 to -15 °C range, hence residual tensile stresses would remain from cooling prior to the winter storm. The addition of these tensile stresses along with lower tensile strengths due to partial ice saturation suggests that the crack would continue down through the frozen sand to the frost line at a depth of 205 cm.

With formation of a crack, tensile stresses would be reduced to a horizontal distance about equal to the crack depth. Fracture theory provides estimates on the magnitude of this stress reduction over the zone of stress relief. Crack spacing will be dependent on this stress reduction and any variation in strength of surficial materials from place to place. All cracks can be visualized as initiating at zones of weakness or "flaws".

Duplication in the laboratory of field conditions responsible for thermally induced loading requires facilities and equipment not available to most researchers. To simplify experimental work, a series of constant strain/stress relation tensile tests were conducted at a constant temperature. In addition, limited data were obtained on stress increase as a function of soil cooling rates for the same saturated frozen sand. Linear thermal contraction/expansion coefficients were determined on duplicate samples so as to permit a more accurate analysis. Preliminary tests on fiber-reinforced sand suggests a technique by which crack formation may be controlled in frozen surface soils.

The thermal contraction and crack formation problem to which this study has been directed, has application to covers and liners for hazardous waste landfills, to highway subgrade soils, and to frozen surface soils for dams, dikes, and other hydraulic structures exposed to severe winter temperature changes. Conclusions from this study, given in chapter VI, involve thermal cracking, crack depth, thermal contraction coefficients, and soil property enhancement. Several recommendations for future research are provided.

CHAPTER II

LITERATURE REVIEW

2.1 Deformation Behavior of Frozen Soils

Mechanical properties determine the behavior of frozen soils under applied tensile forces and loads. Three basic types of deformation are involved: elastic, plastic and viscous flow (creep). A temperature decrease will cause the soil to contract; a subsequent temperature increase will cause the soil mass to expand in volume. The response of the frozen soil will depend on soil type, ice content, degree of ice saturation, dry density of soil solids, and temperature. Rate of loading and time dependent effects will alter the frozen soil response. All these factors, which are reviewed in this section, are relevant to thermal contraction behavior and possible rupture in frozen surface soils.

2.1.1 Thermal Contraction/Expansion Properties

The linear thermal coefficient of expansion is expressed by the relative increase in length with increasing temperature. Thus,

$$\alpha = \frac{\Delta L}{\Delta T\ L_0} \qquad (2\text{-}1)$$

where α is the linear thermal coefficient of expansion, L_0 is length at some reference temperature, and ΔL is the change in length due to a temperature change ΔT from some reference temperature. If the material is isotropic, i.e., exhibits the same thermal expansion in every direction, then

$$\alpha = B/3 \tag{2-2}$$

where B is the volumetric coefficient of thermal expansion.

The volumetric thermal coefficient of expansion is related to the volume of a substance, which in turn is at its minimum value at absolute zero -460 °F (-273.33 °C). This volume is increased as the temperature becomes warmer. The relative increase in volume with increasing temperature is expressed by the volumetric coefficient of thermal expansion. The average volumetric thermal expansion over a temperature interval ΔT is expressed by:

$$B = \Delta V/(\Delta T\ V_0) \tag{2-3}$$

where B is the volumetric coefficient of thermal expansion, V_0 is the volume at some reference temperature, ΔV is change in volume due to a temperature change ΔT from the same reference temperature.

There are many different soil types, each with its own mineral and organic composition. Other factors include crystal orientation within the minerals and texture, which are responsible for a different thermal coefficient of expansion in different directions, Jones, et al. (1968).

Based on convenience, several methods have been used to measure the thermal coefficient, including the dilatometer, optical interferometer, strain gage, and fulcrum-type extensometer. Hooks and Goetz (1964) used the Whittemore strain gage on bituminous concrete for temperatures from +30°C to -30°C. This gage has advantages over the dilatometer in that it is easy to operate and requires little operator experience in order to obtain reproducible results. The Whittemore strain gage was used in this study to determine the coefficient of linear contraction and expansion for frozen Ottawa sand.

2.1.2 Tensile and Compressive Strengths

Frozen soil tensile and compressive strengths depend on several variables including dry density, degree of ice saturation, unfrozen water content, temperature, sample size, rate of loading, and strain rate. The study by Haynes and Karalius (1977) on frozen silt, showed that both compression and tensile strengths depend on temperature, machine speeds (rate of loading), and unfrozen water content. They used two machine speeds, 4.23 cm/sec and 0.423 cm/sec, along with temperatures from 0 °C to -56.7 °C to show that compressive strength increased by about one order of magnitude and the tensile strength increased by one-half an order of magnitude from the warmest to the coldest temperature. For a higher rate of loading they observed a smaller time to failure for both compression and tension tests. Kaplar (1971) showed that strength for soils of normal unit weight with less than 100% saturation always increased with loading rate.

The effect of total moisture content on the unconfined compressive strength of a fine sand at -12 °C and an axial strain rate of 2.2×10^{-6} S^{-1} is shown in Figure (2-1). At low water contents, less than 5%, the sand behavior and strength are similar to those for dry unfrozen sand. Strength increased rapidly with an increase in the ice matrix, approaching a maximum strength value at full ice saturation and maximum dry density. With higher water contents, a decrease in dry density is responsible for a decrease in the unconfined compressive strength. At a moisture content close to 58% the soil particles become suspended in the ice matrix with little or no particle-to-particle contact. The compressive strength is now dependent on the behavior of the ice matrix. A small decrease in strength is noted as the soil particle volume decreases from about 42% at a moisture content of 58% to zero at a moisture content of 100% (Andersland, 1987).

Haynes, et al. (1975) showed that at a temperature of -10°C, the compressive strength for frozen silt is very sensitive to strain rate, increasing ten times over a strain rate range of 1.2×10^{-4} sec^{-1} to 2.9 sec^{-1}. The tensile strength was relatively insensitive with little change indicated.

Bragg and Andersland (1981) found that at strain rates above about 10^{-5} sec^{-1} the compressive strength for frozen sand was essentially independent of strain rate as shown in Figure (2-2). However, at strain rates below 10^{-5} sec^{-1} the compressive strength increased linearly with strain rate according to a power law of the form

$$\sigma_{max} = A\,\dot{\varepsilon}^{1/n} \tag{2-4}$$

where n is the creep parameter, A is a temperature-dependent proof stress evaluated at a strain rate of 1 sec^{-1}, $\dot{\varepsilon}$ is the strain rate (sec^{-1}), and σ_{max} is the maximum uniaxial compressive strength. Values of A and 1/n reported by several investigators for their data are summarized in Table (2-1).

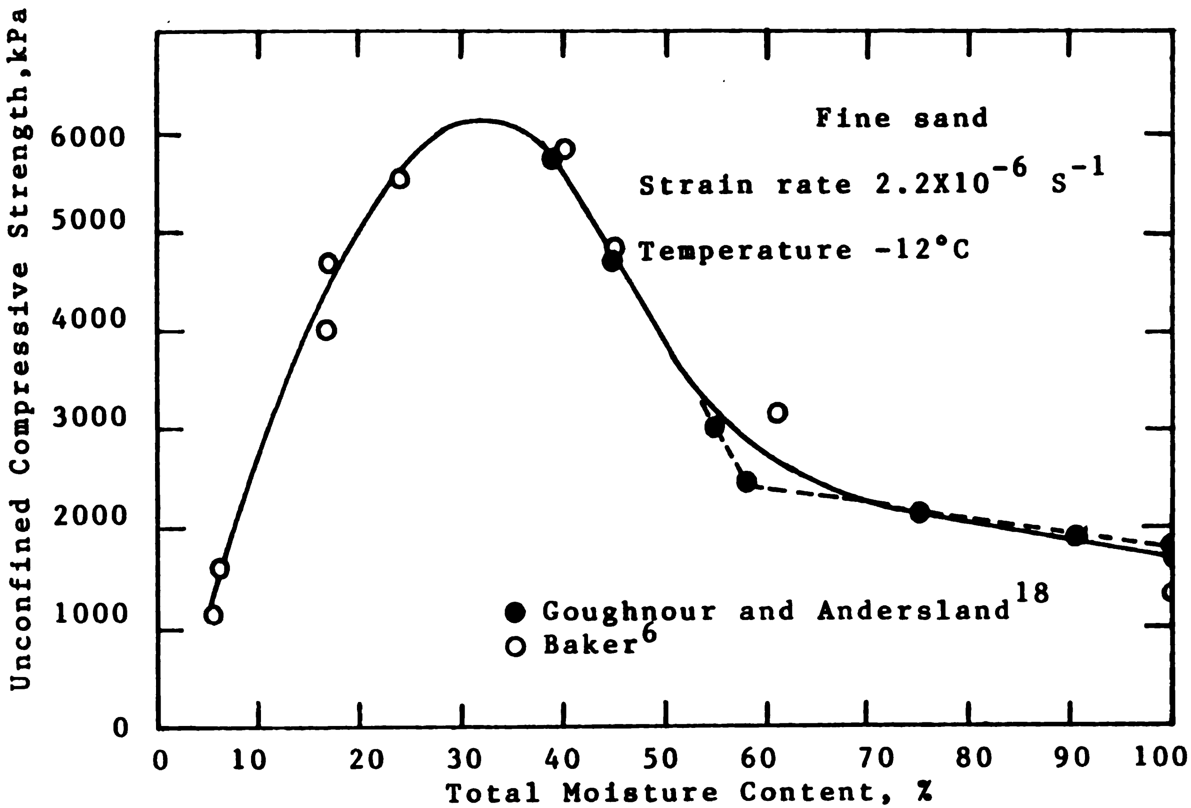

Figure 2-1: Effect of Total Moisture Content on Unconfined Compressive Strength of Frozen Fine Sand at -12 °C (Andersland, 1987).

Table 2-1: Parameter A and 1/n for Equation 2-4 for Silica Sand with Similar Gradation and Density (Bragg and Andersland, 1981).

Temperature (°C)	A	1/n	$\dot{\epsilon}$ (sec^{-1})	Source
-2	341.61	0.303	5×10^{-6} to 8×10^{-5}	Bragg (1980)
-3	—	0.105	1.7×10^{-4} to 2×10^{-2}	Sayles and Epanchin (1966)
-3.85	—	0.10	1.7×10^{-5} to 1.7×10^{-2}	Sayles (1974)
-5.5	28.76	0.09	2×10^{-7} to 2×10^{-3}	Baker (1978)
-6	47.37	0.115	5×10^{-6} to 8×10^{-5}	Bragg (1980)
-6	—	0.073	1×10^{-7} to 1×10^{-2}	Parameswaran (1980)
-6.5	—	0.092	1.7×10^{-4} to 2×10^{-2}	Sayles and Epanchin (1966)
-10	62.31	0.119	5×10^{-6} to 8×10^{-5}	Bragg (1980)
-10	—	0.071	1×10^{-7} to 1×10^{-2}	Parameswaran (1980)
-10	—	0.094	1.7×10^{-4} to 2×10^{-2}	Sayles and Epanchin (1966)
-15	44.31	0.079	5×10^{-6} to 8×10^{-5}	Bragg (1980)
-15	—	0.079	1×10^{-7} to 1×10^{-2}	Parameswaran (1980)

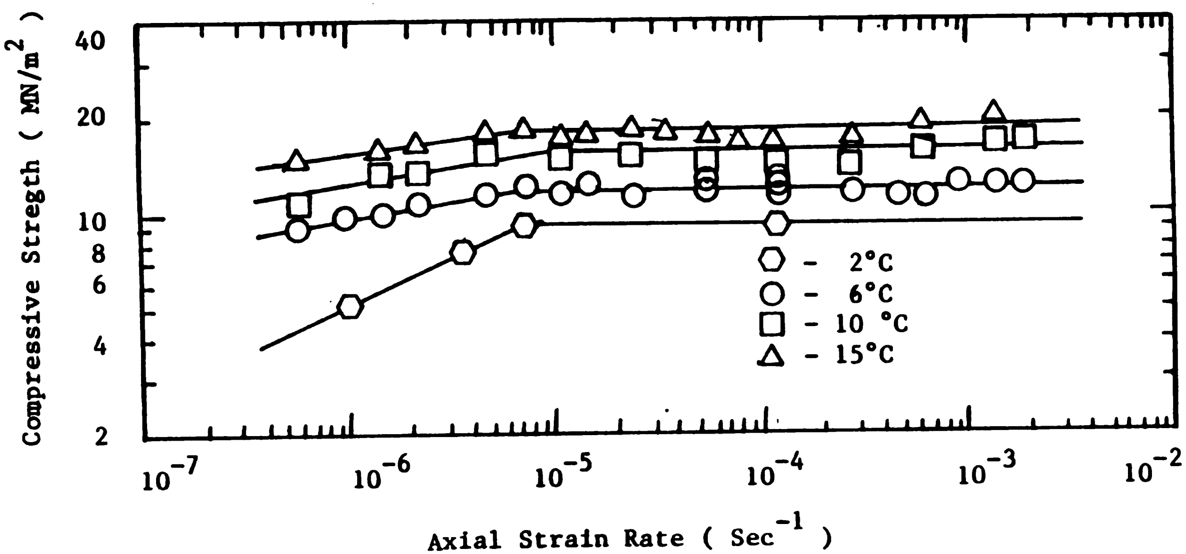

Figure 2-2: Compressive Strength vs. Strain Rate (Bragg and Andersland, 1981).

Bragg and Andersland (1981) gave three equations for the effect of sample size on compressive strength, failure strain and initial tangent modulus for frozen sand. They include the following:

$$\sigma = 12.06 - 0.24\ \Phi \tag{2-5}$$

$$\varepsilon_t = 3.07 + 0.014\ \Phi, \quad \begin{cases} \text{for } T = -6\ ^\circ\text{C and} \\ \dot{\varepsilon} = 1.2 \times 10^{-4}\ \text{sec}^{-1} \end{cases} \tag{2-6}$$

$$E_i = 1.703 + 0.231\ \Phi, \quad \begin{cases} \text{for } T = -6\ ^\circ\text{C and} \\ \dot{\varepsilon} = 1.2 \times 10^{-4}\ \text{sec}^{-1} \end{cases} \tag{2-7}$$

where σ is compressive strength (MN/m^2), ε_t is failure strain (%), Φ is sample diameter in (cm), and E_i is initial tangent modulus (GN/m^2).

Parameters for the above equations were based on the least squares method. It is clear from the above equations that σ, ε_t and E vary linearly with sample diameter while the compressive strength decreased with increasing diameter for both ε_t and E_i. The initial tangent modulus increased with increasing sample diameter.

Peak tensile strength of frozen silt, σ_m, reported by Yuanlin and Carbee (1987), was found to be a function of strain rate, temperature, and density. A simple power-law equation gives σ_m as

$$\sigma_m = k\ (\dot{\varepsilon}/\dot{\varepsilon}_1)^n \tag{2-8}$$

where $\dot{\varepsilon}_1$ is a reference strain rate taken as 1 sec^{-1}, $\dot{\varepsilon}$ is strain rate, n is a dimensionless parameter, and k has dimensions of stress. Both k and n varied with temperature, density, and strain rate. A summary of their values are listed in Table (2-2).

Table 2-2: Values of k and n in Equation 2-8 (Yuanlin and Carbee 1987).

Temperature (°C)	Density (g/cm^3)	Strain Rate $\dot{\varepsilon}$ (S^{-1})	k (kg/cm^2)	n
	1.08 - 1.12	$5 \times 10^{-4} - 5 \times 10^{-7}$	148.6	0.142
-5	1.2 - 1.26	$1 \times 10^{-2} - 1 \times 10^{-5}$	143.4	0.151
		$1 \times 10^{-5} - 6 \times 10^{-8}$	48.6	0.068
	1.36 - 1.41	$1 \times 10^{-3} - 7 \times 10^{-7}$	105.4	0.134
-2	1.20 - 1.26	$1 \times 10^{-2} - 1 \times 10^{-6}$	103.2	0.185

2.1.3 Elastic Properties, E and ν

Linear relations between the components of stress and strain are described by Hooke's law. The modulus of elasticity E is a linear relation between stress and strain, thus

$$E = \frac{\sigma}{\varepsilon} \tag{2-9}$$

where E is modulus of elasticity (F/L^2), σ is stress (F/L^2), and ε is strain (L/L). Strain extension of frozen soils in the X-direction is accompanied by lateral strain (contraction) in both the y, and z directions. This is known as Poisson's effect, which leads to Poisson's ratio ν. For isotropic materials

$$\nu = -\frac{\varepsilon_x}{\varepsilon_y} = -\frac{\varepsilon_x}{\varepsilon_z} \tag{2-10}$$

where

compo

direc

unifo

ratio

Ander

modu

wher

abso

Cels

of p

whe

σ,

ben

Val

wit

hig

str

the

where ε_x is the strain component in the X-direction, ε_y is the strain component in the y-direction, and ε_z is the strain component is the z-direction.

Young's Modulus, E, for frozen soils is many times greater than for unfrozen soils. In frozen soils E depends on soil composition, void ratio, ice content, temperature, and external pressures (Andersland and Anderson, 1978). Tsytovich (1975), introduced an equation for the modulus of elasticity as follows:

$$E = \alpha + \beta\theta + \gamma\theta^2 + \delta\theta^3 \qquad (2\text{-}11)$$

where α, β, γ, and δ are experimentally determined parameters. The absolute value of the negative temperature θ of frozen soil is in degree Celsius. Tsytovich approximated equation 2-11 with a power law equation of the form

$$E = \alpha + \beta\theta^n \qquad (2\text{-}12)$$

where n is a non linear parameter, and β is a function of normal stress σ. For temperatures down to -10°C, n can be assumed equal to unity, hence

$$E = \alpha + \beta\theta \qquad \text{for } \theta \leq -10^\circ C \qquad (2\text{-}13)$$

Values for E decreased with increasing external pressures and increased with decreasing temperatures.

Haynes and Karalius (1977) showed that frozen soils gave their highest modulus for higher machine speeds and consequently lower strains. The modulus values at 50 % strength were slightly lower than the initial tangent modulus. Also, tension tests consistently gave higher

machin

tests.

M

streng

rate,

funct

obser

can b

where

These

using

from

It i

infi

in t

ratio

soil.

Roe

higher modulus values as compared to compression tests, and higher machine speeds produced higher E values for both tension and compression tests.

Yuanlin and Carbee (1987) in their investigation on tensile strength of frozen silt reported on the effects of temperature, strain rate, and density. They showed that the initial tangent modulus E_i is a function of strain rate and temperature. For medium-dense samples, they observed a relation between E_i and the modulus E_1 at 50% strength which can be expressed as

$$E_i = 6.05\ E_1 + 3.26 \times 10^4 \qquad (2\text{-}14)$$

where E_i and E_1 are in kgf/cm^2.

Poisson's ratio for three soils are summarized in Table (2-3). These values were checked by equation

$$\nu = \frac{E}{2G} - 1 \qquad (2\text{-}15)$$

using Young's moduli measured from compression tests, and shear moduli from tension tests on cylinderical frozen specimens (Tsytovich, 1975). It is clear from Table (2-3) that temperature has a significant influence on Poisson's ratio, and that it will decrease with a decrease in temperature (Tsytovich, 1975).

Other methods of finding the modulus of Elasticity and Poisson's ratio involves the use of compressional and shear waves in the frozen soil. Using equation 2-16 values for ν, E, and G may be computed (Roethlisberger, 1972),

Table 2-3: Poisson's Ratio for Frozen Soil (Tsytovich, 1975).

Soil type	Water content %	T Temperature °C	σ Stress kN/m^2	ν Poisson's ratio
Sand (7% pass 0.25mm,	19.0	-0.2	196	0.41
1.4% pass 0.05mm)	19.0	-0.8	588	0.13
Silt (64.4% pass 0.05mm,	28.0	-0.3	147	0.35
9.2% pass 0.005mm)	28.0	-0.8	196	0.18
	25.3	-1.5	196	0.14
	28.7	-4.0	588	0.13
Clay (50 + %pass 0.005mm)	50.1	-0.5	196	0.45
	53.4	-1.7	392	0.35
	54.8	-5.0	1176	0.26

$$\nu = \frac{1}{2} \frac{V_p^2 - 2V_s^2}{V_p^2 - V_s^2} \tag{2-16}$$

where

$$V_p = \sqrt{\frac{E}{\rho} \frac{1-\nu}{(1+\nu)(1-2\nu)}} \quad , \quad V_s = \sqrt{\frac{G}{\rho}}$$

ν is Poisson's ratio, ρ is density, E is modulus of elasticity, G is shear modulus, V_p is compressional wave velocity, and V_s is shear wave velocity.

2.1.4 Time Dependent Effects (Creep)

A material under constant load will deform with time. This phenomenon is called creep. A test carried out at constant load is therefore called a creep test, and the measured strains are called creep strains. The slope of the creep curve (strain versus time) at any point determines the creep rate.

Vyalov (1986), Andersland and Anderson (1978), and Ladanyi (1972), defined creep deformation as the sum of a hypothetically instantaneous deformation, γ_0, which occurs immediately after load application and a deformation which develops with time $\gamma(t)$, thus,

$$\gamma = \gamma_0 + \gamma(t) \tag{2-17}$$

The deformation $\gamma(t)$ associated with the process of creep, is illustrated in Figure (2-3). In addition to instantaneous deformation, creep displays three stages: (I) non-steady state creep (segment AB), (II) steady state flow (segment BC), and (III) progressive flow. During stage I, deformation develops at a decreasing rate and reaches a minimum value. During stage II the deformation rate remains more or less constant, $\dot{\gamma}$ = const; and is sometimes called the stage of viscoplastic flow. At stage III, deformation develops at an increasing rate until failure occurs (brittle or viscous). This final process is referred to as the failure stage.

The duration and effect of any particular stage of creep varies with the soil type and load. Higher loads correspond to a shorter stage II and a more rapid development of failure, stage III. Referring to Figure (2-3) the transition time from stage to stage will be different:

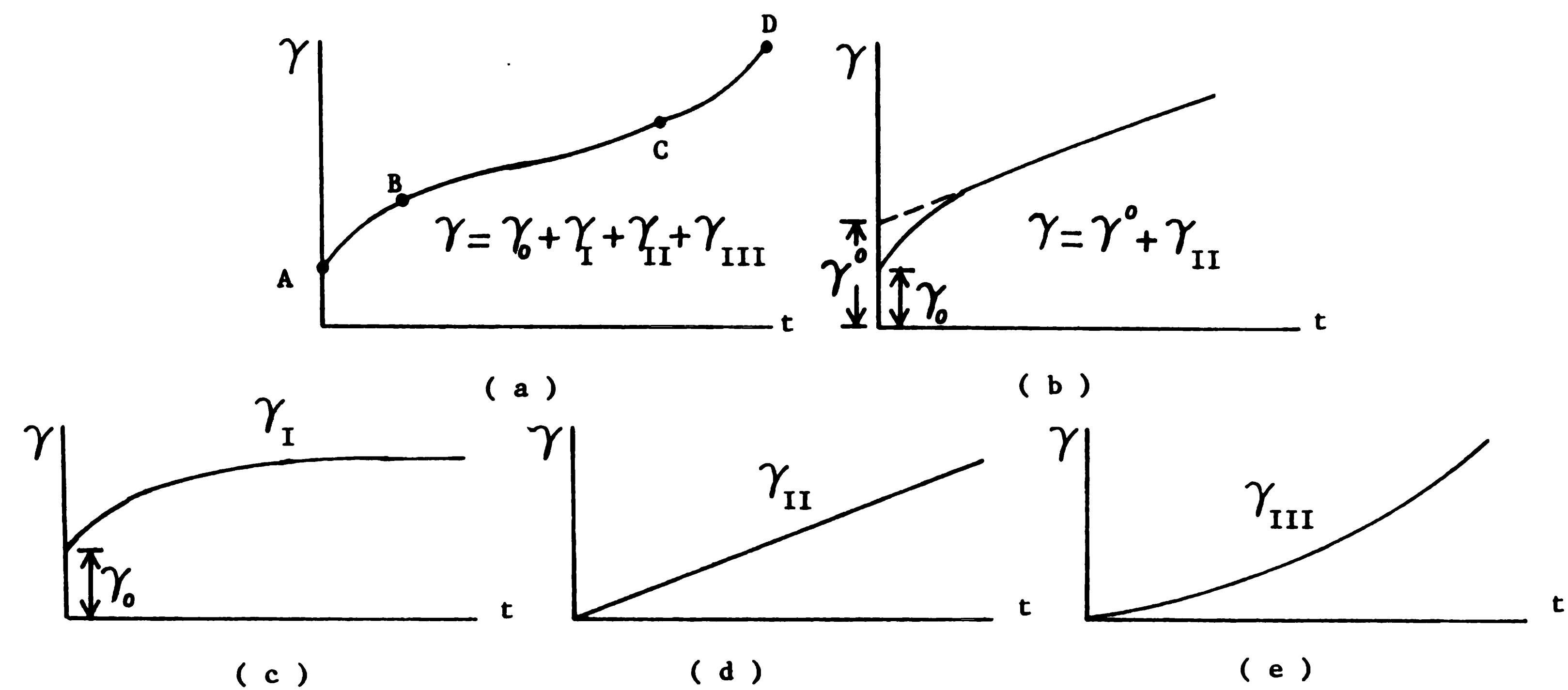

Figure 2-3: (a) Non-attenuating Creep Deformation and (b) Attenuating Creep Deformation as the Sum of the Components; (c) Attenuating Deformation (γ_I); (d) Steady-State Deformation (γ_{II}); (e) Progressive Deformation (γ_{III}), (Vyalov, 1986).

the beginning of steady-state viscoplastic flow is denoted by t_{ss}; the transition to the stage of progressive flow by t_{pr}; and the time of failure by t_{fail}. Soil deformation with time can be represented by the sum

$$\gamma = \gamma_0 + \gamma_I \Big|_{0}^{t_{ss}} + \gamma_{II} \Big|_{t_{ss}}^{t_{pr}} + \gamma_{III} \Big|_{t_{pr}}^{t_{fail}} \qquad (2\text{-}18)$$

where γ_0 is hypothetically the instantaneous deformation which occurs immediately on load application, $t = 0$, γ_I is the deformation developing over the period $0 < t \leq t_{ss}$, γ_{II} is the deformation developing over the period $t_{ss} < t < t_{pr}$, and γ_{III} is the progressive deformation developing over the period $t_{pr} < t < t_{fail}$.

In most cases, it is undesirable to allow soil to operate under the conditions of stage III. Therefore γ_{III} is commonly excluded from the analysis, and creep deformation is considered as the sum of the instantaneous and viscoplastic deformations, thus

$$\gamma = \gamma_0 + \gamma_I + \gamma_{II} \qquad (2\text{-}19)$$

Sayles (1973), reporting on triaxial creep tests on frozen Ottawa sand, found that at low stresses the rate of strain decreased continuously with time such that logarithmic plots of strain versus time data lead to the expression:

$$\dot{\varepsilon} = [\dot{\varepsilon}_R/(t_R)^{1/n}]\ (t)^{1/n} \qquad (2\text{-}20)$$

where $\dot{\varepsilon}$ is the rate of strain at time t greater than zero, $\dot{\varepsilon}_R$ is a corresponding strain rate, t_R is a reference time greater than zero, and n is the slope of the straight line on the plot.

mix

test

the f

give

wher

para

2.1.

the

init

soon

tota

defo

of t

unlo

of a

(seg

Eckardt (1982) studied the creep behavior of frozen soil in uniaxial compression. The lower and upper boundary conditions for his tests on sand and clayey, sandy silt included:

Temperature T:	$-40°C \leq T \leq -5°C$
Time under load t_B:	$1\ h \leq t_B \leq 10{,}000\ h$
Uniaxial stress σ_1:	$-300\ kPa \leq \sigma_1 \leq 10{,}000\ kPa$
Failure deformation ε_f:	$-2\% \leq \varepsilon_f \leq 7\%$
Deformation rate $\dot{\varepsilon}$:	$1 \times 10^{-6}/h \leq \dot{\varepsilon} \leq 5 \times 10^{-3}/h$

He found that creep curves for both compression and tension tests can be given in the form of axial deformation, thus

$$\varepsilon_1^m = \sigma_1/k(T,\ t_B) \qquad (2\text{-}21)$$

where σ_1 is the axial creep stress, m is a material constant, and K is a parameter dependent on temperature T, and t_B is the loading time.

2.1.4.1 Recoverable and Residual Deformation

When a soil specimen is unloaded, as shown in Figure (2-4), some of the deformation will be of the recoverable kind. This recovery, from an initial hypothetically instantaneous deformation γ_0, is initiated as soon as the load is removed and proceeds until the deformation is either totally or partially gone. Total recovery is the case when the initial deformation is of the purely elastic type, $\gamma_0 = \gamma^e$, so that segment 0-2 of the loading curve in Figure (2-4) is the same as segment 3-4 of the unloading curve.

Partial recovery takes place when the initial deformation consists of an elastic deformation (segment 0-1), and a plastic deformation (segment 1-2),

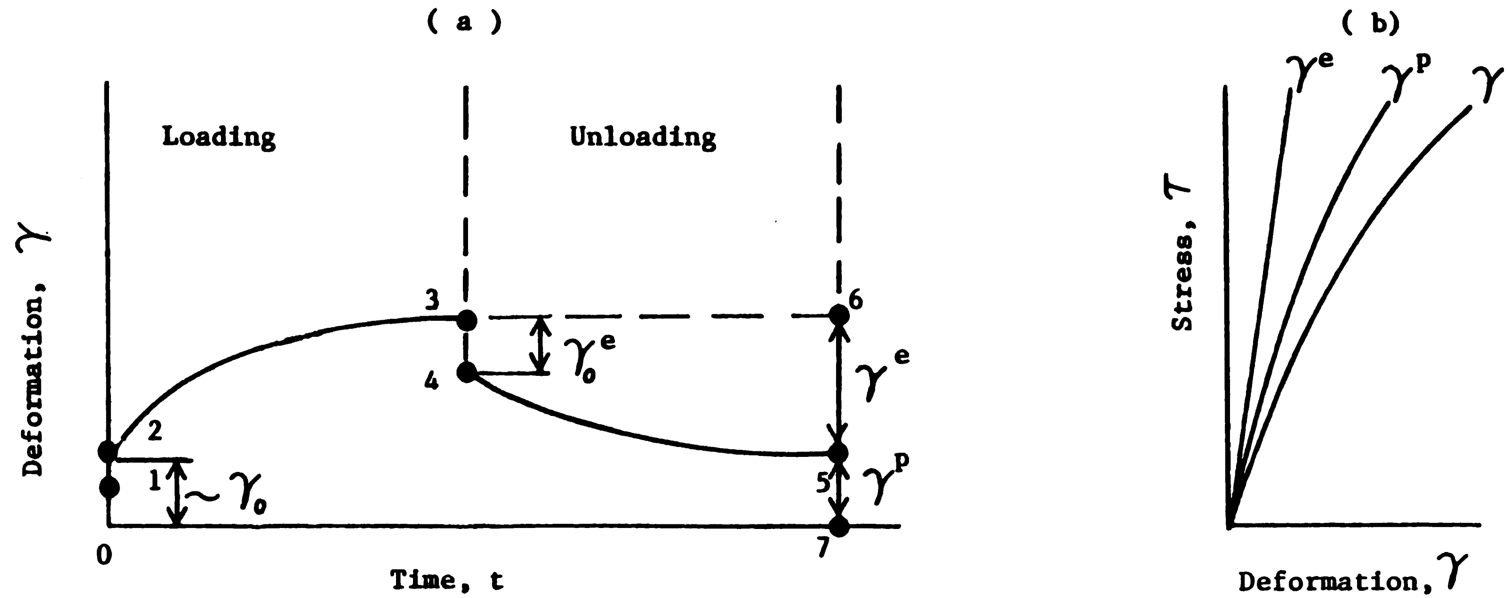

Figure 2-4: Recoverable, γ^e, and Residual γ^p, Components of Deformation as Presented on (a) The Creep Curve and (b) The Stress-Deformation Graph (Vyalov, 1986).

$$\gamma_0 = \gamma_0^e + \gamma_0^p \tag{2-22}$$

Consequently, the body recovers only from the elastic deformation γ_0^e.

The recovery from deformation γ_I in Figure (2-4) takes place only partially with time (segment 4-5), the deformation consisting of an elastic segment γ_I^e (segment 5-6), and a plastic after effect γ_I^p (segment 5-7), thus

$$\gamma_t = \gamma_I^e + \gamma_I^p \tag{2-23}$$

The deformation at stage II and III, the steady-state and progressive flow, respectively, are plastic and totally irrecoverable, thus

$$\gamma_{II} = \gamma_{II}^p \qquad \text{and} \qquad \gamma_{III} = \gamma_{III}^p \tag{2-24}$$

In general, soil creep deformation at any time t consists of a recoverable deformation and a residual deformation Vaylov (1986).

$$\gamma_0 = \gamma^e + \gamma^p \tag{2-25}$$

2.1.4.2 Fatigue Damage Accumulation

In a body subjected to cyclic loading, the process of fracture starts with microcracks nucleating and growing at the initial stage of the process. Then, macrocracks begin to form and propagate, which ends in fracture of the body. For a body with considerable initial defects (such as notches, cracks, and/or inclusions) the early ("latent") stage of fracture may be very short or even non-existent. The relation between time for the latent stage and time for macrocrack propagation depends on the geometry of the body and on the nature of defects. The time for crack growth may include 10 to 80 percent of the service life of the specimen. If the body is sufficiently homogeneous, and there is no stress concentration, the latent period may be quite long. It is difficult to estimate damage accumulation in the latent stage. It is also difficult, as a rule, to determine the initial time for macrocrack formation.

In fatigue theory, damage accumulation is usually considered with respect to the entire fracture process without distinguishing the stage of fatigue (Kachanov, 1986). In tests with uniform load cycles the cumulative effect eventually produces fatigue failure, unless the load is below the prevailing fatigue limit. When loading and unloading doesn't occur in uniform cycles but in an irregular manner, the cumulative effect of these events may also produce fatigue failure. The term "cumulative damage" refers to the fatigue effects of loading events other than uniform cycles (Fuchs and Stephens, 1980).

Fatigue damage is defined as

$$\omega = N/N^* \qquad (2\text{-}26)$$

where N is the current number of cycles, and N^* is the number of cycles to fracture. Under conditions of cyclic loading, the analysis can generally be based on the principle of a linear summation of damage. This principle, as applied to fatigue fracture, was formulated by Palmgren in 1924 and by Miner in 1945. The percent damage already done to the sample or fraction of life used at a certain stress level can be formulated by

$$\text{Cycle Ratio} = \frac{2N_i}{2N_{fi}} = \frac{\text{Reversals applied at } \sigma_{ai}}{\text{Reversals to failure at } \sigma_{ai}} \tag{2-27}$$

which equals the fraction of life used at σ_{ai}.

Failure (Kachanov,1986; Fuchs and Stephens, 1980) occurs when

$$\sum_i \frac{2N_i}{2N_{fi}} = 1 \tag{2-28}$$

2.2 Frozen Soil Thermal Properties

Thermal properties of frozen soil play an important role in their mechanical behavior. Thermal conductivity, latent heat, apparent heat capacity, and thermal diffusivity are essential in heat flow calculations involving frozen soils. Thermal properties of a frozen soil are not constant, but are a function of temperature, dry density or porosity, water content, mineral composition, additives, organic factors, and direction of heat flow.

2.2.1 Unfrozen Water Content

The amount of frozen and unfrozen water in soil has a significant effect on thermal conductivity and the specific heat of frozen soil. Unfrozen water will reduce the tensile strength of frozen soil by reducing the ice content and by creating weak zones adjacent to the soil particles.

Anderson and Tice (1972) predicted the unfrozen water content w_u such that

$$w_u = f(S, \theta) \tag{2-29}$$

where S is specific surface area (m^2/g) and θ is the temperature in degrees below zero degrees Celsius (32°F). Anderson et al. (1973) proposed an equation for prediction of unfrozen water contents as

$$w_u = \alpha\theta^{\beta} \tag{2-30}$$

where w_u is the unfrozen water content, α and β are parameters characteristic of each soil type (Table 2-4), and θ is the temperature in degrees Celsius below zero.

The values of α and β obtained by Anderson et al. (1973) was a function of specific surface areas for each soil. They found that

$$\ln \alpha = 0.5519 \ln S + 0.2618 \tag{2-31}$$

with a correlation coefficient of 0.90 and,

$$\ln (-\beta) = -0.2640 \ln S + 0.3711 \tag{2-32}$$

with a correlation coefficient of 0.86. This gives the expression for w_u as

$$\ln w_u = 0.2618 + 0.5519 \ln S - 1.449 S^{-0.264} \ln \theta \tag{2-33}$$

or

$$w_u = \mathrm{Exp}\left[0.2618 + 0.5519 \ln S - 1.449 S^{-0.264} \ln \theta\right] \tag{2-34}$$

Equations 2-30, 2-31, and 2-32 are utilized in Chapter V to compute the unfrozen water content in frozen soil.

Table 2-4: Experimental Values for α, β, Specific Surface Areas S and Correlation Coefficients r (Anderson et al., 1973).

Soil	Surface Area S = m^2/g	α	β	r
Basalt	6	3.45	-1.13	0.96
Rust	10	11.05	-0.80	0.96
West Lebanon gravel				
< 100 μ	18	3.82	-0.64	0.94
Limonite	26	8.82	-0.83	0.99
Fair banks silt	40	4.81	-0.33	0.96
Dow field silty clay	50	10.35	-0.61	0.94
Kaolinite	84	23.80	-0.36	0.90
Suffield silty clay	140	13.92	-0.31	0.98
Hawaiian clay	382	32.42	-0.24	0.93
Wyoming bentonite	800	55.99	-0.29	0.72
Umiat bentonite	800	67.55	-0.34	0.83

2.2.

thro

grad

Thus

wher

(m^2)

elem

wate

vapo

dete

unfr

soil

and

wher

and

Aver

V, t

2.2.2 Thermal Conductivity

Thermal conductivity is the amount of heat passing per unit time through a unit cross-sectional area of the soil under a unit temperature gradient applied in the direction of heat flow (Farouki 1981, 1982). Thus

$$k = \frac{q}{A\,(T_2 - T_1)/L_0} \qquad (2\text{-}35)$$

where k is thermal conductivity (W/m °C), A is cross-sectional area (m^2), $\Delta T = (T_2 - T_1)$ is drop in temperature (°C), L_0 is length of the element (m), and q is the amount of heat in (W).

In general, thermal conductivity of soil depends on its density, water content, mineralogical composition, temperature, solid, liquid, vapor constituents, and the state of the pore water. Kersten (1949) has determined the thermal conductivity for a wide range of both frozen and unfrozen soils at different water contents. Thus for unfrozen-sandy soils

$$k_u = 0.1442\,[0.7 \log w + 0.4]\; 10^{0.6243\gamma_d} \qquad (2\text{-}36)$$

and for frozen-sand soils

$$k_f = 0.01096\;(10)^{0.8116\gamma_d} + 0.00461\;(10)^{0.9115\gamma_d}\, w \qquad (2\text{-}37)$$

where k is thermal conductivity (W/m °K), γ_d is soil density (g/cm^3), and w is water content.

Average values given by equation 2-36 and 2-37 will be used in Chapter V, to compute frost depth penetration, and ground temperatures.

2.2.3 Latent Heat

Heat energy that is released or absorbed when a material undergoes a change of phase is called latent heat. It is expressed by the number of calories of heat required to effect a complete change of one gram of the material from one phase to another. Thus, for frozen soil

$$L = \rho_d \, wL' \qquad (2\text{-}38)$$

and for partially frozen soil

$$L = \rho_d \, w(1-W_u)L' \qquad (2\text{-}39)$$

where $W_u = w_u/w$ is the ratio of unfrozen to total water content of the soil, L is latent heat of fusion (J/m^3), L′ is latent heat of water (333.7 kJ/kg), ρ_d is dry density of the soil (kg/m^3), w is the soil water content (percent by weight of solids), and w_u is the unfrozen water content (percent by weight of solids).

2.2.4 Apparent Heat Capacity

The unfrozen water content decreases exponentially with temperature, gradually releasing latent heat and continuously changing the heat capacity (Johansen and Frivik, 1980). To account for this change the heat capacity of frozen soil can be expressed as the sum of the heat capacities of the main constituents. In frozen soils the liquid-solid phase change is gradual and continual with change in temperature, therefore the term specific heat capacity is not appropriate. Use of apparent heat capacity is more appropriate. Therefore, the apparent heat capacity can be expressed as the sum of an appropriate term for each of these factors plus a term to account for the latent heat of phase change that is continually being given off or absorbed. Thus

$$C_a = C_s + C_i\,(w-w_u) + C_u\,w_u + \frac{1}{\Delta T}\int_{T_1}^{T_2} L\,\frac{\partial w_u}{\partial T}\,dT \qquad (2\text{-}40)$$

where C_a is the apparent heat capacity of frozen soil, C_s is the heat capacity of the dry soil matrix, C_i is the heat capacity of ice, C_u is the heat capacity of the unfrozen water, w is the total water content, w_u is the unfrozen water content, T is temperature, and L is latent heat of the liquid-solid phase change (Hoekstra, 1969).

Volumetric heat capacity is the energy required to raise the temperature of a unit volume of soil by 1°C. For unfrozen soil

$$C_{vu} = \gamma_d\,[C_{ms} + C_{mw}\,w/100] \qquad (2\text{-}41)$$

for frozen soil

$$C_{vf} = \gamma_d\,[C_{ms} + C_{mi}\,w/100] \qquad (2\text{-}42)$$

and for partially frozen soil

$$C_{vf} = \gamma_d\,[C_{ms} + C_{mi}\,(1+W_u)\,w/100] \qquad (2\text{-}43)$$

where $W_u = w_u/w$ is the ratio of unfrozen to total water content, C_{ms} is the mass heat capacity of soil solids (0.71 J/g °C), C_{mw} is the mass heat capacity of water (4.1868 J/g °C), C_{mi} is the mass heat capacity of ice (2.1 J/g °C), and γ_d is dry density of the solids (g/cm^3).

Kay and Goit (1975) found that the mass heat capacity varies linearly with temperature from -73°C to +27°C (200 to 300°K). Their measurements showed that

$$C_{ms} = C_p = mT \tag{2-44}$$

where $C_m = C_p$ is the mass heat in cal/°Kg, m is a proportionally constant, and T is absolute temperature in °K. They found that specific heat decreased with decreasing temperature over their range of temperature measurement. Table (2-5) shows some typical values for C_p.

Table 2-5: Correlation between Mass Heat and Temperature for Representative Soil Materials (Kay and Goit, 1975).

Material	Equation	Correlation coefficient
Clay-Na bentonite	$C_p = 8.4 \times 10^{-4}\ T - 0.342$	0.984
Sand-Sauble Beach	$C_p = 5.2 \times 10^{-4}\ T + 0.0247$	0.970
Silt-Conestogasilt loam	$C_p = 4.9 \times 10^{-4}\ T + 0.0369$	0.995
Peat-Sphagnum 41% fiber	$C_p = 1.15 \times 10^{-3}\ T - 0.0245$	0.986
Ice	$C_p = 1.76 \times 10^{-3}\ T + 0.0228$	0.999

2.2.5 Thermal Diffusivity

Thermal diffusivity is the ratio of thermal conductivity k to volumetric heat capacity ρc. Thus

$$\alpha = k/\rho c = k/c_v \tag{2-45}$$

where α is thermal diffusivity (m^2/s), ρ is density (kg/m^3), k is thermal conductivity (W/m °C), C is mass heat capacity (J/kg °C). For unfrozen soil

$$\alpha_u = k_u/C_{vu} \tag{2-46a}$$

and for frozen soil

$$\alpha_f = k_f/C_{vf} \tag{2-46b}$$

where the subscript u, and f refer to unfrozen and frozen soil, respectively.

Knowledge of the thermal diffusivity of frozen soils is necessary for transient heat transfer analysis. Haynes et al. (1980), reported a thermal diffusivity for a number of soils, over a range of temperatures, and water contents as summarized in Table (2-6).

2.3 Thermal Contraction Cracks in Frozen Surface Soils

Temperatures at the earth's surface fluctuate on the order of 25°C about the mean through the combined effects of changing seasons, and shorter period random and diurnal changes. More than 90 percent of this fluctuation is confined to the surficial 10 m. For Alaska, all of Canada, and the Northern tier of states of the U.S., daily mean air temperatures will drop below freezing for periods of weeks during the

Table 2-6: Thermal Diffusivity for three soil types (Haynes et al., 1980).

Sample	Water content %	Temperature (°C)				
		-50	-35	-20	-5	20
		Thermal diffusivity, $cm^2/s \times 10^{-3}$				
20-30 Ottawa	0.01	3.02*	2.85	2.88+	2.73	2.81*
sand	8.8	13.17*	11.77	12.45	—	—
	3.0	3.37*	3.19	3.30	3.10	3.03*
Fair banks	17.0	9.49*	8.22	7.78	6.79*	—
silt	25.0	—	10.05	10.02	8.04*	—
	1.8	3.14	2.91	2.76	2.66	2.33*
CRREL varved	18.9	8.26*	8.21	7.44	6.22*	-
clay	25.5	12.19*	11.24	10.33	8.76	-

* Extrapolated

\+ For example 2.88×10^{-3}

winter season. The surface soil strata will freeze to depths of 2 m or more. When temperatures fall in the winter, these surface layers "try" to contract but they are constrained by the tensile strength of the frozen soil. The surface layers are stretched in a sense, although no observable displacements occur. Because frozen soil is relatively weak in tension, initial fracturing commences at the ground surface and penetrates the ground to the depth needed to relieve the tensile stresses. The cracks will be distributed over the ground surface in a pattern such that tensile stresses are reduced below the frozen soil tensile strength.

2.3.1 Origin of the Cracks

When the ground surface is cooled it would contract if it were not constrained. As it cannot contract, horizontal tensions are generated with small horizontal strains. The horizontal thermal strain is calculated as the product of the contraction coefficient and the change in temperature from its initial value. It is the stress produced by this stretching and not the strain that determines whether cracking will occur. Frozen soil materials behave elastically in response to rapid deformation. If elastic behavior is assumed in response to slower natural thermal deformations, the stress would be proportional to the drop in temperature from some reference value. Then using elastic soil constants, stresses on the order of the soil tensile strength would develop in ice-saturated soil when the temperature drops only 2 or 3°C, and open cracks would occur with a horizontal spacing no greater than the crack depth (Lachenbruch, 1962). Since this does not generally happen, it is apparent that frozen soil behavior is more complex and involves time dependent effects as outlined in section 2.3.2.

From the above comments on thermal stress, it is clear that both low temperatures and rapid cooling rates favor large tensile stresses. Since both of these quantities will attain greater extremes at the ground surface, the greatest thermal tensions will normally develop at the ground surface. It follows that repeated contraction cracks would be initiated at the ground surface. This behavior is reported by Lachenbruch (1962) for thermal cracks in permafrost. The original cracks (Figure 2-5a) that start ice-wedges and determine their location are initiated at the ground surface. With the approach of warmer seasonal temperatures, water seepage fills the cracks and freezes. Any remains of the crack in the surface thawed layer will disappear during the summer. The process will repeat itself the following fall with the crack forming in the weaker ice formed in the crack from the previous season. For this case, crack initiation occurs below the surface in the ice. For each subsequent season the lateral dimensions of the ice wedge will grow as more and more ice accumulates in the permafrost (Figure 2-5c and 2-5d). In temperate regions with warmer mean annual temperatures, the ice wedge will not form.

2.3.2 Stresses Before And After Fracture

In analyzing the stress prior to fracture, the ground is assumed to be a homogeneous semi-infinite medium. The ground temperature, with reference to the mean annual temperature as zero, is used to provide a relation between horizontal stress and temperature. Information required includes: (a) ground temperature as a function of air

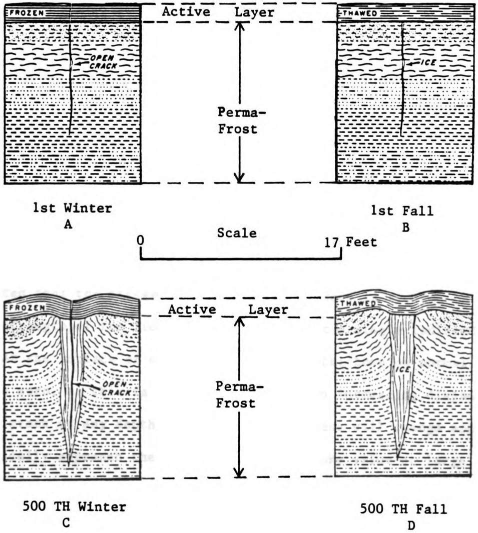

Figure 2-5: Schematic Representation of the Formation of an Ice Wedge According to the Contraction - Crack Theory. Width of Crack Exaggerated for Illustrative Purposes (Lachenbruch, 1963).

temperatures, time, and depth; (b) the thermal contraction coefficient as a function of temperature; and (c) mechanical properties of the frozen soil as a function of temperature. Assuming the simplest model of deformation, the elastic solution for stress gives

$$\sigma = - \frac{E}{1-\nu} \alpha \Delta T \tag{2-47}$$

where σ is the tensile stress at a given depth, E is Young's modulus, ν is Poisson's ratio, α is the coefficient of thermal contraction, and ΔT is the change in temperature.

Prior to fracture the stresses will be the same from place to place at a given depth and time. After crack formation there will be a reduction in tensile stress in its vicinity. These cracks must be so distributed that the stress over the entire surface is reduced below the tensile strength of the frozen ground. Consider a single isolated crack. At the surface of the crack the horizontal tension normal to the strike is zero, as this is a free surface. With increasing distance from the crack at any depth, the horizontal stress will change and asymptotically approach the initial or prefracture value at large distances. Each crack has associated with it a zone of influence or stress relief. Throughout this zone the stresses are reduced well below the tensile strength and no further cracking would occur. Beyond the zone of stress relief the stresses near the ground surface will still exceed the frozen soil tensile strength and other cracks would be expected to occur. The spacing of the cracks are related to the width of the stress relief zone for a single fracture. This question will be examined in greater detail in section 5.2.3.

2.3.3 Crack Depth and Spacing

Up to this point it has been assumed that cracks will initiate if and when the tensile stress exceeds some critical value - the tensile strength. Lachenbruch (1961) has used fracture mechanics theory to provide a more complete picture of crack formation in frozen soils. Energy is required to lengthen a crack, first to overcome the forces of cohesion to produce new surfaces, and second, in a brittle-plastic medium, to do work of plastic deformation in the region of elevated stress near the crack tip. At the same time, when a tension crack lengthens, it relieves some of the tension that produced it, hence strain energy is released from the medium. A crack will lengthen if, and only if, by so doing it releases at least as much (strain) energy as it consumes near the crack tip.

In a frozen soil under uniform tension, the amount of strain energy (G) released with the creation of one square centimeter of crack surface increases with the length of the crack and the tensile stress. As the tensile stress is increased in a brittle-plastic medium, a value of (G) is reached at which small flaws in the frozen soil start to grow and coalesce to form minute cracks. The growing cracks release more strain energy with increase in length, but at the same time, the size of the plastic zone near the tip grows, and so does the energy consumption. When the rate of energy consumption overtakes the rate of energy release, crack growth stops. This process is called "stable cracking" because it is self arresting.

As cracks continue to lengthen stably in a brittle-plastic material, the increase in plastic-zone size becomes less important, and a crack length is reached at which the rate of energy release is growing faster than the rate of energy consumption with increasing crack length. At this point the crack will extend with no further increase in tensile stress, and "unstable" fast fracture begins. The stress at which small cracks attain this critical length in uniformly stressed frozen soil is called the "tensile strength". This condition is identified with a critical value of the rate of strain energy release (or consumption) per square centimeter and is denoted by G_c. If the rate of energy release (G) for a given crack is less than G_c, propagation, if it occurs, will be slow and stable; if it is greater, excess energy is available to accelerate crack extension to cause fast fracture.

At what depth does the crack stop? The crack will stop at that depth at which the rate of energy release ceases to exceed the rate of energy consumption near the crack tip; or about the depth where G falls to G_c. Crack depth is a function of stress on the crack surfaces, and stress intensity factors, thus

$$b = f\ (K_I, \sigma) \qquad (2\text{-}48)$$

where b is crack depth, K_I is stress intensity factor, and σ is stress on the crack surfaces. Due to non linearity of stress distribution on the crack surface, a combination of methods (Sih 1973; Koiter, 1965; Lachenbruch, 1962) are used in evaluating the stress intensity factor K_I as will be shown in Chapter IV.

Crack spacing depends primarily on how the tensile stresses are reduced along the horizontal surface and away from the crack. Crack spacing is a function of horizontal distance from the crack, crack depth, and stress magnitude and distribution along the crack surface. Calculations for crack spacing will be shown in Chapter V along with a numerical example.

CHAPTER III

PRELIMINARY EXPERIMENTAL WORK

3.1 Thermal Contraction/Expansion Behavior

3.1.1 Materials and Preparation of Beam Specimens

A commercially available Silica Sand (produced by UNIMIN Corporation, Oregon, Illinois 61061, U.S.A) used for the experimental study was evaluated relative to its thermal contraction/expansion behavior in the frozen state. The sand consisted of sub-angular quartz particles with a specific gravity of 2.65. The samples were prepared so that the sand gradation was uniform in size with all material passing the number 30 U.S. standard sieve (0.590 mm) and retained on the number 200 sieve (0.074 mm). The coefficient of uniformity ($C_u = d_{60}/d_{10}$) was approximately 1.51.

A wooden mold, 12 inches (304.8 mm) long by 2.5 inches (63.5 mm) wide by 2 inches (50.8 mm) high, Figure (3-1), was used to prepare the samples. The mold was first sealed by placement of high vacuum grease along the edges, then water was poured into the mold. Sand was placed into the water to first remove all air bubbles, then the sides were tapped to give the desired sand density.

After preparation of the unfrozen sample, the next step involved drilling partial holes at each end for placement of steel gage plugs. The holes were carefully located on the top of the compacted beam, using

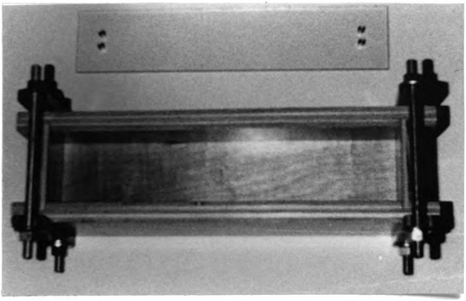

(a)

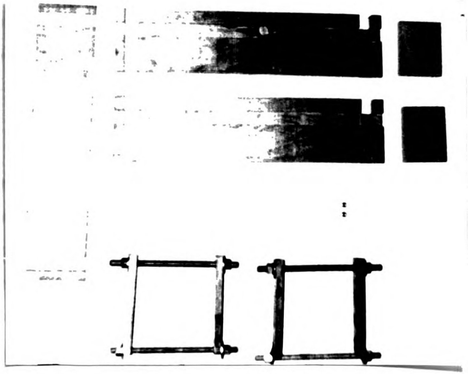

(b)

Figure 3-1: Beam Mold and Template for Preparation of Contraction/Expansion Specimens.

the template shown in Figure (3-1), to give two 10 inch (254 mm) gage lines centered 1 inch (25.4 mm) from each end, and 0.75 inch (19.05 mm) from the edge of the beam. Holding the template firmly in place on the beam, the gage plugs were inserted into the hole and tapped lightly into the surface of the sand. The template was then removed.

The mold, sand, and steel plugs were then placed into the freezer and frozen at a temperature close to -5°C (23°F). After 24 hours the sample was removed from the mold, placed on the wooden rollers shown in Figure (3-2), and returned to the freezer. Gage length and temperature readings were taken immediately and at appropriate intervals as the frozen beam was allowed to slowly cool down to -30 °C (-22 °F). The 9 mm diameter wood rollers provided a very low friction support during contraction and expansion. Gage and temperature readings were continued as the sample was permitted to slowly return to -5 °C (23 °F). One cycle of readings was completed in about 2.5 days.

3.1.2 Equipment and Test Procedures

Dimensional changes of the frozen sample caused by a change in temperature were measured using a Whittemore strain gage. This gage is a mechanical device employing a dial gage with no internal multiplication of the measured deformation. For this investigation, a 10 inch (254 mm) gage length and a least gage reading of 0.0001 inch (2.54×10^{-3} mm) gave a strain sensitivity of 0.00001 inch/inch (2.54×10^{-4} mm).

The gage and accessories are shown in Figure (3-3). The frame and bar on which the gage is mounted serves as a reference between readings.

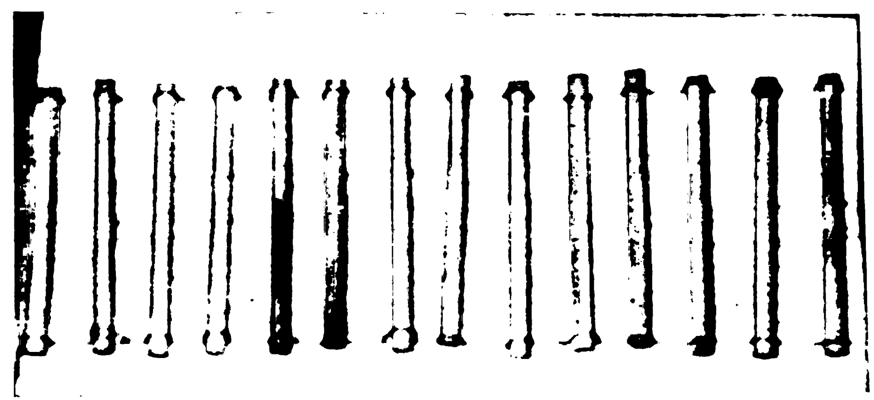

Figure 3-2: Low Friction Beam Support Consisting of 9 mm Diameter Wood Dowels Placed on a Styrofoam Board.

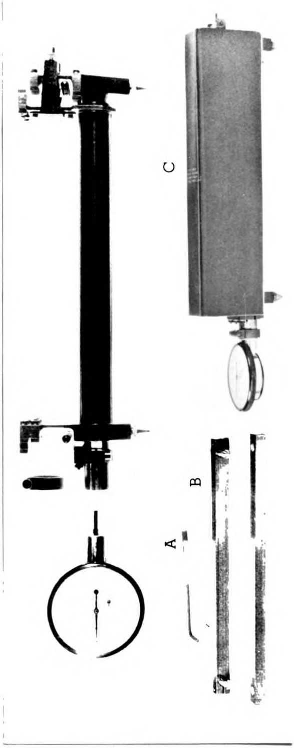

Figure 3-3: The 10-Inch Whittemore Strain Gage.

A standard separate frame is used for establishing the correct gage length on the specimens.

The testing technique involved placement of the standard bar and gage in the cold box adjacent to the frozen samples so that a uniform temperature was maintained throughout the investigation. Before taking a measurement, the gage was checked against the appropriate standard bar followed by a series of three readings obtained for the left and right sample gage plugs. The gage points were then gently inserted into a set of the steel gage plugs and the reading taken. This procedure was repeated three times for each gage line, removing and replacing the gage for each consecutive reading. It was important that the gage be held vertical and that a gentle tap be given the dial gage to ensure that consistent readings were obtained.

Temperatures were monitored using two thermistors (type 100 OHM Platinum RTD .00385 T.C. produced by Pyromation Inc.) embedded, prior to freezing, in the sample near its mid-section. The thermistors where monitored using a Minitrend 205 data logger produced by Doric Scientific, San Diego, California.

Measurement of dimensional changes was repeated at selected temperatures with the length change of the specimen given by the difference between initial and consecutive readings. These results were then plotted as shown in Figure (3-4).

3.1.3 Thermal Contraction Coefficients

Thermal contraction/expansion tests on (1) saturated sand, (2) partially saturated sand, (3) drained partially saturated sand, and (4) snow, showed that an increasing percentage of ice saturation increased

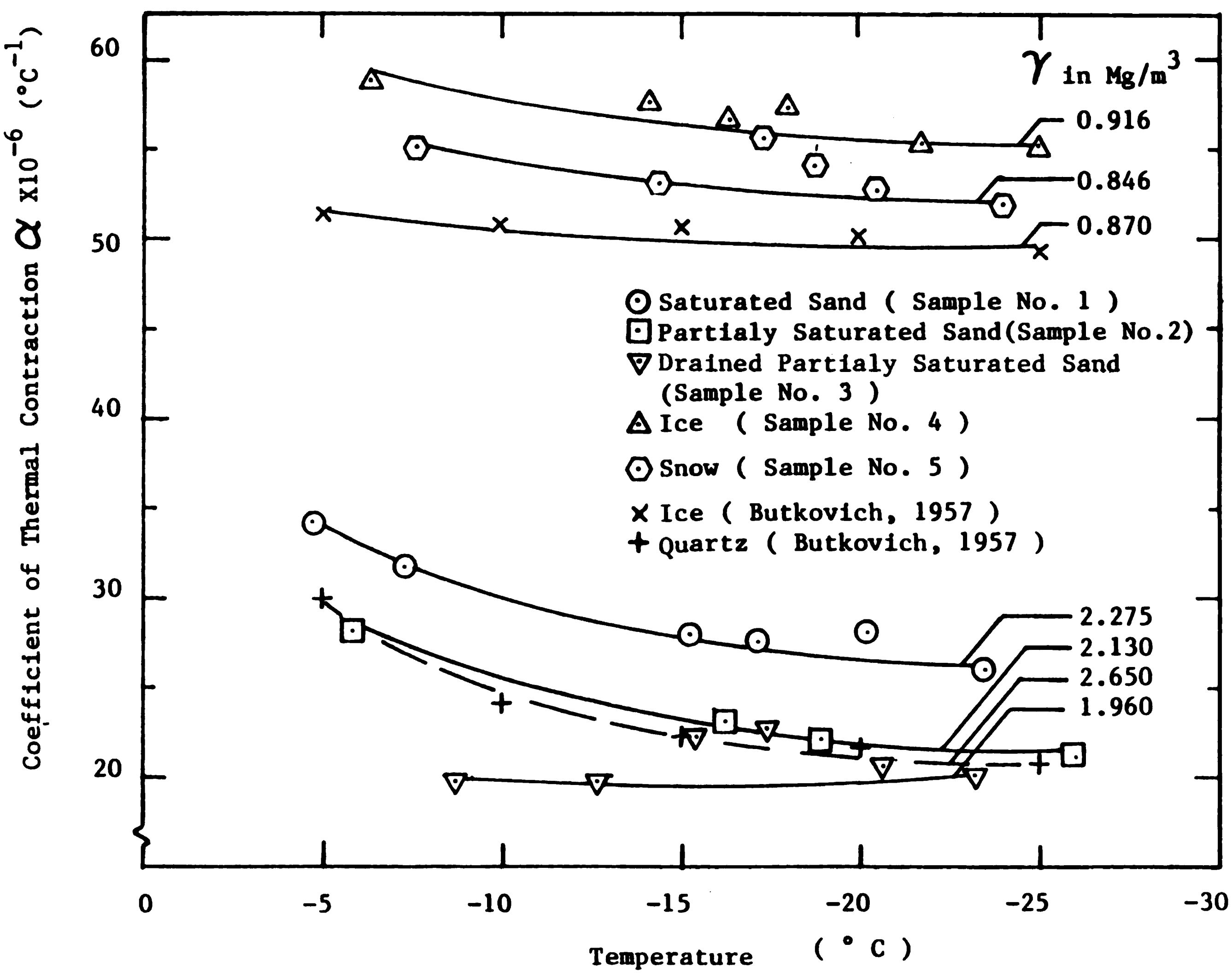

Figure 3-4: Effect of Temperature on the Coefficient of Thermal Contraction for Frozen Sand, Ice, and Quartz.

the coefficient of thermal contraction as shown in Figures (3-4) and (3-5). In all samples tested and the data reported by Butkovich (1957), the effect of changing the temperature from -5 °C (23 °F) to -25 °C (-13 °F), changed the coefficient by at most $\pm 4 \times 10^{-6}$ °C^{-1}. A comparison of these coefficients of thermal contraction for the frozen soil with the coefficient for quartz and for ice (γ = 0.97 g/cm^3), shows that α is almost constant with temperature between -5 °C (23 °F) and -25 °C (-13 °F). The presence of ice and an increase in frozen sand density serves to increase the coefficient of thermal contraction. This change is shown in Figures (3-5) and (3-6). In general, the density of the material has more effect on the coefficient of thermal contraction, than the change in temperature.

3.2 Fiber Reinforcement

3.2.1 Materials and Preparation of Compression Specimens

A commercially available silica sand (produced by UNIMIN corporation, Oregon, Illinois 61061, U.S.A.) was selected for the fiber reinforced compression samples. This sand consisted of sub-angular quartz particles with a specific gravity of 2.65. The sand gradation was uniform with all material passing the number 20 (0.840 mm) U.S. standard sieve and retained on the number 200 (0.074 mm) sieve. The coefficient of uniformity ($C_u = d_{60}/d_{10}$) was approximately 1.49.

Commercially available steel wire (gage sizes of 28, 24, and 17) was used in volume fractions of 3%, 6%, and 9%. The wire was cut to the required length of 0.50 inch or 0.25 inch as needed for samples. A sand and steel fiber volume fraction of 64 percent was selected to give a dense fiber reinforced soil mass. This volume fraction was convenient

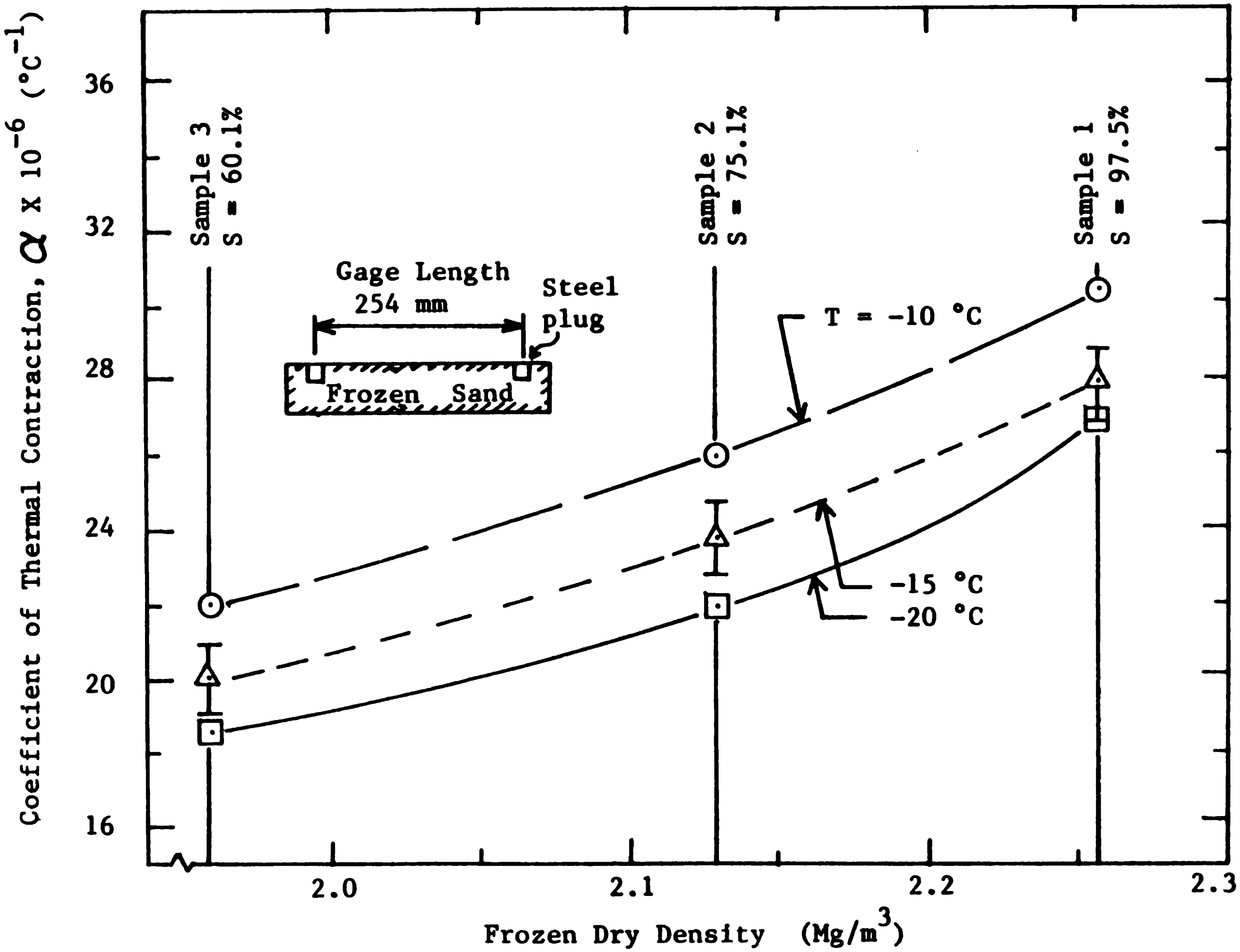

Figure 3-5: Thermal Contraction/Expansion Behavior of Frozen Quartz Sand.

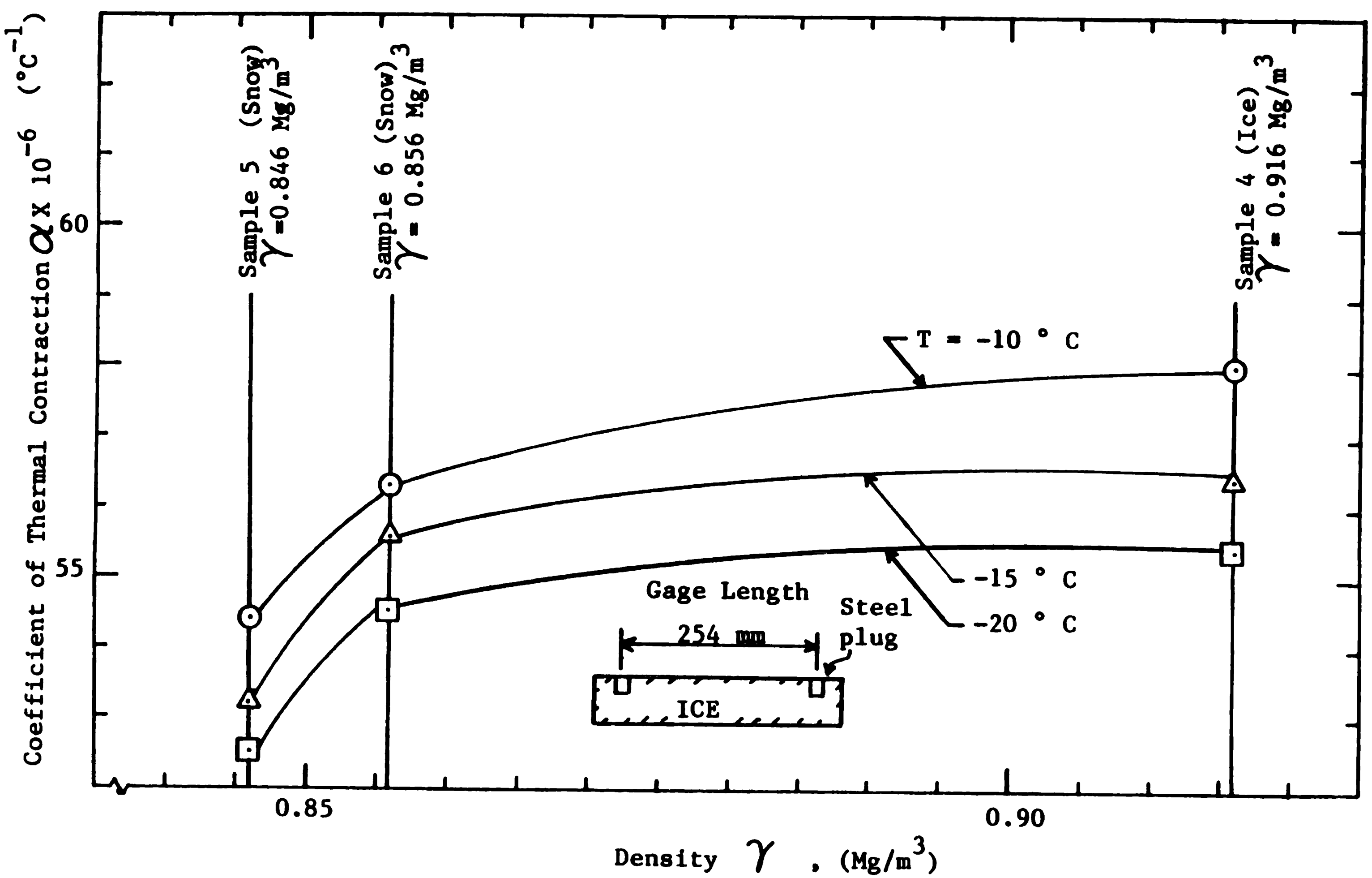

Figure 3-6: Effect of Density and Temperature on Coefficient of Thermal Contraction of Ice.

fo

fr

ex

to

pr

wa

s

g

w

s

b

a

i

g

for ease of compaction and is comparable to a compacted sand volume fraction typically encountered in the field.

All samples were prepared in split aluminum molds. A removable extension, 0.375 inches high, was attached to the open end of each mold to aid in sample preparation. The mold was disassembled and cleaned prior to each sample preparation. Next, a thin coat of silicone grease was applied to the inner mold surface to reduce ice adhesion at the sample/mold interface and to aid in sample removal after freezing.

The amount of oven dried sand, and steel fibers required for a given volume fraction, was predetermined based on the mold volume, weight of the sand, and steel fiber. To insure a high degree of saturation, molds were first partially filled with distilled water. Next, a mixture of sand and steel fibers was slowly poured into the mold allowing air bubbles to readily escape to the surface. The degree of ice saturation, for samples prepared in this manner, ranged from 96.1 to 99.9 percent based on an ice density at -14 °C of 0.9148 mg/m^3 (Pounder, 1967). Sample compaction was achieved by tapping the mold sides and bottom sufficiently to allow the fiber reinforced sand to settle within the mold. The mold and samples were then placed in a cold box at -14 °C and allowed to freeze for at least 12 hours.

Next, mold extensions were removed and the exposed sample ends were trimmed with a sharpened scraper until a uniform seating area was formed for the loading platens. Samples were then removed from the mold, weighed, and enclosed in rubber membranes to prevent sublimation during storage. Sample volume was assumed equal to the mold volume for density computations.

3.2.2 Uniaxial Compression Test

Uniaxial constant strain rate compression tests were conducted on 1.13 inch (28.70 mm) diameter cylindrical samples with a 2:1 height to diameter ratio, at a temperature of -6 °C (21.2 °F) and strain rate of approximately 1.1 x 10^{-4} sec^{-1}. Sample diameters were selected so as to stay within the capacity of the test equipment. Prior to mounting samples in the triaxial cell, a stainless steel (disk) loading platen was placed at each end of the sample.

Loading platen surfaces in contact with the sample were coated with a thin layer of Teflon to reduce end effects. Two protective membranes were placed over the samples and fastened securely to the loading platens with rubber bands. The 1.13 inch diameter samples were then mounted on the base pedestal of the triaxial cell (inside a cold box). The triaxial cell (Figure 3-7) was placed over the sample, attached to the cell base, and the loading ram was brought into contact with the top loading platen. The entire triaxial cell was then transferred to the low temperature bath and a mixture of ethylene glycol and water was allowed to fill the bath and circulate around the sample. A period of at least 6 hours was allowed for sample temperatures to adjust to the cold bath temperature prior to testing.

After completion of a test the triaxial cell was disassembled and the sample removed. The membrane and sample were inspected for leaks and the failure mode was noted and sketched. The sample was thawed and oven dried to permit determination of oven dry weights. The degree of ice saturation was then computed based on the mold volume, weight fractions of sand and fiber, and sample weight.

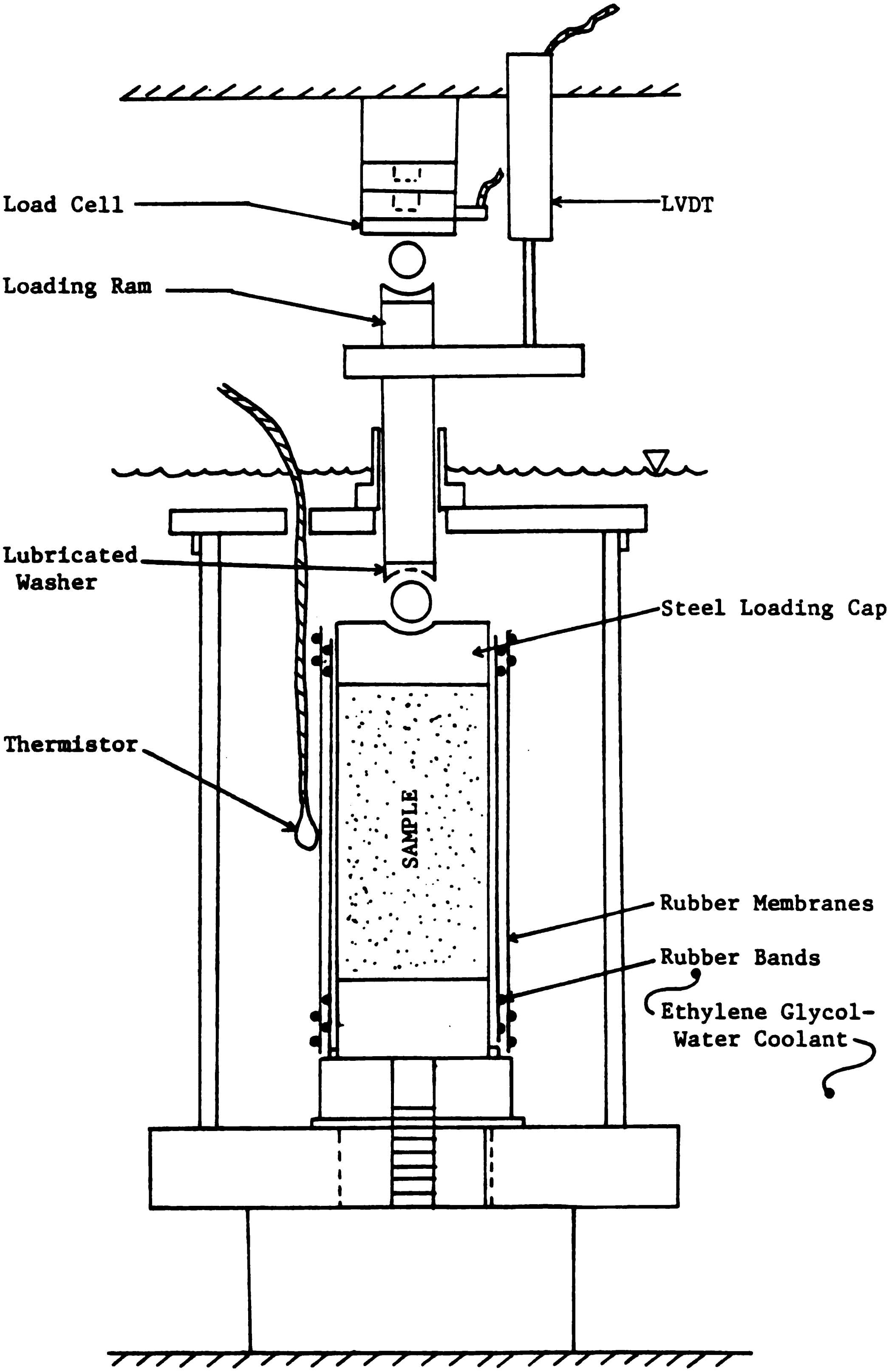

Figure 3-7: Modified Triaxial Cell.

test
diam
para
used
fro

Equ

com
sam
tri
SP
si
wa
36
sc
7)

o
b
t
r
o
t
d
.

With higher compressive strengths due to fiber reinforcement and test equipment of limited load capacity, it was necessary to use smaller diameter frozen sand specimens in the test program. The following paragraphs present a description of the equipment and test procedures used to determine the mechanical properties of the fiber reinforced frozen sand material.

Equipment:

A modified triaxial cell was used for the constant strain rate compression tests conducted on the 1.13 inch diameter samples. The samples rested on a stainless steel platen which was supported by the triaxial cell load pedestal. A flat load cell, universal, Model FLU: 5 SP2 - 0211 (rated capacity of 5,000 pounds), with SCM-700-strain gage signal conditioner was used to monitor axial loads. Axial deformation was measured using a displacement transducer (LVDT) type GCA-121-500 S/N 3665 with SCM series, S/N 987 strain gage signal conditioner. A schematic diagram of the triaxial cell assembly is shown in Figure (3-7).

A constant temperature was maintained during testing by immersion of the test apparatus (triaxial cell) in a circulating low temperature bath of ethylene glycol and water (50-50 mixture). The temperature of the coolant fluid was maintained to $\pm$ 0.1 °C using a micro-regulated refrigeration unit and circulator. A thermometer with scale divisions of 0.1 °C was used to monitor the temperature of the bath. The temperature of the coolant immediately adjacent to the sample was determined to $\pm$ 0.05 °C using a thermistor type 100 OHM platinum RTD .00385 T.C period and a Doric, Minitrend 205 data logger. A schematic di

Fi

us

a

w

0

d

s

t

s

(

I

a

I

diagram of the test equipment and coolant circulation system is shown in Figure (3-8).

The constant strain rate uniaxial compression tests were conducted using a Wykeham-Farrance (Model T57) variable speed testing machine with a 10,000 pound load capacity. This test machine had a 30 speed gear box with the capability for displacement rates ranging from 0.075 to 0.000048 inches per minute. Results indicated that the cross-head displacement rate increased slightly during testing, reaching the selected rate only after the peak load had been reached. Output from the various transducers and thermistors were recorded on a data logger strip chart, using four channels. The test set-up is shown in Figure (3-9).

Test Procedures:

After the frozen sample was mounted in the triaxial cell, the test apparatus was placed in the cold bath. When a sufficient period of time had elapsed for temperature stabilization (6-hours), the following test sequence was followed:

1. The signal conditioners were connected to the recorder, which was allowed to warm up for approximately one-half hour prior to testing. After the warm-up period, the signal conditioners were adjusted to a zero reading.
2. The loading ram of the test frame was brought into contact with the test apparatus, but with no applied load. A small seating stress, approximately 100 psi, was applied to the sample prior to testing. The manual loading feature of the Wykeham-Farrance test frame was used to apply the seating load and the magnitude was monitored with the load transducer. The specimen was not tested until the seating

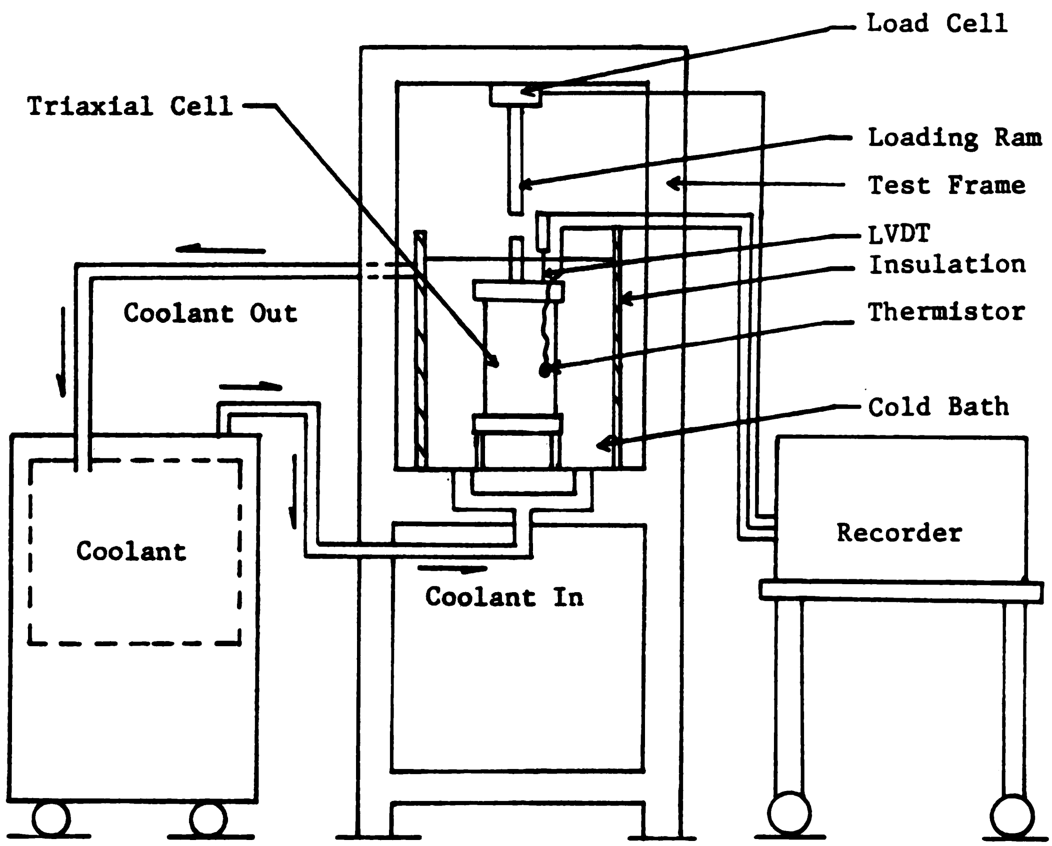

Figure 3-8: Diagram of Test System.

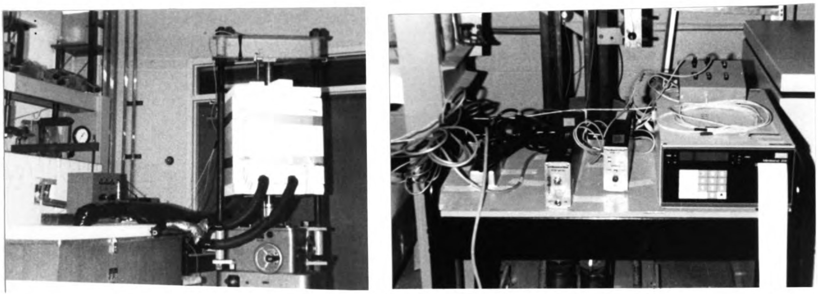

(a) (b)

Figure 3-9: Uniaxial Compression Test Set-Up. (a) Loading Unit and Constant Temperature Baths, (b) Data Collection Equipment.

stress had decreased to nearly zero by sample relaxation. This procedure gave a more uniform contact surface between the sample and loading platens and helped minimize data scatter.

3. Temperatures adjacent to the sample (inside the triaxial cell) were measured using a thermistor and monitored by the data logger.
4. The gear box controls for the loading ram were adjusted to give the desired loading rate and the loading ram was engaged.
5. Samples were deformed to at least 7 percent strain (failure or peak stresses normally occurred at greater than 5 percent axial strain). The drive mechanism for the recorder and test frame were then stopped.
6. Circuits from the transducers were disconnected from the recorder and the recorder strips were labeled and filed until the data could be transcribed to data sheets.
7. The sample was unloaded and the triaxial cell removed from the cold bath and disassembled. The failure mode was sketched and the sample was oven dried at 110 °C to determine the weight of sand.

3.2.3 Compression Test Results

Steel fibers used in reinforcing the frozen sand, provided information on the influence of gage size, volume fraction, length, and aspect ration (length to diameter ratio) on the unconfined compressive strength. A summary of these tests are given in Table (3-1). For comparison, tests were also run on specimens with no fibers.

Table 3-1: Summary of Unconfined compressive strength tests on Fiber Reinforced Frozen Sand.

Sample No	4	7	10	11	12	13	14	18	19	20	21	24	25	26	27	30	31	33	34
Steel wire (gage)	28	17	17	17	17	17		24	28	24	24	17	24	28	24	28	28	28	24
Length of wire (inches)	0.25	0.25	0.25	0.5	0.5	0.5	Frozen Sand	0.25	0.25	0.25	0.5	0.25	0.25	0.25	0.5	0.5	0.5	0.5	0.5
Diameter of wire (inches)	.016	.054	.054	.054	.054	.054		.023	.016	.023	.023	.054	.023	.016	.023	.016	.016	.016	.023
Aspect ratio (l/D)	15.6	4.6	4.6	9.2	9.2	9.2		10.8	15.6	10.8	21.6	4.6	10.7	15.6	21.6	31.2	31.2	31.2	21.6
Fiber Volume fraction V_f (%)	9	3	6	9	6	3	0	3	3	6	3	9	9	6	9	3	6	9	6
Unconfined compressive strength (lbf/in^2)	1698	1314	1431	1546	1545	1619	1464	1543	1574	1542	1366	1508	1456	1533	1901	1419	1658	2022	1861
Axial Strain (%)	7.31	5.00	5.96	6.34	6.63	5.86	5.38	5.00	5.38	6.34	5.67	5.67	6.92	6.15	9.61	5.67	8.17	7.11	4.90
Corrected Axial Strain (%)	7.12	5.66	6.25	6.75	6.18	5.76	5.18	5.25	5.50	6.67	5.67	5.75	7.00	6.00	9.62	5.87	8.25	7.11	5.18
Time to Failure (sec.)	837	350	413	444	463	450	362	368	394	475	437	431	462	450	744	519	513	881	575
Temperature (- °C)	6.1	6.0	6.1	6.0	6.1	6.1	6.1	6.0	6.05	6.05	6.0	6.1	6.0	6.0	6.0	6.1	6.0	6.1	6.1

The effect of different volume fractions for a given fiber are shown in Figures (3-10), (3-11), and (3-12). In these tests the fiber length was kept constant, either 0.25 inches (6.35 mm), or 0.50 inches (12.7 mm). As shown in these figures, increasing the fiber volume fraction increased the unconfined compressive strength and, in general, increased the modulus of elasticity for the reinforced frozen sand.

A steel fiber, gage 28, with volume fraction of 9% (sample 33), increased the compressive strength from 1464 psi (0% fiber) to 2022 psi. Note that the failure strain increased with an increase in volume fraction as shown in Figure (3-11). This behavior can be explained in that frozen soil is a brittle material while steel wire is an excellent ductile material.

Reducing the frozen soil volume fraction by adding steel fiber will also improved the energy absorption characteristics of the frozen soil. An increase from 5.3% strain for 0 % fiber up to 9.6 % (sample No. 27) with 9 % fiber was observed.

The fiber diameter, as well as the length, have an effect on the unconfined compressive strength of reinforced frozen sand. Figures (3-13) to (3-15) represent data for a constant fiber volume fraction and fiber length, but different fiber diameters. In these tests the effect of fiber surface area appears to influence the behavior. A failure mechanism for the fiber reinforced frozen sand can be explained as fiber pull out and debonding, which depends on the fiber surface area. Increasing the surface area will increase the total bond between steel fibers and ice, sand or both. This behavior will increase the resistance of the mix to compressive failure loads. The surface area for a given fiber depends on fiber diameter. As shown in Figure (3-16),

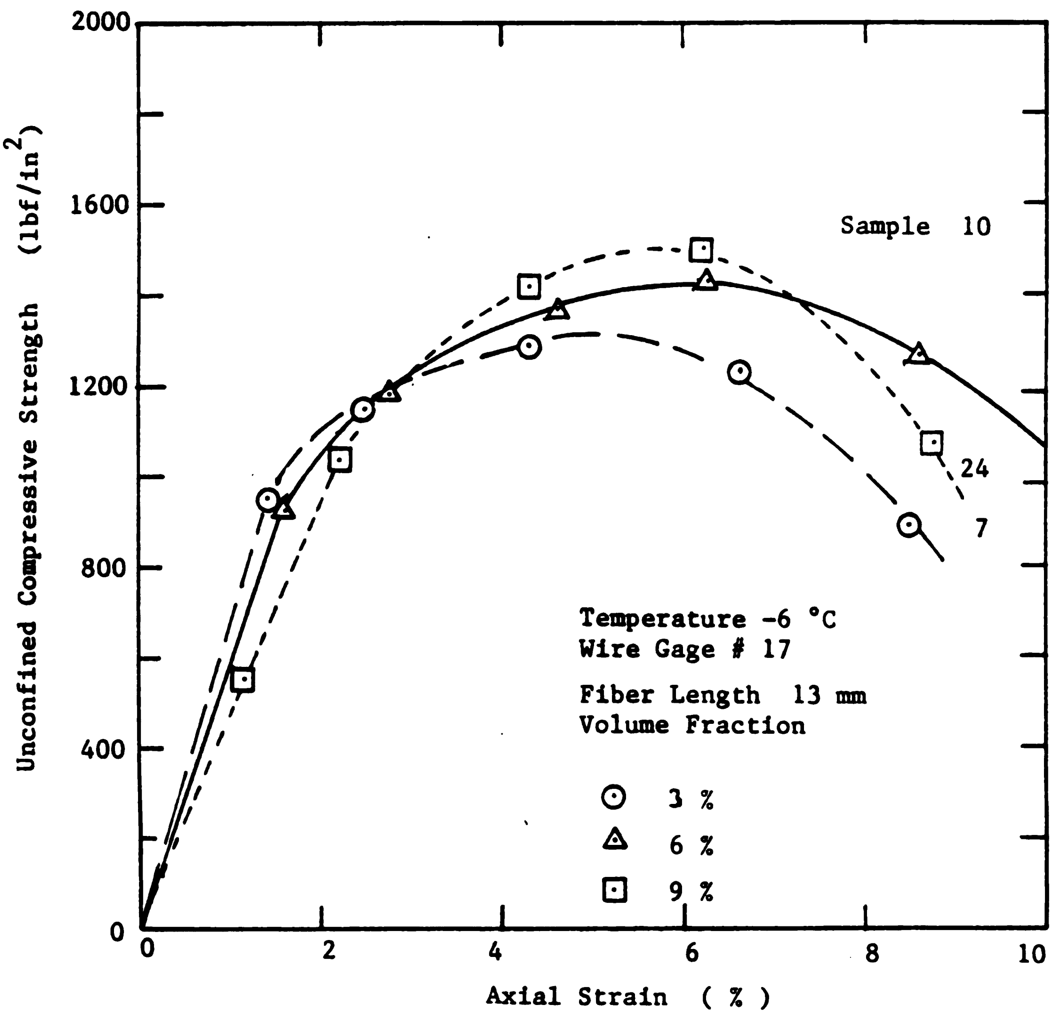

Figure 3-10: Influence of Fiber Volume Fraction on Compressive Strength of Fiber-Reinforced Frozen Sand (steel fiber gage 17).

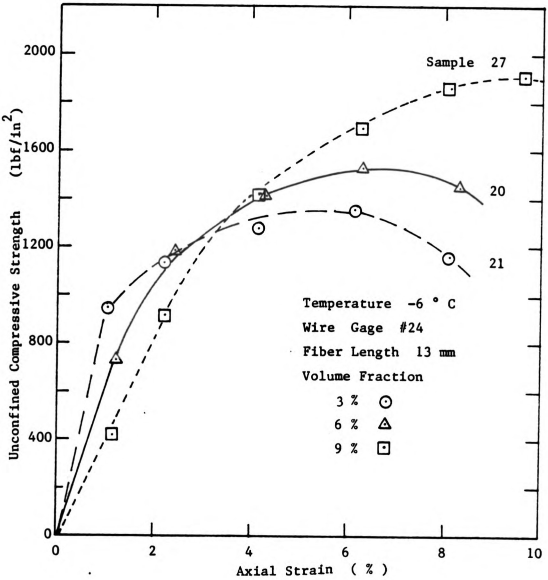

Figure 3-11: Influence of Fiber Volume Fraction on Compressive Strength of Fiber-Reinforced Frozen Sand (steel fiber gage 24).

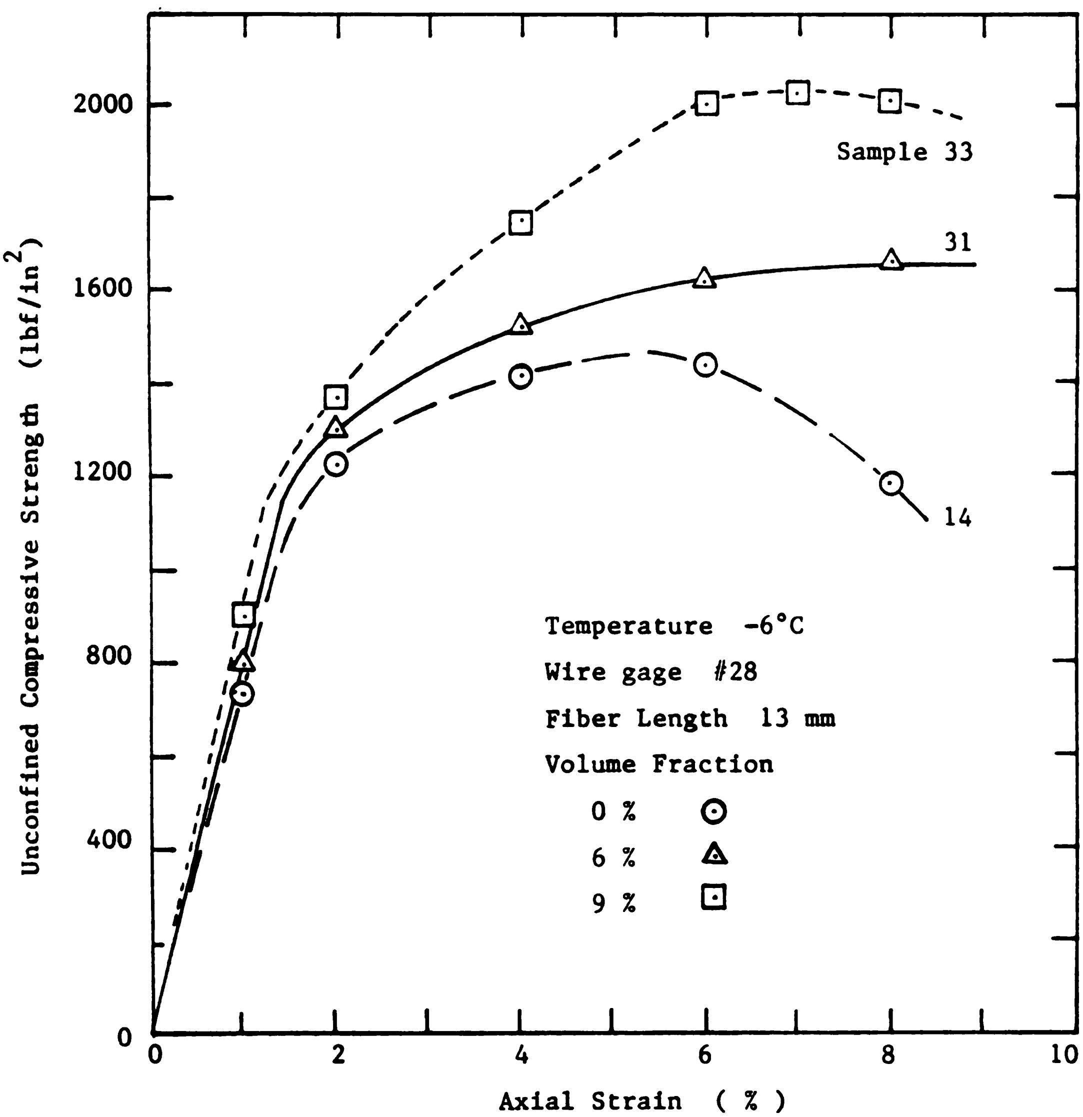

Figure 3-12: Influence of Fiber Volume Fraction on Compressive Strength of Fiber-Reinforced Frozen Sand (steel fiber gage 28).

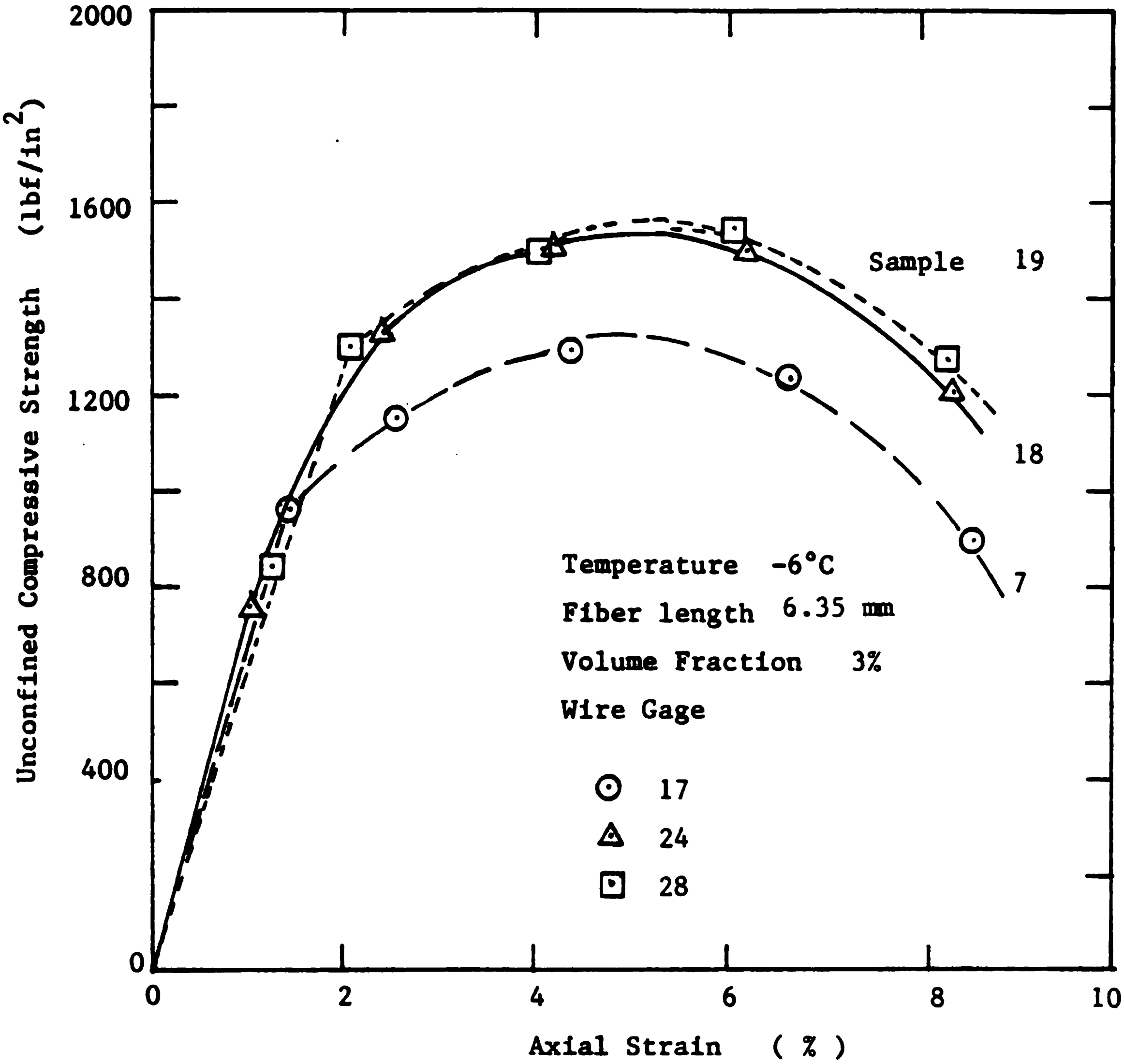

Figure 3-13: Influence of Fiber Diameter on Compressive Strength of Fiber-Reinforced Frozen Sand (fiber length = 0.25 inch).

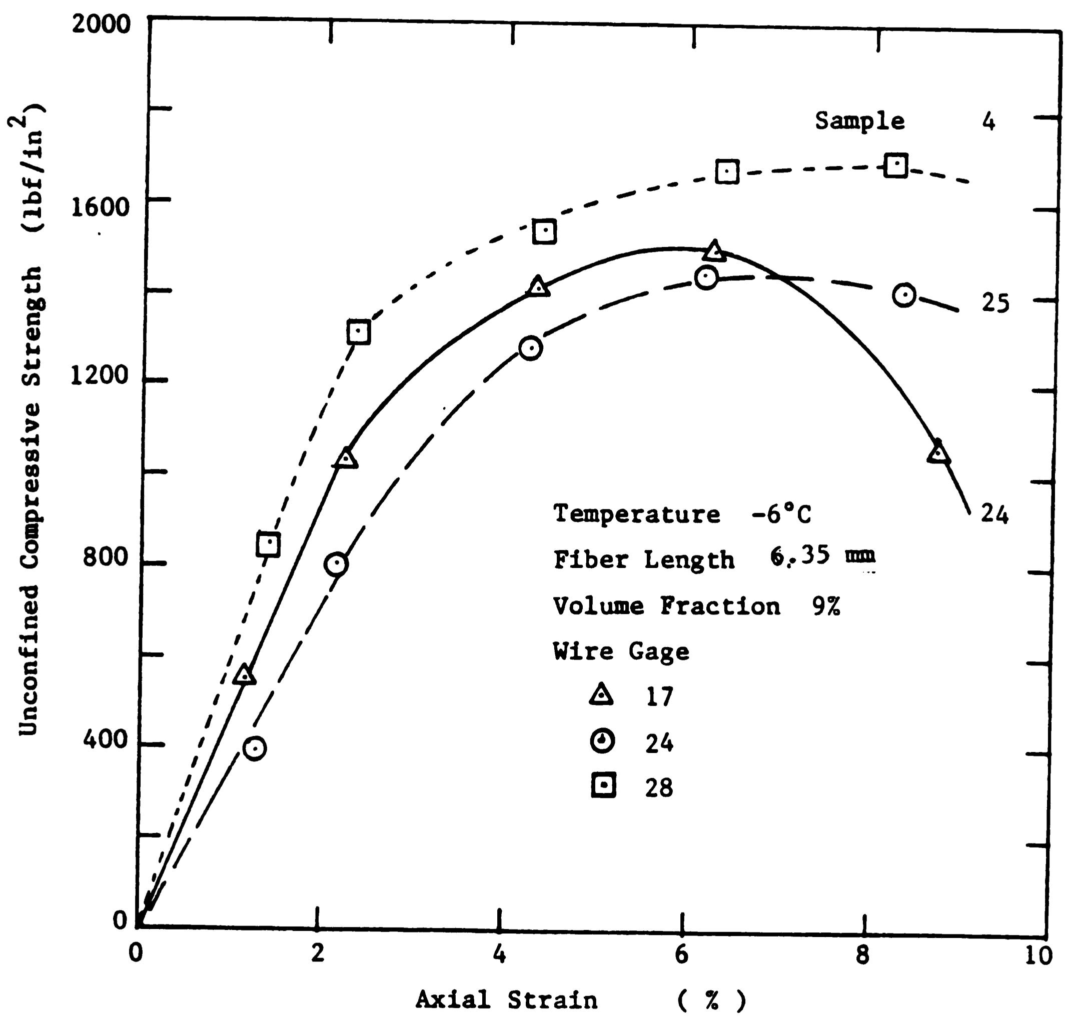

Figure 3-14: Influence of Fiber Diameter on Compressive Strength of Fiber-Reinforced Frozen Sand (fiber length = 0.25 inch).

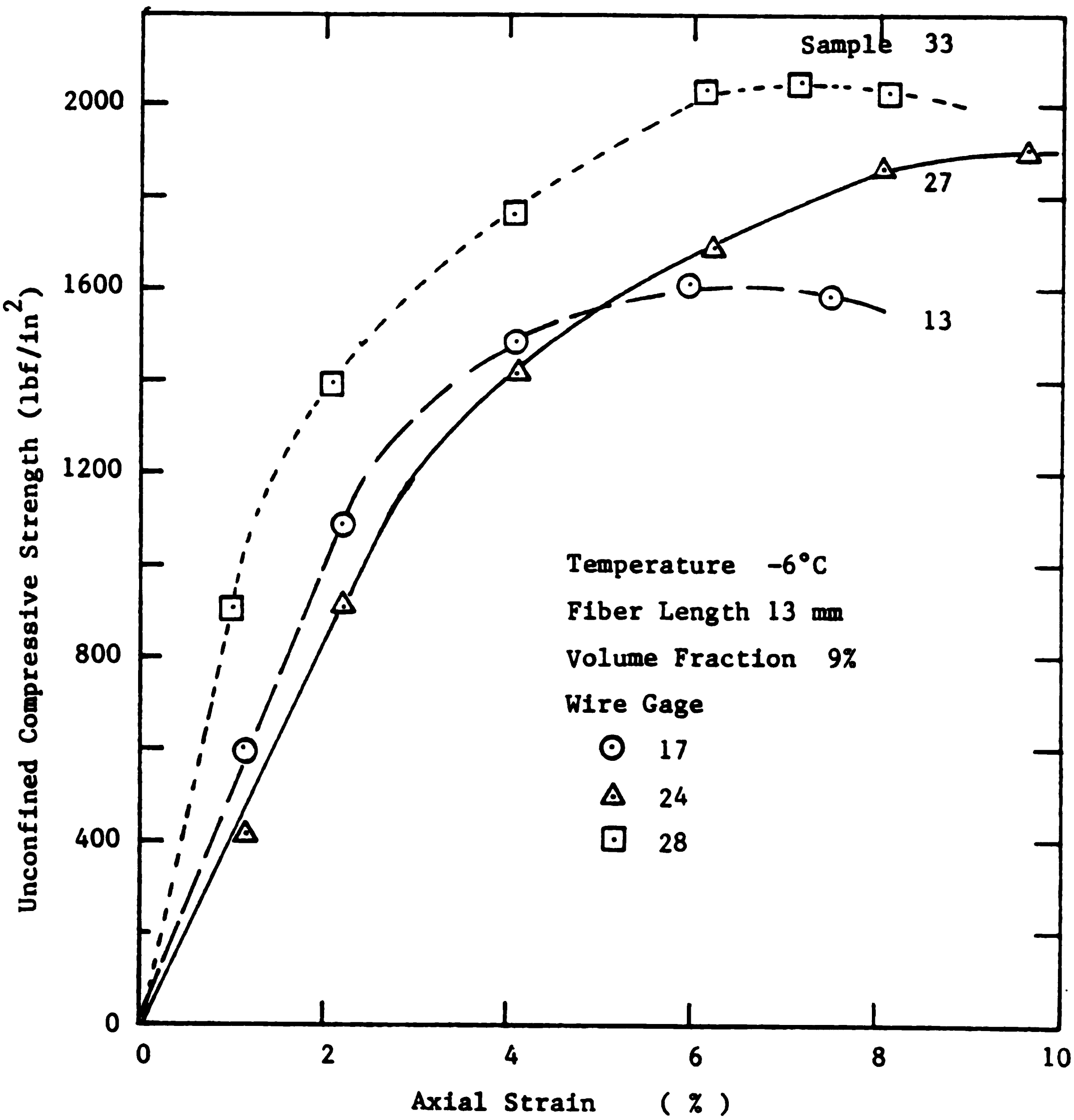

Figure 3-15: Influence of Fiber Diameter on Compressive Strength of Fiber-Reinforced Frozen Sand (fiber length = 0.50 inch).

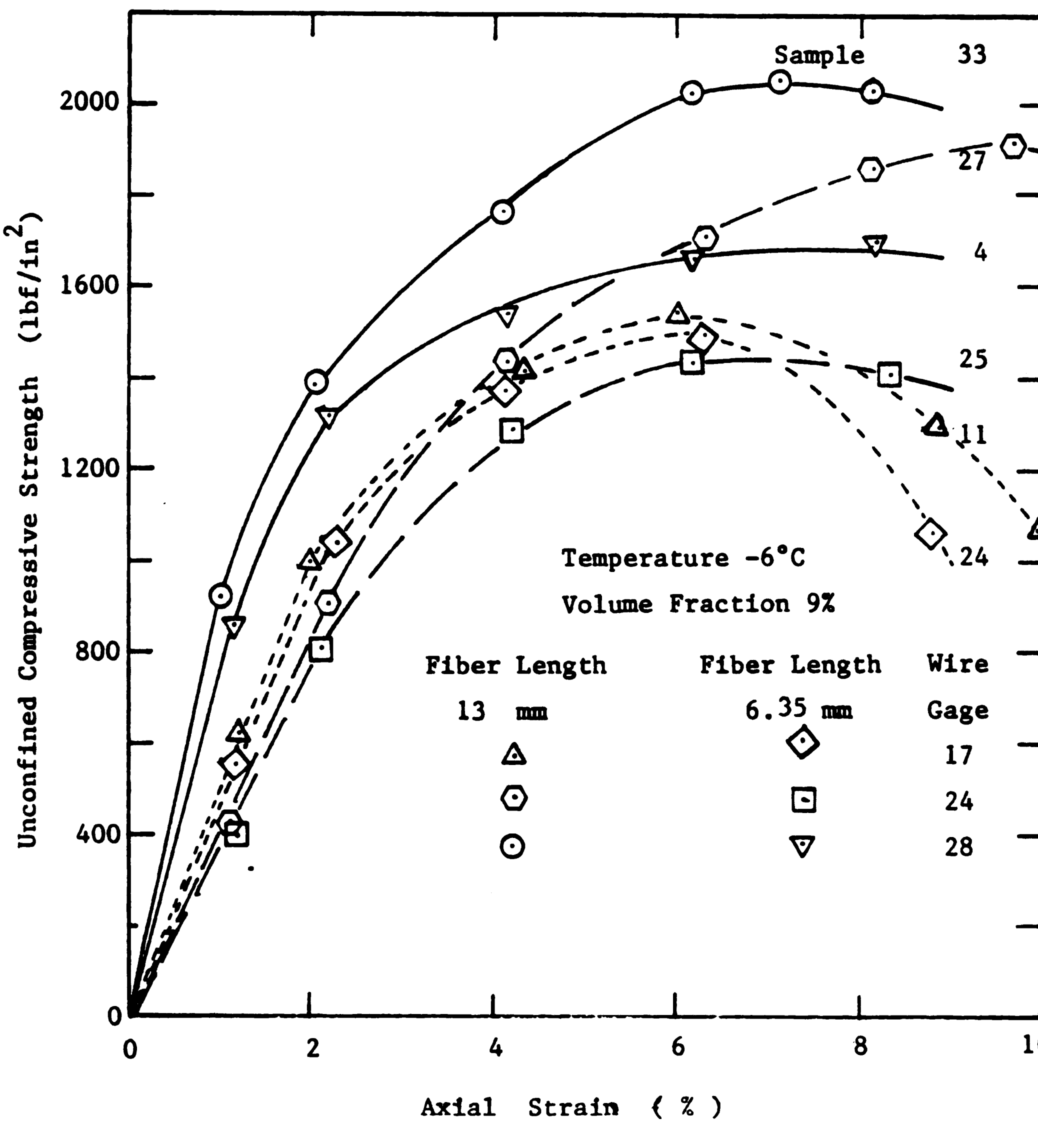

Figure 3-16: Influence of Fiber Diameter and Gage Length on the Compressive Strength of Fiber-Reinforced Frozen Sand.

for a fiber volume fraction of 3%, the steel wire (gage 28) of diameter 0.016 inches (0.4064 mm) has a higher modulus of elasticity and failed at a higher compressive strength, as compared to samples reinforced with fiber gages 24 and 17.

The effects of a combination of fiber lengths and diameters can be visualized by introducing the aspect ratio effect on the unconfined compressive strength of frozen sand. Increasing the length will increase the aspect ratio of a given fiber, with a known diameter. Influence of volume fraction and aspect ratio of different fibers on the unconfined compressive strength are shown in Figure (3-17), Al-Moussawi, and Andersland (1988). For both an increase in aspect ratio and volume fraction of steel fiber, all tests showed an increase in the unconfined compressive strength. At a given aspect ratio, the addition of fiber made it more difficult to obtain the same soil density in areas adjacent to the fibers. For this reason little or no strength increase was indicated for 3% fiber volume.

3.3 Thermal Tensile and Stress Relaxation Tests

3.3.1 Materials and preparation of Tensile Specimens

Silica sand with properties the same as that used for the thermal contraction tests was used in sample preparation. Particle size distribution for the sand is given in Table (3-2).

An aluminum mold, with dimensions shown in Figure (3-18), was used to prepare the frozen sand sample. The sample was shaped as shown in Figure (3-19) to minimize end effects. Screw rods at both ends transferred the load from the end plates (Figure 3-20), to the frozen sample. The three piece mold was first coated with vacuum grease at all

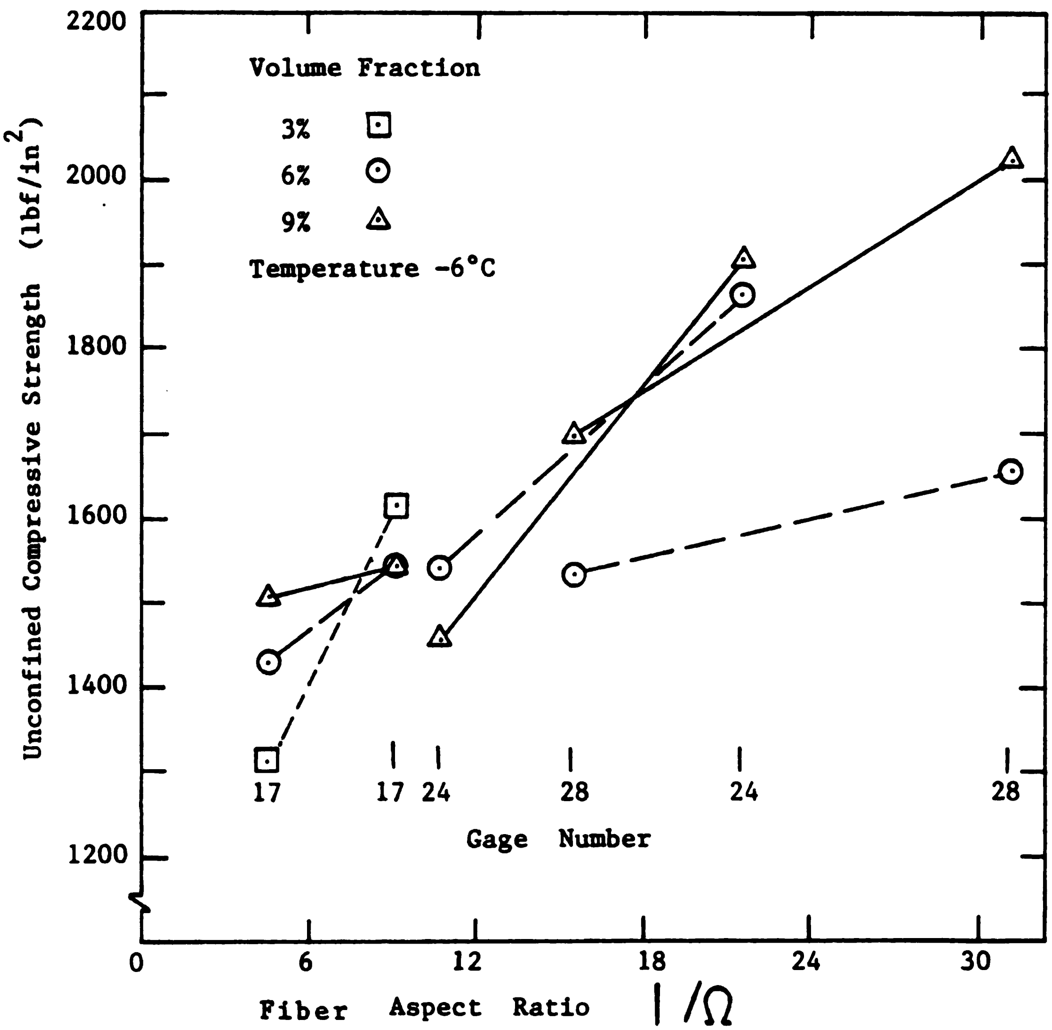

Figure 3-17: Influence of Fiber Aspect Ratio on the Unconfined Compressive Strength of Fiber Reinforced Frozen Sand.

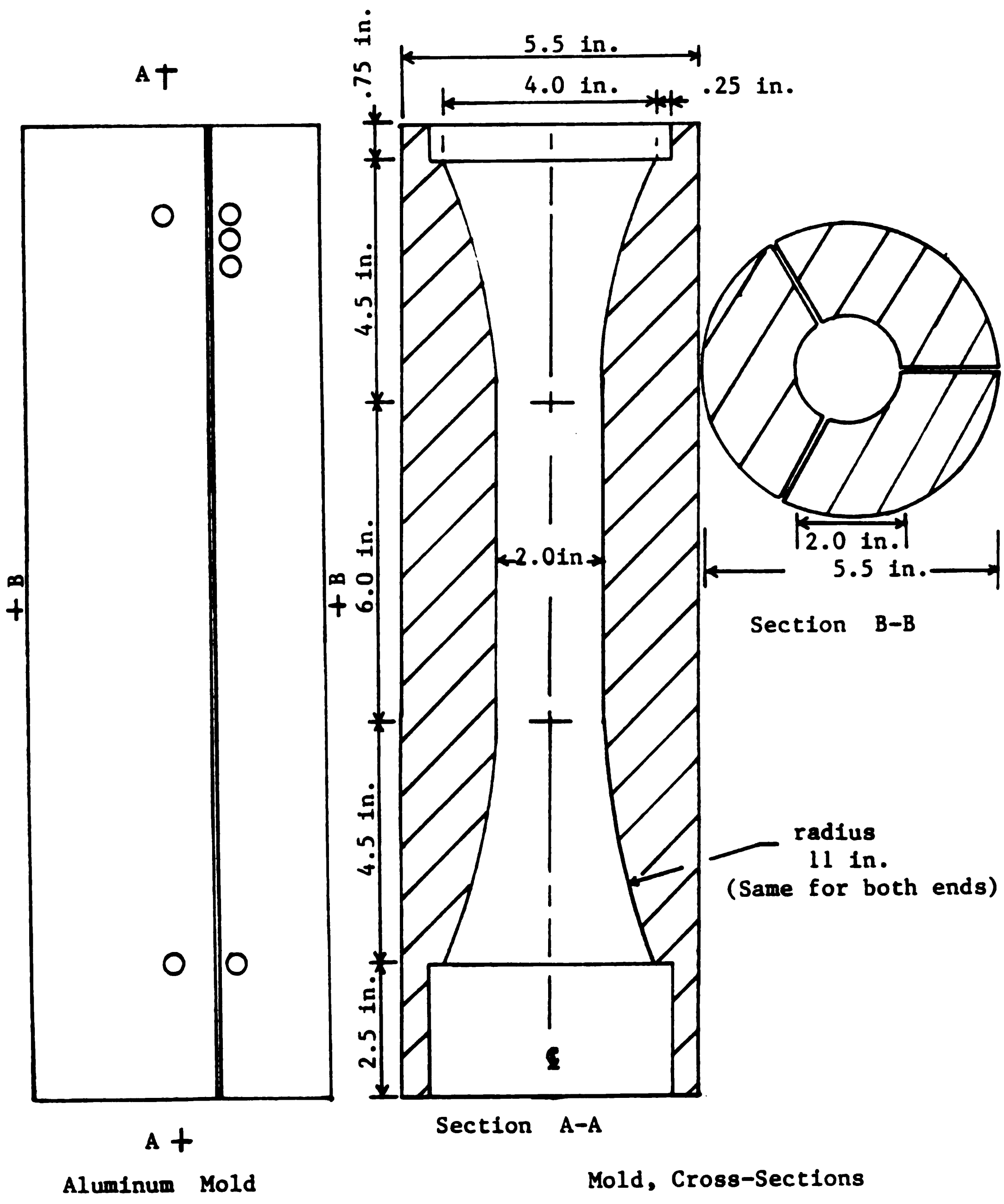

Figure 3-18: Aluminum Mold Used in Preparation of Frozen Tensile Test Samples.

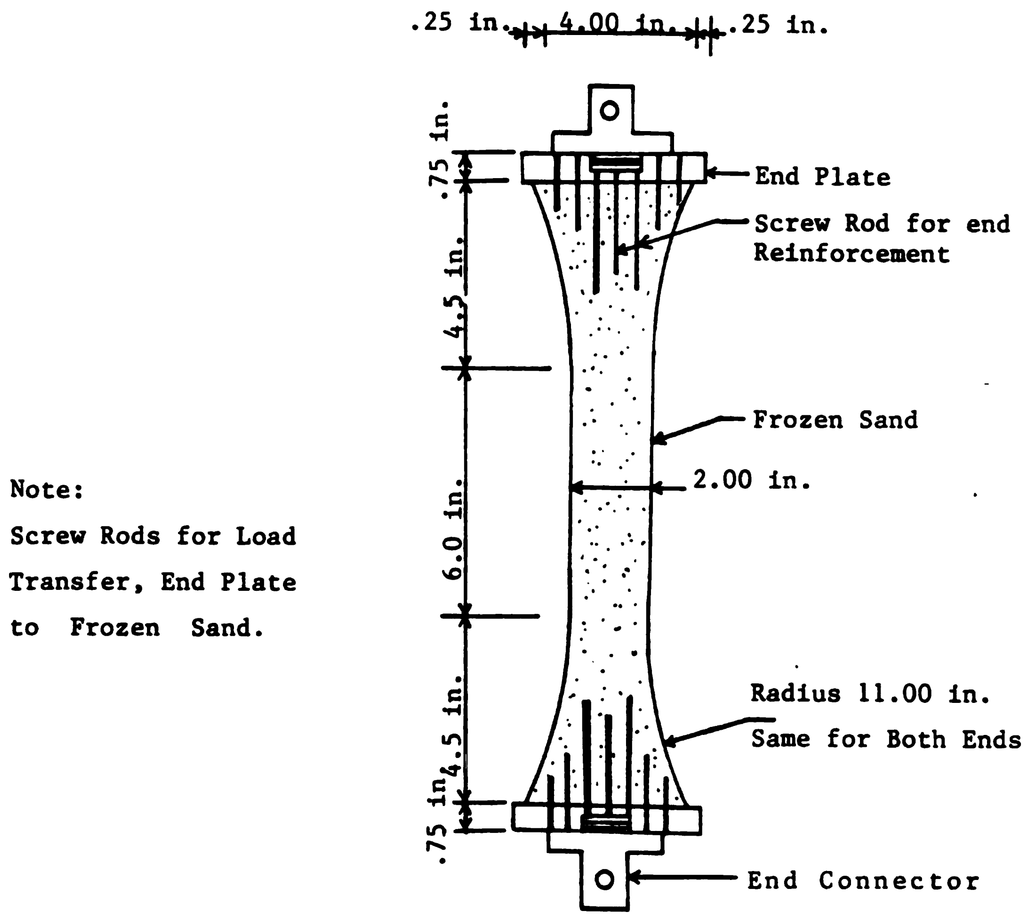

Figure 3-19: Tensile Test Sample Cross-Section With End Plates, Screw Rods, and Connectors in Position.

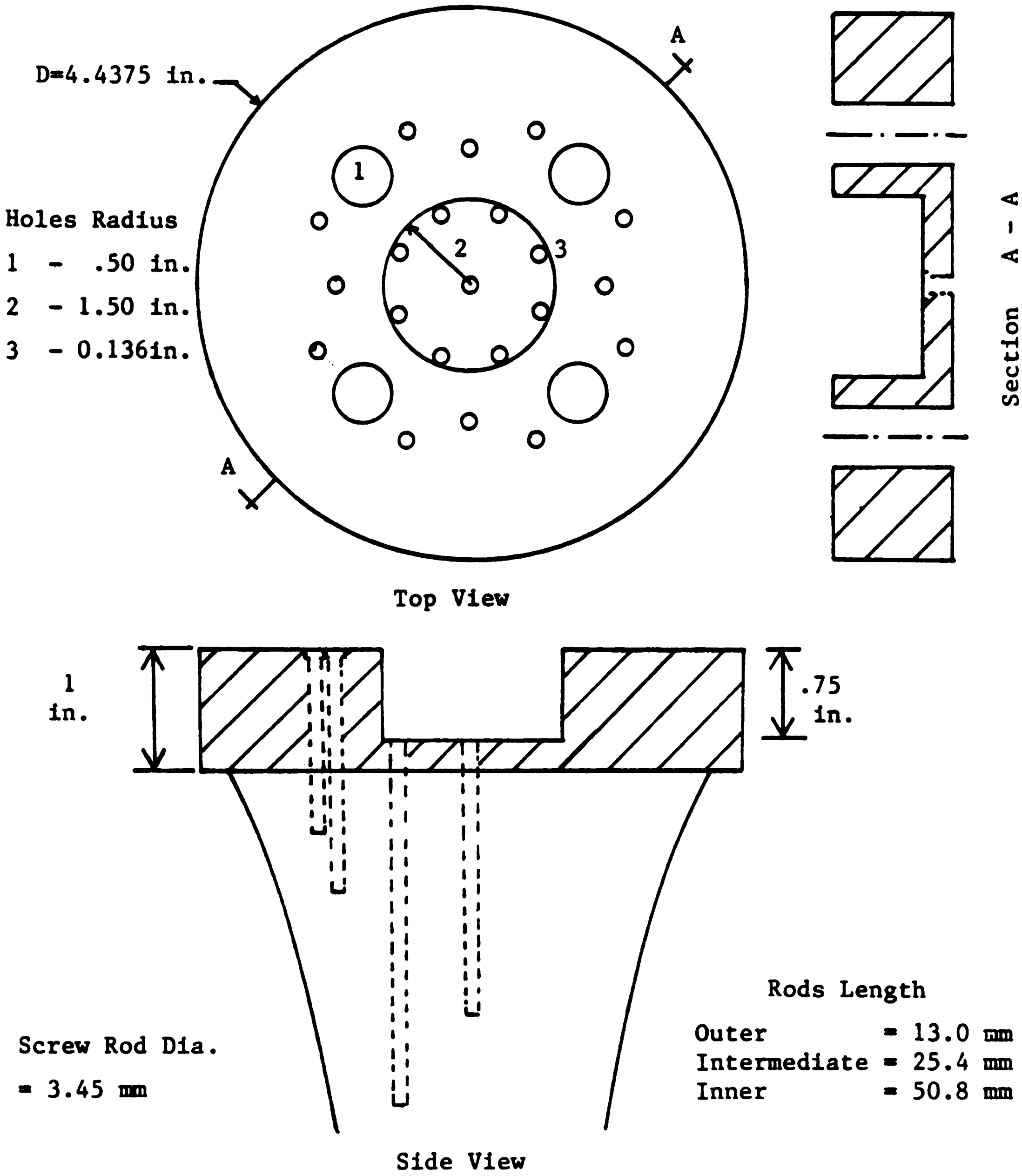

Figure 3-20: Tensile Test Specimen End Plate with Fabrication Details.

Table 3-2: Weight Size Fractions of Sand Used in Preparation of the 2100 gm Samples for Tensile Stress Relaxation Tests.

U.S. Standard Sieve Number	Weight (gm)	Percent Finer by Weight
30	4.20	96.00
40	1092.00	47.98
50	831.60	20.44
70	140.70	10.36
100	24.78	3.26
140	4.62	0.56
200	1.26	0.07
pan	0.84	0.00
Total	2100.00	

joints and assembled. Next, water was poured in the mold to help air bubbles escape during placement of the sand. Tamping the sand during placement helped achieve a relatively homogeneous and dense sample.

The mold with the sample inside, was placed in the freezer for freezing and cooling to -20 °C (-4 °F). Next, the sample was removed from the mold and supported vertically inside the freezer by connecting the end plates to the connector bars attached to the load frame. While in the freezer, the sample temperature was allowed to adjust to -5 °C (23 °F). The test was started at -5 °C. Two metal screens placed around the sample provided support for the dry ice coolant as shown in Figure (3-21). Partial control of cooling rates was handled by changing the space between the sample surface and the dry ice. The outer screen diameter was adjusted so as to provide space for a minimal amount of dry

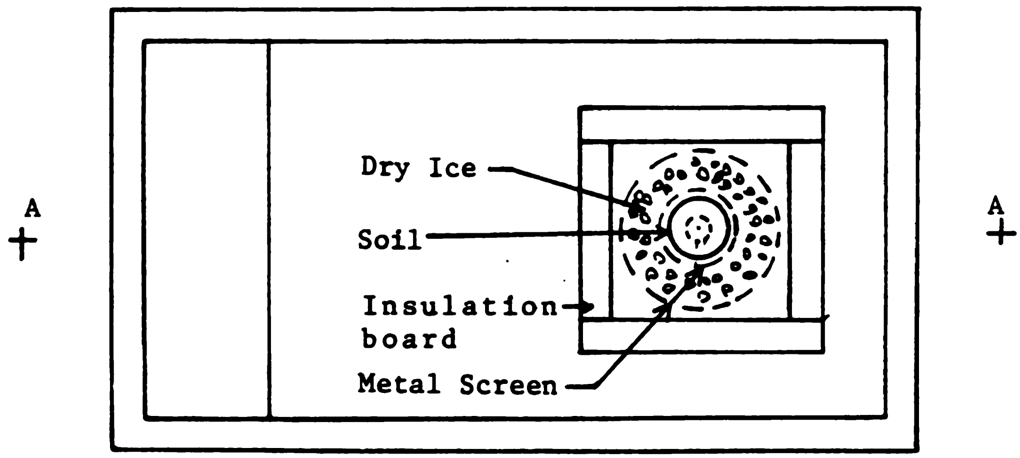

(a) Top View

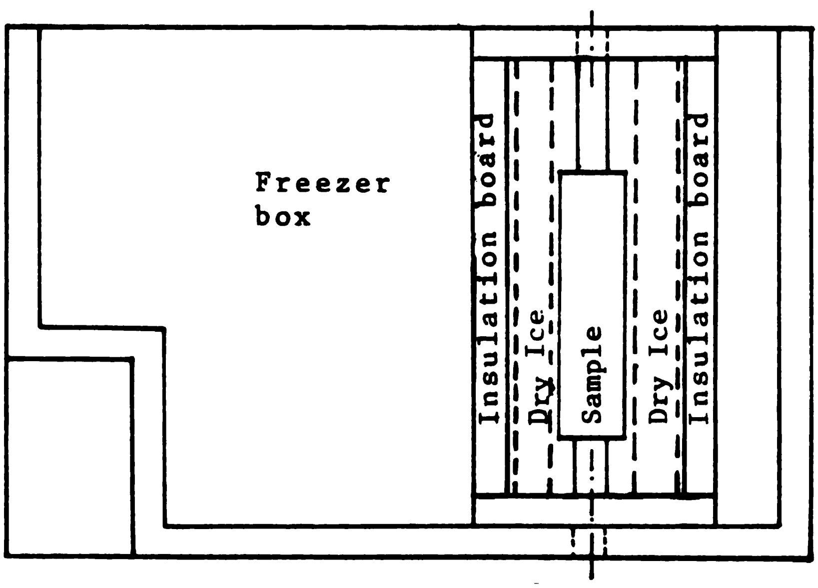

(b) Section A - A

Figure 3-21: Freezer Box Modification for the Thermal Contraction Tests Including Insulation Board Location and Metal Screen for Support of the Dry Ice.

ice. An insulation board box placed around the dry ice in the freezer helped reduce external heat effects and vaporization of the dry ice.

3.3.2 Experimental Equipment

Temperatures were measured using six thermistors (type 100 OHM Platinum RTD .00385 T.C.) attached to the sample surface, four on the ends and two at the mid cylindrical section as shown in Figure (3-22). A flat load cell (Model FL5U(C)-2SP) with rated capacity of 5000 pounds was used with a strain gage signal conditioner (Model SCM-700) to measure axial loads. Axial deformation was measured with an LVDT type (GCA-121-500 S/N 3665 with SCM series, S/N 987) strain signal conditioner as shown in Figure (3-23). Loads, axial deformation, and temperature were monitored using a Doric Minitrend 205 data logger. Data output from the various transducers and thermistors were recorded on the logger strip chart, using eight channels. Figure (3-23) shows the test set-up for both tensile and stress relaxation tests.

3.3.3 Test Procedures

After mounting the tensile sample as shown in Figure (3-24) and waiting six hours for temperature stabilization, the test sequence described below was followed for both tensile and stress relaxation tests.

1. The signal conditioner was connected to the recorder, and allowed to warm up for approximately one-half hour prior to testing. After warm-up the signal conditioners were adjusted to a zero reading.
2. A small seating stress, approximately 100 psi, was applied to the sample prior to testing by adjusting the nut on top of the load

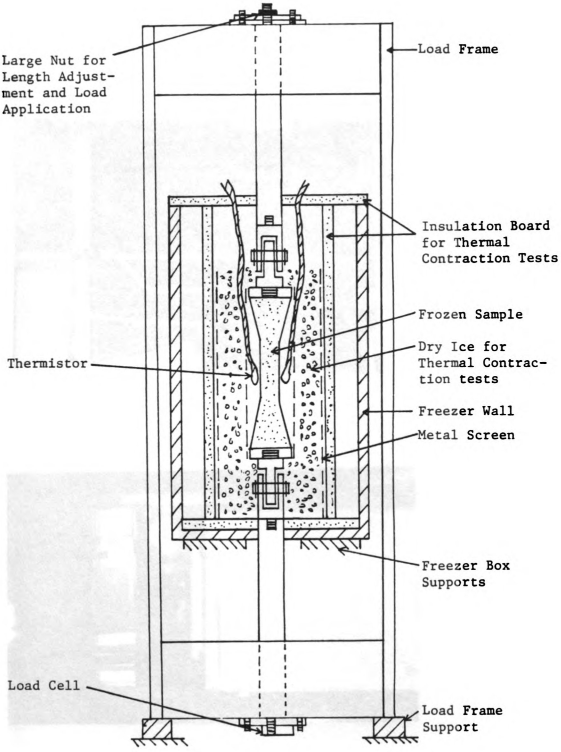

Figure 3-22: Diagram Showing Frozen Tensile Sample in Position for Stress Relaxation Tests or Loading by Thermal Contraction.

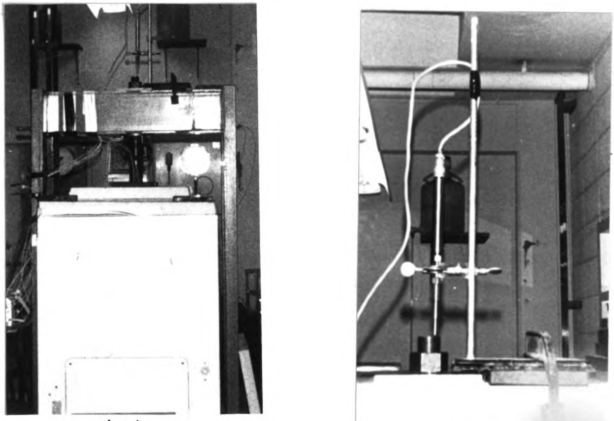

(a) (b)

Figure 3-23: Equipment for Tensile and Stress Relaxation Tests. (a) Freezer Box and Load Frame, (b) Measurement of Axial Deformation.

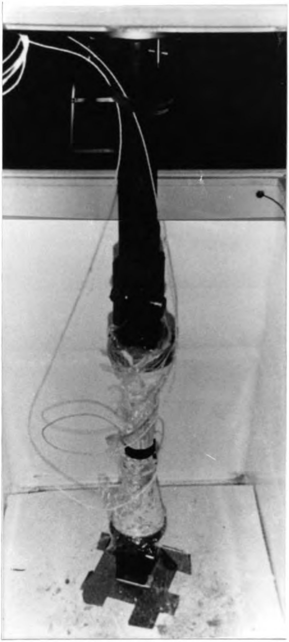

Figure 3-24: Frozen Sample with Thermistors in Freezer Box After Mounting on Load Frame.

frame. Next the seating stress was allowed to decrease by relaxation to nearly zero. This procedure provided a more consistent load transfer between the end plates and the sample through the connectors, and helped to minimize data scatter.

3. With the sample in tension, dry ice was placed around the sample. This caused thermal contraction in the sample and an increase in tensile stress. With time and sufficient cooling, peak stresses or tensile failure occurred in the samples.

4. In the stress relaxation test all samples were tested at -15 °C (5 °F) with no dry ice. Temperatures were controlled by the freezer with a small fan providing circulation and a more uniform temperature within the freezer. Initial stresses were introduced to the sample manually by adjusting the load on the top sample end plate. Tests were strain controlled, i.e., stress relaxation occurred only as a result of creep in tension. This creep was allowed to continue to a level where very little change in the stress occurred with time. After the desired number of strain cycles, the sample was manually loaded in tension to failure.

5. After completion of each test, all transducer circuits were disconnected from the recorder, and data strips were labelled and filed until they could be transcribed to data sheets.

6. The sample with end plates was removed from the freezer. The failure mode was sketched or photographed, as shown in Figure (3-25), and the sample was oven dried at 110 °C (230 °F) to determine the weight of sand, and degree of ice saturation.

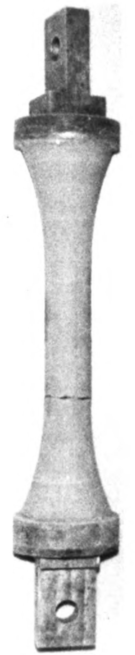

Figure 3-25: Frozen Sand Sample (No. 4) after Tensile Failure.

3.3.4 Thermal Tensile Test Results

To evaluate the effect of temperature and cooling rate on thermal contraction and cracking in frozen sand, tensile specimens (Figure 3-26), were initially loaded with a seating stress (close to 100 psi) after which the specimen ends were fixed. Some stress relaxation occurred before placement of dry ice around the sample area. Sample temperatures were close to -5 °C during mounting and placement of the seating load. Stress and temperatures were then monitored as a function of time as the specimens were cooled to temperatures as low as -78 °C (-108.4 °F). The sublimation temperature for dry ice provided a reasonable lower temperature for these tests and helped provide a larger range of cooling rates. The rate of cooling was partially controlled by the spacing between the dry ice and the specimen. For the most rapid cooling rate (-4.31 °C/min) the specimen diameter was reduced to 1 inch at its mid-section allowing temperature change to occur more quickly.

The change in temperature and tensile stress with time for sample 4 is presented in Figures (3-26) and (3-27). Reasonably constant rates of temperature decrease were achieved over portions of the curve. Sample temperatures are average values for the smaller middle portion of the test specimens (Figure 3-26). With thermistors placed on the specimen sides, cooling tests on duplicate samples showed that measured temperatures were close to average values when a small adjustment was made in the time scale. For the tensile test results, it appeared that this correction was very minor, and therefore has been omitted for the data presentation. Towards the end of a test at higher stresses, failure in tension was very sensitive to any vibrations in the load frame caused by adding dry ice or other adjustments in the equipment.

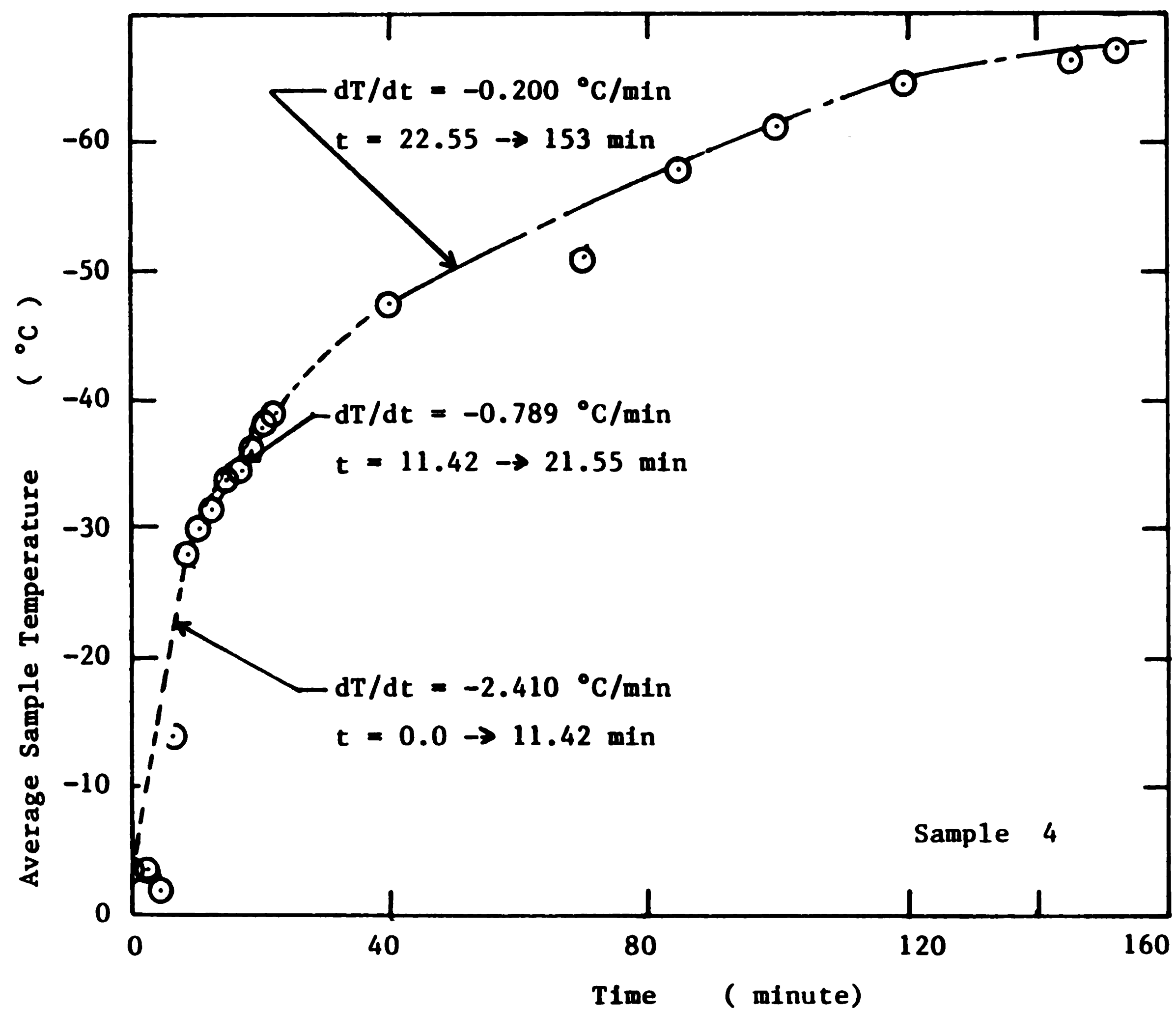

Figure 3-26: Temperature versus Time for Sample 4, Showing Change in dT/dt.

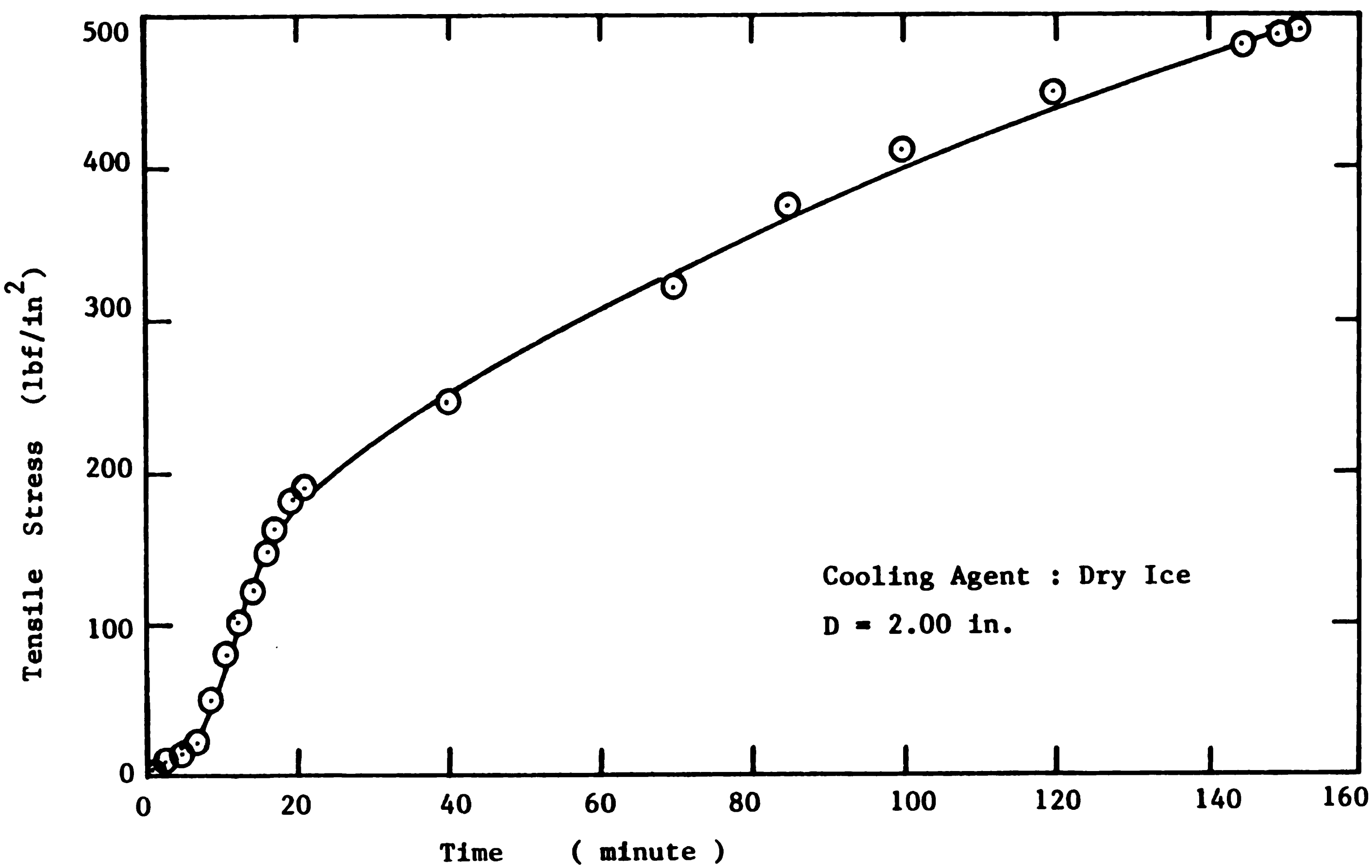

Figure 3-27: Development of Tensile Stress with Time for Sample 4.

Data for samples 1, 2, and 3 are summarized in Figures (3-28), (3-29), and (3-30). As expected, the more rapid cooling rates gave higher rates of stress increase since creep and stress relaxation are time dependent. The tensile stress-time curves in Figure (3-28) show an upward curvature as lower temperatures are achieved. The temperature-time curves in Figure (3-29) appear to be more linear. A cross-plot of tensile stress versus temperature in Figure (3-30) for samples 1, 2, and 3, all show an increase in slope with colder temperatures. The greater stiffness of frozen sand at colder temperatures would explain this increase in slope. A decrease in the coefficient of thermal contraction with colder temperatures (Figure 3-5) would lead to a decrease in slope and partially cancel the effect of greater stiffness. This thermal contraction behavior implies that a colder soil sample will experience a larger stress increase per degree drop in temperature when compared to a warmer frozen soil. Field observations reported by Lachenbruch (1961) are in agreement with this observation, in that cracks more readily occur later in the winter season when the ground is colder.

A modified cold storage freezer was used to achieve a cooling rate close to -0.021 °C/min for sample 5. This tensile stress versus time data (Figure 3-31) also shows an upward curvature in agreement with data summarized in Figure (3-28). A stress of 77 psi was reached after 7.75 hr. of slow cooling. A summary of the stress/temperature cooling curves for saturated frozen sand is given in Figure (3-32). Data for sample 5 was limited to temperatures above -15 °C by the freezer box capacity. Data for sample 4 (Figure 3-32) is shown by three groups of data representing different average cooling rates.

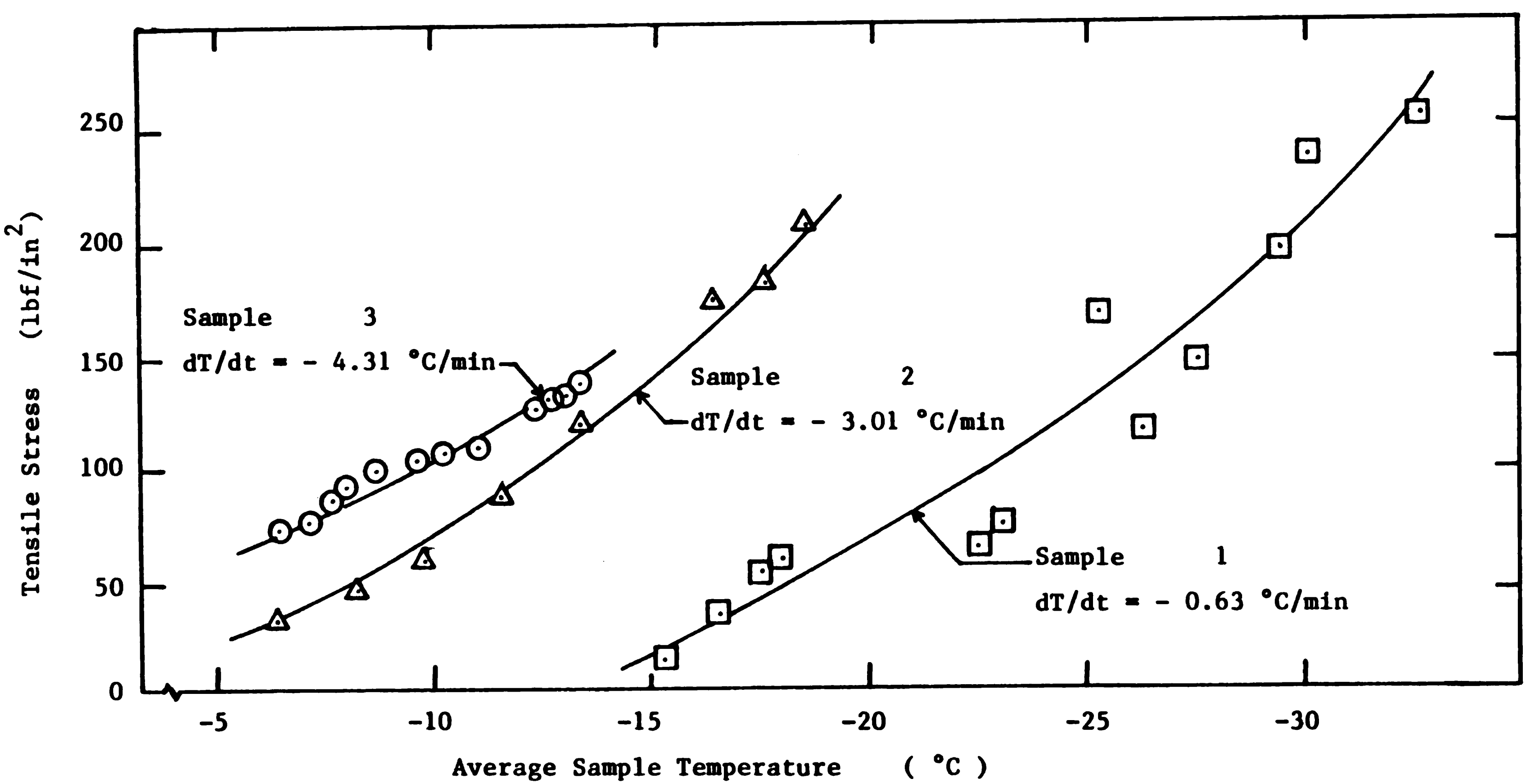

Figure 3-28: Development of Tensile Stress in Saturated Frozen Sand over a Period of Time for Three Cooling Rates.

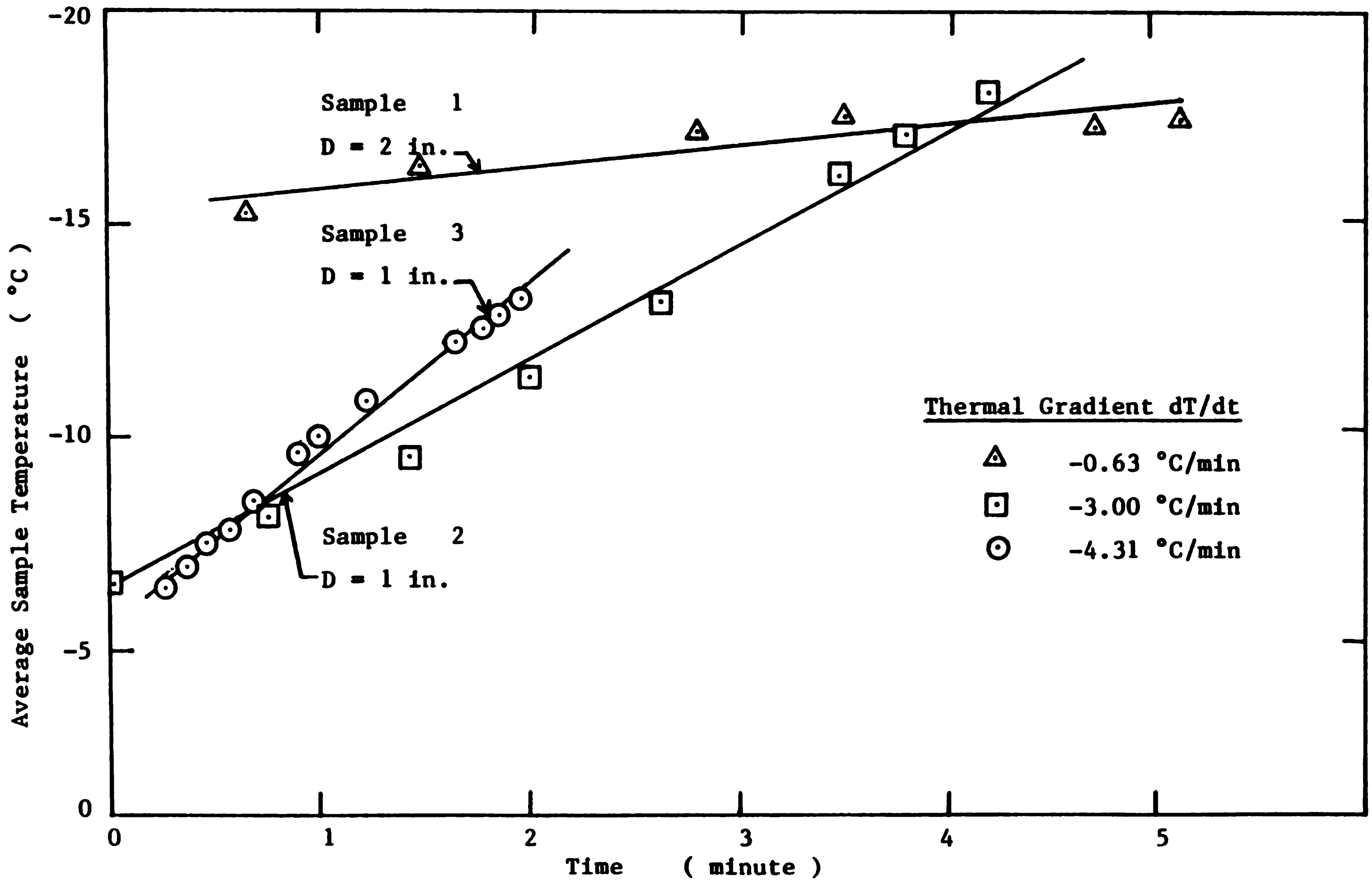

Figure 3-29: Cooling Curves for Three Saturated Frozen Sand Samples. Partial Control of dT/dt Achieved by Change in Sample Diameter and Spacing Between Dry Ice and Sample.

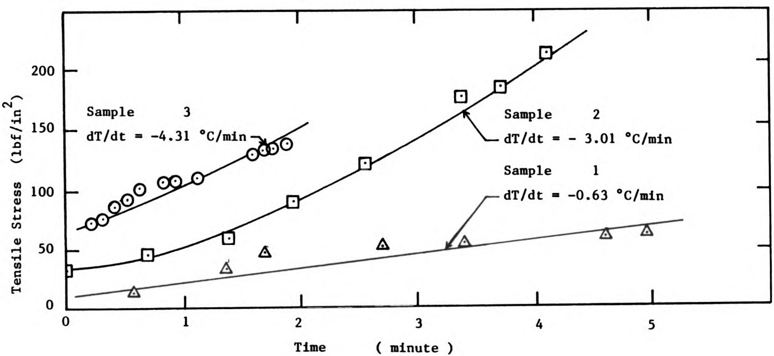

Figure 3-30: Tensile Stress Increase in Saturated Frozen Sand with Decrease in Temperature for Three Cooling rates -- -4.3 °C/min, -3.0 °C/min, -0.63 °C/min.

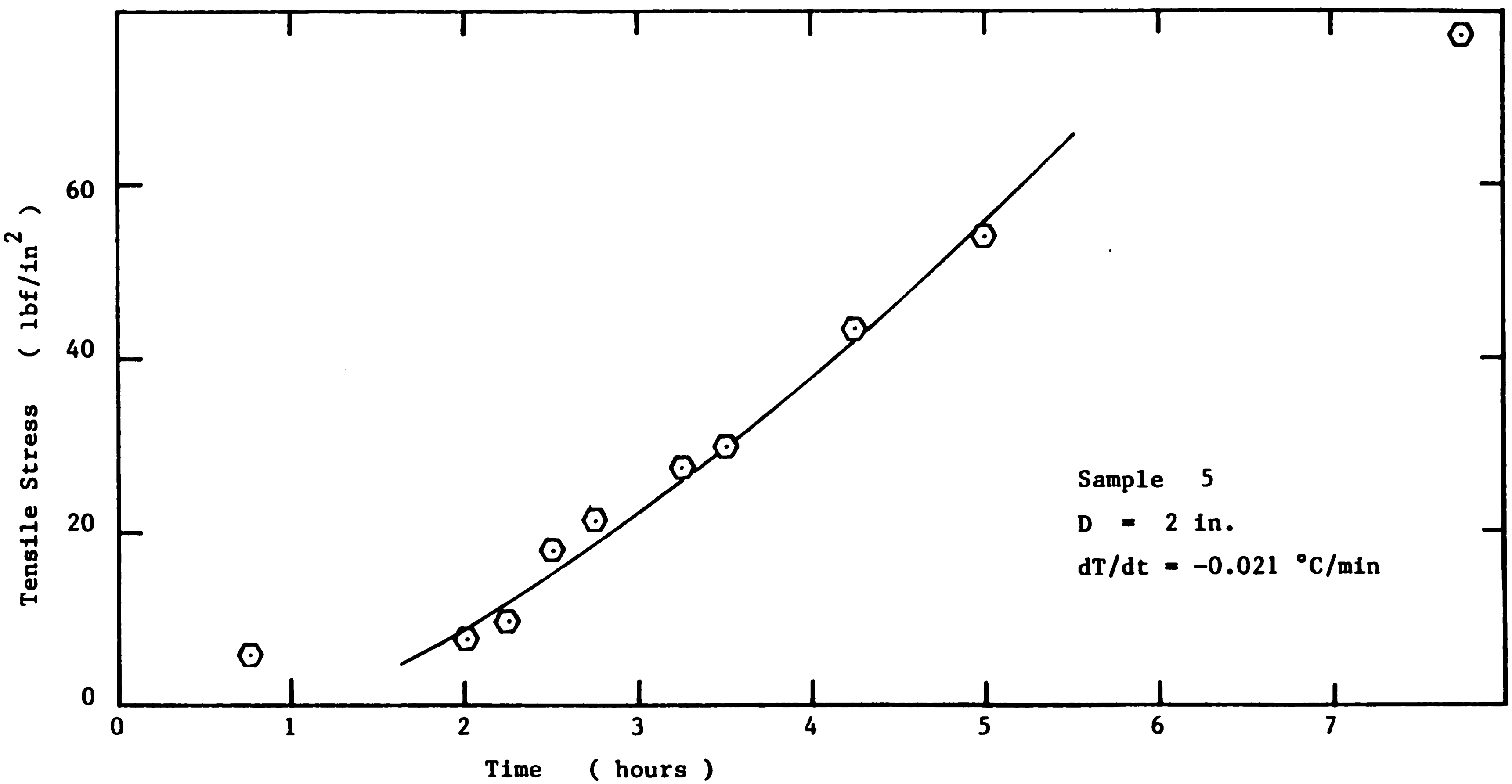

Figure 3-31: Development of Tensile Stress in a Saturated Frozen Sand with Time for a Cooling Rate of -0.021 °C/min.

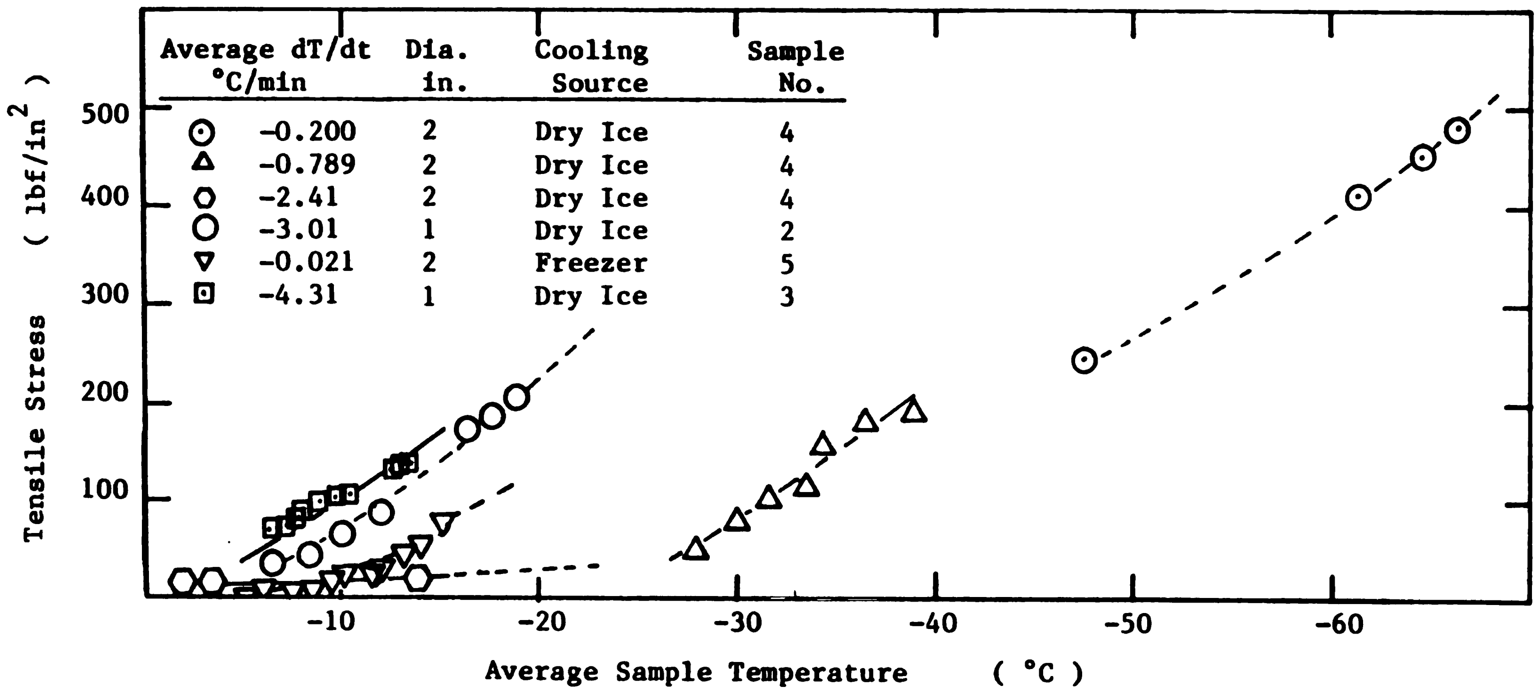

Figure 3-32: Summary of Stress/Temperature Cooling Curves for Saturated Frozen Sand.

Table 3-3: Summary of Tensile Strength Tests on Frozen Saturated Sand.

Sample No.	+ dT/dt (°C/min)	Maximum Stress (psi)	Time to Max. Stress or Failure (min.)	Sample Dia. (inch)	Cooling Source
1	-.63	258.3	-	2	Dry Ice
2	-3.01	211.0	3.98	1	Dry Ice
3	-4.31	138.5	1.876	1	Dry Ice
4	-2.41	51.83	8.21	2	Dry Ice
4	-.789	247.5	39.78	2	Dry Ice
4	-.200	490.8	152.19	2	Dry Ice
5	-.021	77.05	-	2	Freezer

+ Average values. A uniform cooling rate was achieved only over limited temperature ranges due to equipment limitations.

3.3.5 Stress Relaxation Behavior

Soil creep involves slow and progressive deformation of the material with time under a constant tensile stress. When deformation (or strain) is held constant, the tensile stress will gradually decrease or relax with time. A combination of these processes occurs during and after thermal contraction in frozen soil. Thermal contraction test results (section 3.3.4) showed that increase in tensile stress was reduced for lower cooling rates due to creep and stress relaxation.

To provide more information on the effect of cumulative strain (damage) resulting from cyclic thermal contraction on frozen soil tensile strength, a series of cyclic constant strain tests were run on duplicate samples of the type described in section 3.3.1. After mounting the specimen and allowing the temperature to come to equilibrium at -15 °C, an axial strain was applied to the specimen after which the strain was fixed. These strains, including 6.6×10^{-4} in/in for the fourth cycle, 12.0×10^{-4} in/in for the second cycle, and 10×10^{-4} in/in for the forth cycle, were applied prior to each cycle so as to simulate a permanent known deformation (plastic strain) representing past sample strain history. Selection of these strains was arbitrary, but did recognize that a total tensile strain of about 100×10^{-4} in/in would likely lead to failure (Eckardt, 1982). The sequence of load applications with the above strains is illustrated in Figures (3-33), (3-35), (3-37), and (3-38).

Figure (3-33) illustrates a reference value for stress and strain for a one load cycle. This strain value was used to estimate the permanent cyclic deformation used for the stress relaxation tests. With strains fixed for a 24-hour period, stresses decreased to the point where only very slow changes were observed. At this point the next cycle was initiated.

Fatiguing the sample to a fixed total strain and then breaking it showed effects of stress and strain at failure. This simulated what really happens in the field. In these tests, holding the temperature constant while cyclic strains where imposed in the laboratory simulated the cyclic cooling in the field.

The cyclic strain showed the following phenomenon: The series of limited cyclic tensile strains imposed on the frozen sand samples showed that strain controlled fatigue will induce strain hardening and reduce

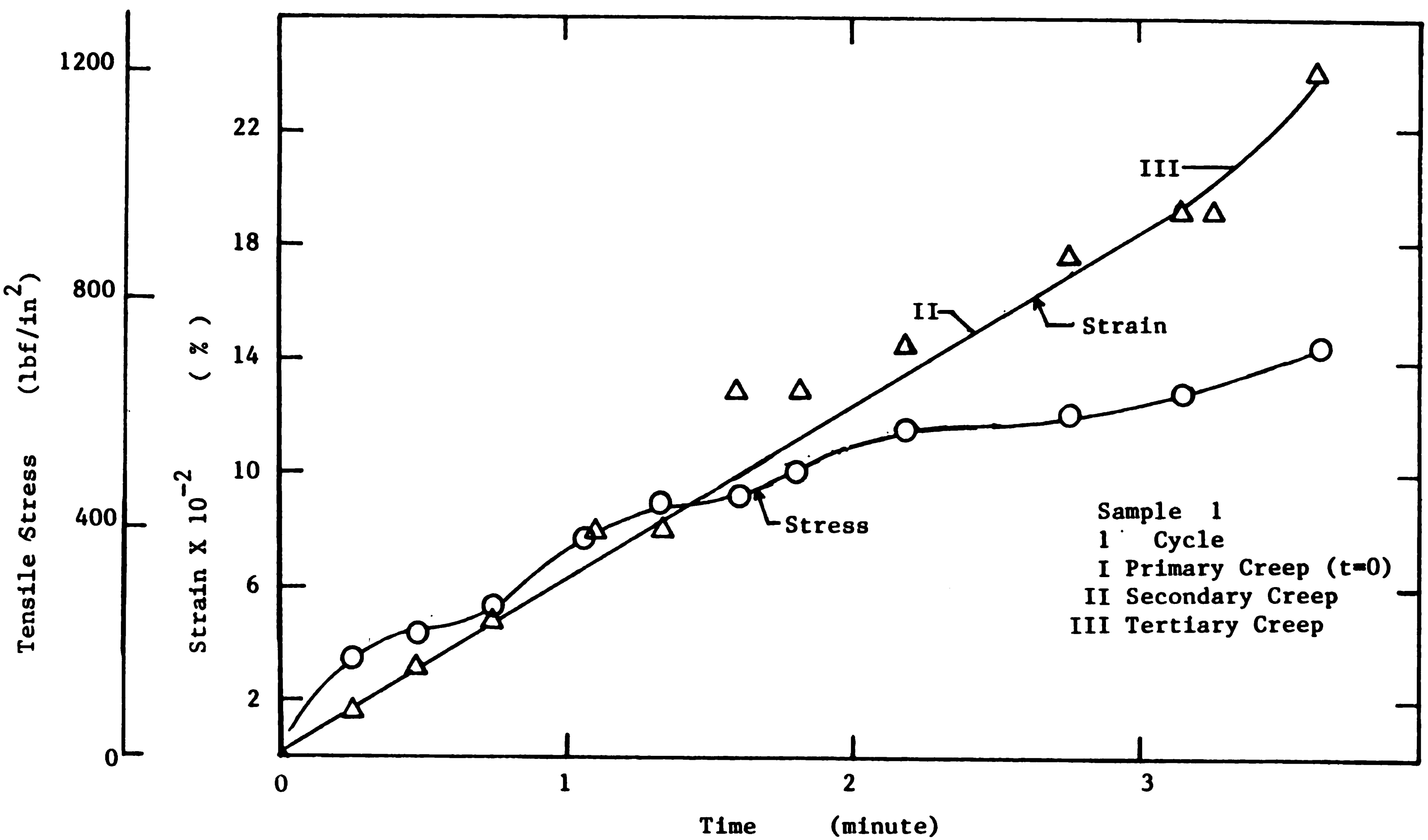

Figure 3-33: Stress and Strain vs. Time for the Tensile Test on Frozen Saturated Sand, Load Cycle 1.

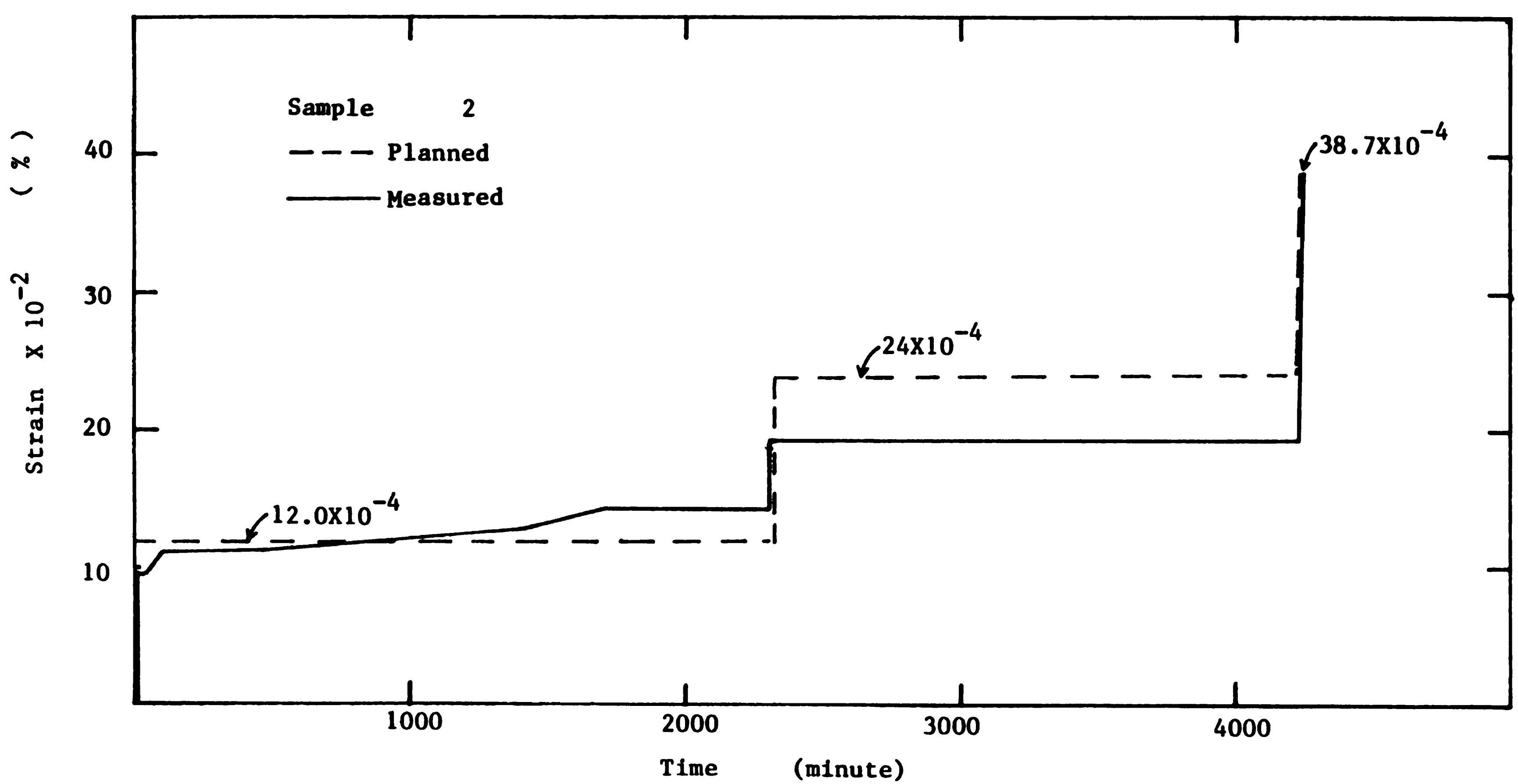

Figure 3-34: Cyclic Strain (2 cycles).

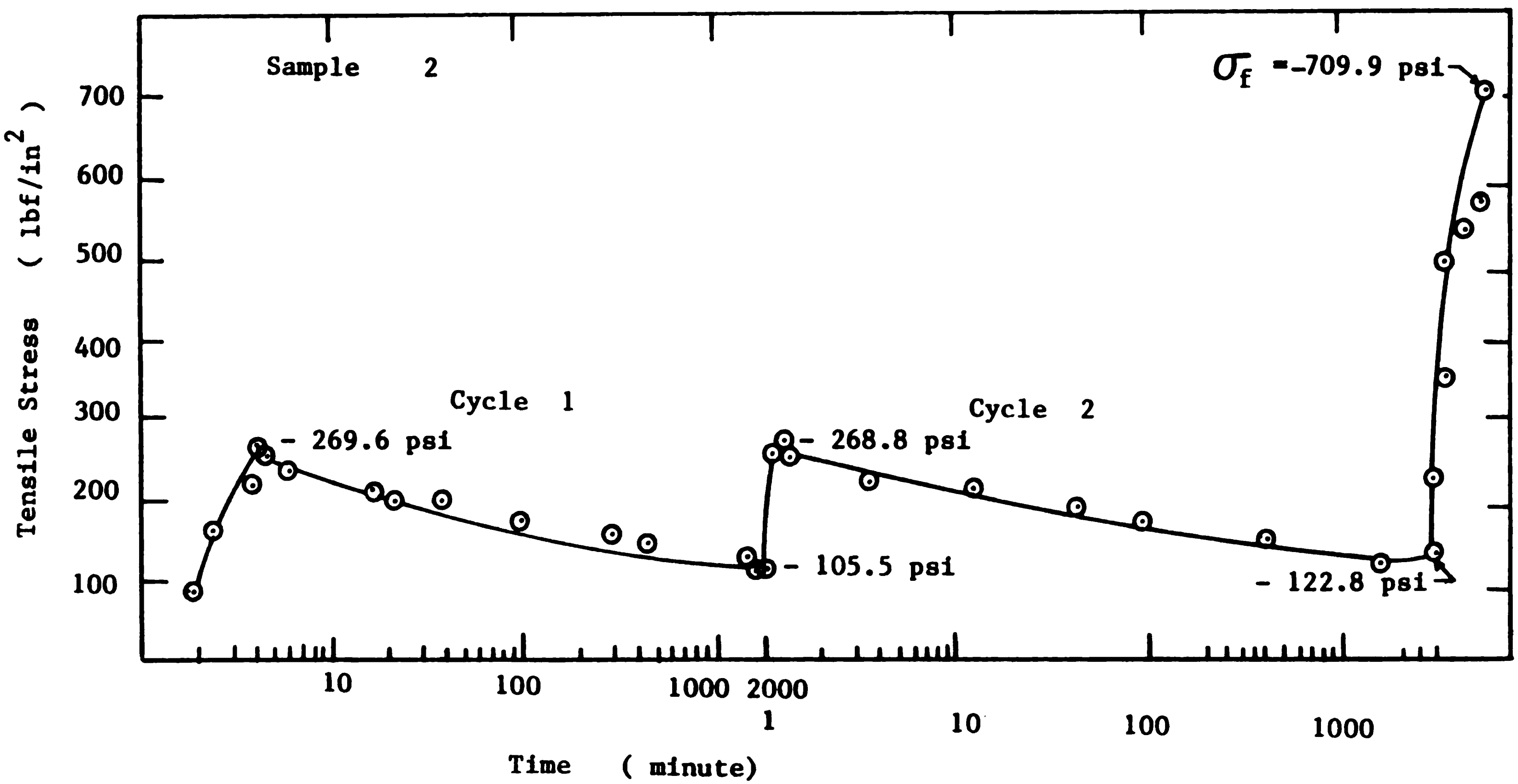

Figure 3-35: **Tensile Stress Relaxation in Frozen Saturated Sand for 2 Load Cycles.**

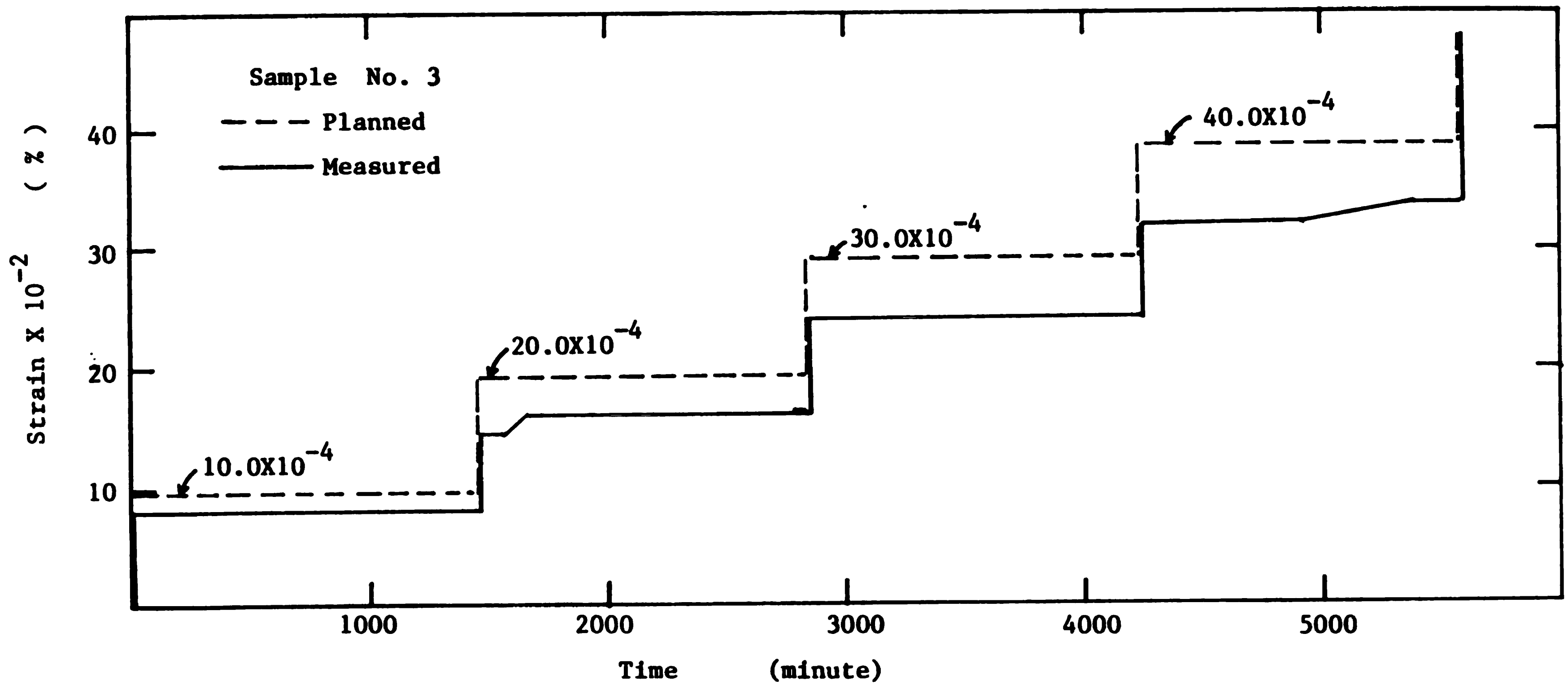

Figure 3-36: Cyclic Strain (4 cycles).

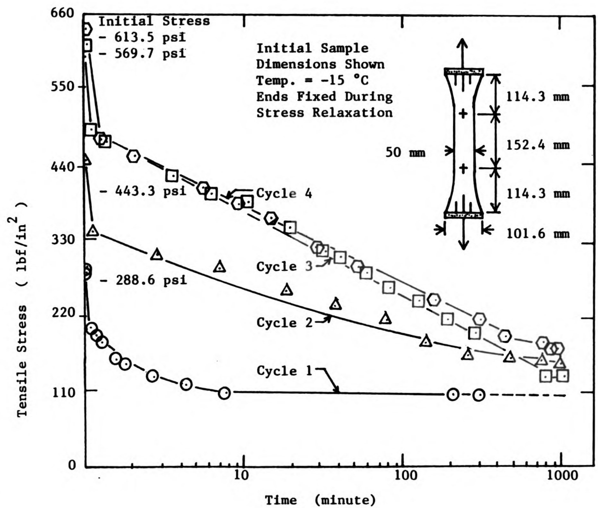

Figure 3-37: Stress Relaxation Curves at A Constant Temperature (-15 °C) for Frozen Saturated Quartz Sand After Cyclic Loading.

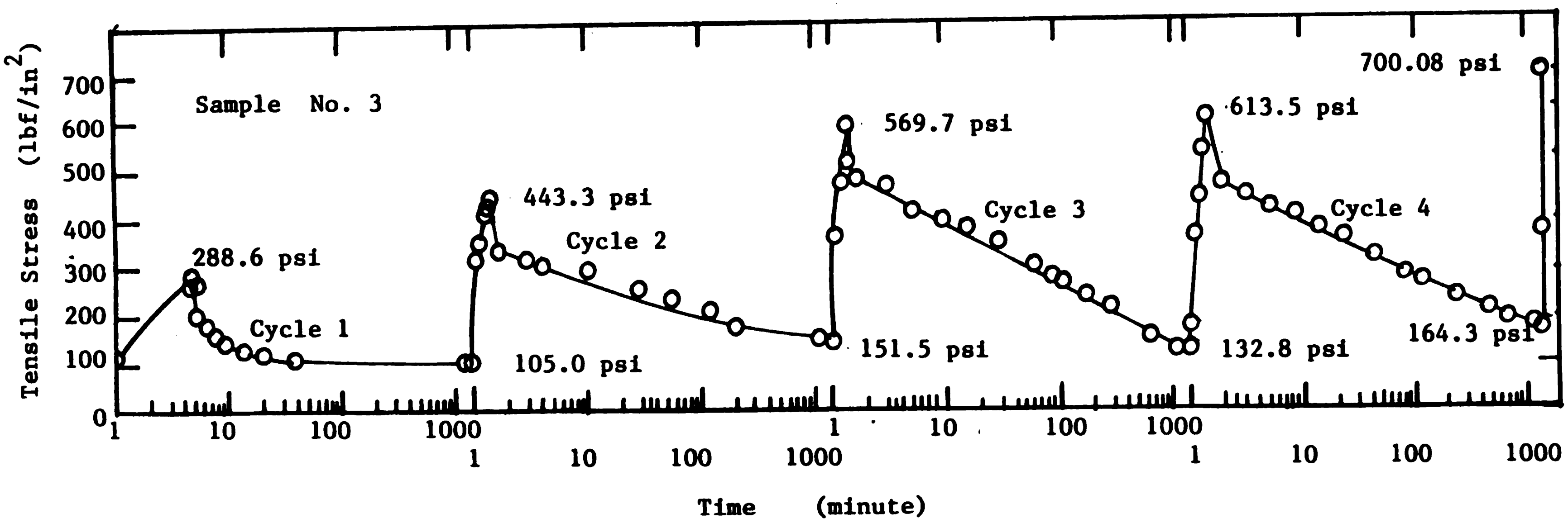

Figure 3-38: Stress Relaxation Curves for Frozen Saturated Sand at -15 °C over 4 Loading Cycles.

the tensile strength, i.e., induce stress softening. The data summary (Figure 3-39) showed that failure strains increased from 0.24 % in 1 cycle to 0.48 % in 4 cycles, an increase of 100 %. For the same series of 4 cycles the tensile strength decreased by about 3 % (Andersland and Al-Moussawi, 1988).

Table 3-4: Results from Stress Relaxation Tests on Saturated Frozen Quartz Sand at -15 °C.

Sample Number	σ_f psi	% Reduction in σ_f (%)	ε_f in/in $\times 10^{-4}$	% Increase in ε_f (%)	Cycle Number
1	722.41	0	24.19	0	1
2	709.9	1.73	38.70	60	2
3	700.80	2.99	48.38	100	4

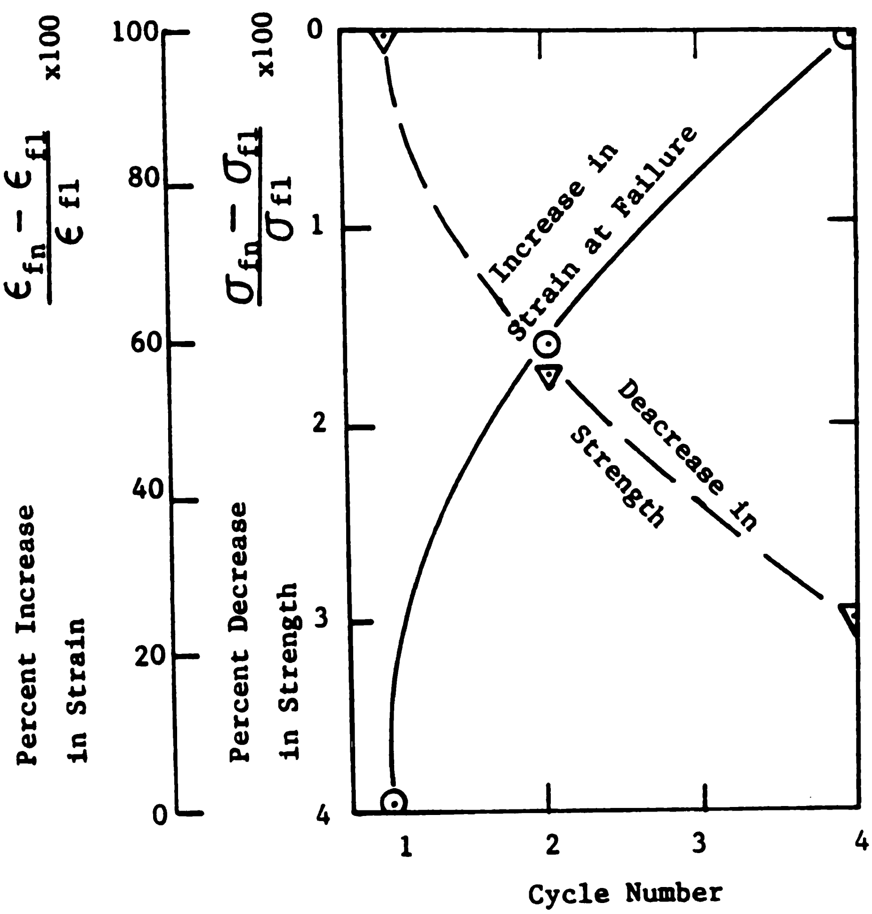

Figure 3-39: Load Cycle Effect on Failure Strain and Rupture Stress for Saturated Frozen Quartz Sand at -15 °C.

CHAPTER IV

THEORETICAL CONSIDERATIONS

4.1 Mathematical Formulation

Construction cracks in frozen soil can be considered analogous to a theoretical model of tension cracks in a semi-infinite solid. The effect of the crack in relieving tensile stress at the ground surface relates to the problem of crack spacing. The rate of energy dissipation at the advancing crack tip relates to the problem of crack depth. Even though the stress that causes cracking develops slowly, an elastic model of the stress near a crack can be useful as long as the cracks, once initiated, propagate rapidly. The crack is generally initiated on a plane of great stress (often) at or near the ground surface, and is propagated toward the interior of the medium where the tension diminishes and ultimately passes into compression.

It is well known that most soil materials behave elastically only when deformed rapidly. Thus the processes which produce tension (such as thermal contraction) could be modeled elastically. This approach gives a very good approximation to the stress conditions that exist immediately after the crack has formed.

This review of theory will serve to present expressions which describe the elastic stress in a semi-infinite solid containing a long crack of finite depth. Before the crack appears, the medium is assumed to have a nonuniform stress field with the maximum principal stress normal to the plane on which the crack will form.

The components of initial stress vary only in the direction of crack depth. The crack will be considered as lying in the plane $y = 0$ in a strip $0 < x < b$ for $x > 0$, Figure (4-1). The maximum principal stress will be represented by $\tau(x)$ which is directed parallel to the y axis and varies only with x. The x and z components of the initial stress can be assigned later, in conformity with any particular application, as only their component influences the boundary conditions at the crack walls. One can also assume that the stress vector will vanish at the surface $x = 0$.

Under conditions of plane strain the stress in the interior of an elastic body can, in the absence of body forces, be reduced to the Airy stress function $U(x, y)$ such that

$$\frac{\partial^4 U}{\partial x^4} + 2\frac{\partial^4 U}{\partial^2 x \partial^2 y} + \frac{\partial^4 U}{\partial y^4} = 0 \qquad (4\text{-}1)$$

where

$$\sigma_{xx} = \frac{\partial^2 U}{\partial y^2}, \quad \sigma_{yy} = \frac{\partial^2 U}{\partial x^2}, \quad \tau_{xy} = -\frac{\partial^2 U}{\partial x \partial y} \qquad (4\text{-}2)$$

and the Airy stress function U will lead to the prescribed stresses on the boundary. Muskhelishvili (1963) defined the analytic function of the complex variable z, namely, $\Phi_1(z)$ and $\psi_1(z)$ such that

$$\frac{\partial U}{\partial x} + i\frac{\partial U}{\partial y} = \varphi_1(z) + z\,\overline{\varphi_1'(z)} + \overline{\psi_1(z)} \qquad (4\text{-}3)$$

throughout the mass and

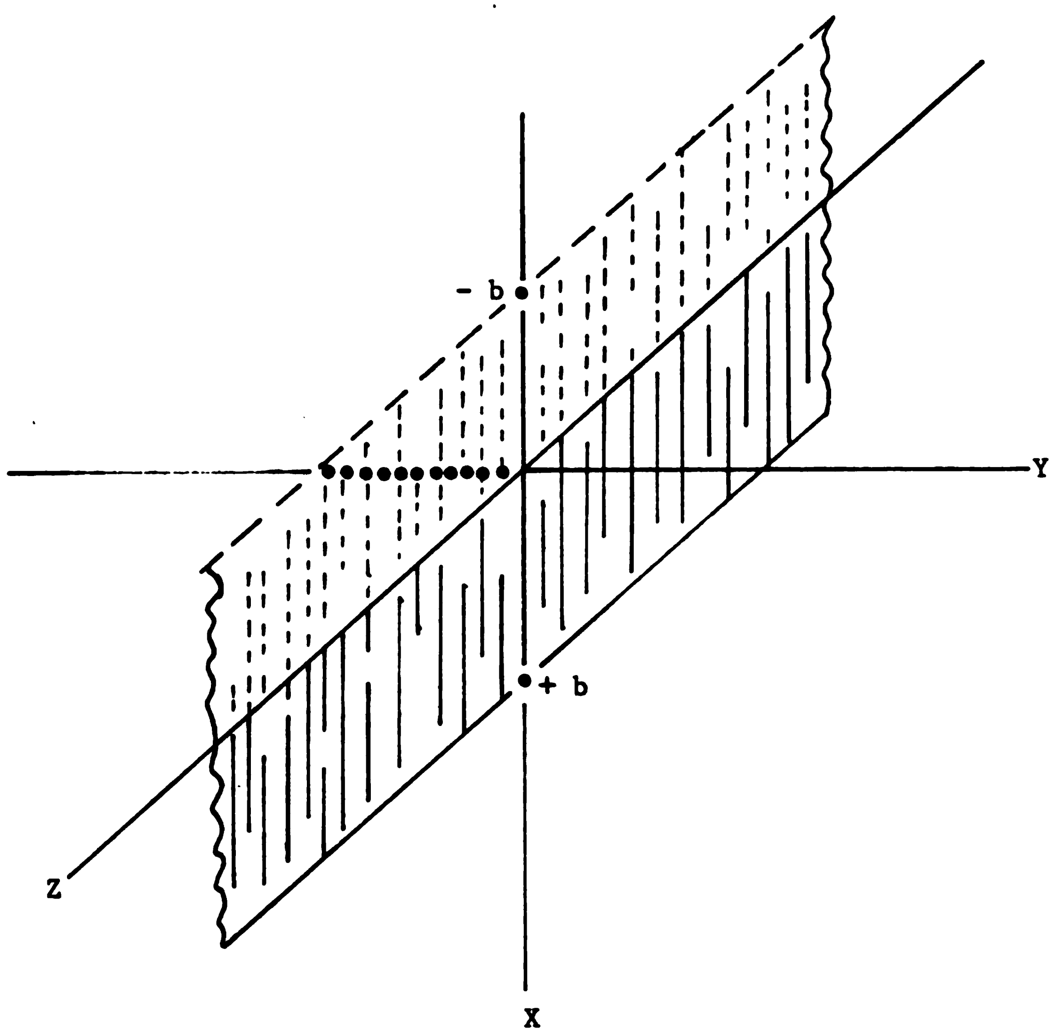

Figure 4-1: Coordinate System and Position of the Thermal Crack.

$$\frac{\partial U}{\partial x} + i\frac{\partial U}{\partial y} = f(s) \tag{4-4}$$

on the boundary L.

The prime denotes differentiation with respect to $z = x + iy$, the complex conjugate is represented by a bar, and

$$f(s) = f_1(s) + if_2(s) = i \int_0^s (X_n + iY_n)\, ds \tag{4-5}$$

where X_n and Y_n are the x and y components of the prescribed surface stresses in the direction of the positive normal on the boundary L.

The analytic functions $\Phi_1(z)$ and $\psi_1(z)$ are determined, respectively, within a complex constant and a complex linear function, by the boundary relation.

$$\varphi_1(z) + z\overline{\varphi_1'(z)} + \overline{\psi_1(z)} = i \int_0^s (X_n + iY_n)\, ds \tag{4-6}$$

The arbitrariness in Φ_1 and ψ_1, as determined by equation (4-6), represents only rigid body motion and hence equation (4-6) completely determines the state of stress in terms of surface force. Applying the complex transformation $z = \omega(\zeta)$, and setting

$$\begin{aligned} \varphi_1(z) &= \varphi_1(\omega(\zeta)) = \varphi_1(\zeta) \\ \psi_1(z) &= \psi_1(\omega(\zeta)) = \psi(\zeta) \\ \zeta &= \rho\, e^{i\theta} \end{aligned} \tag{4-7}$$

for equation (4-5) gives

$$\varphi(\zeta) + \frac{\omega(\zeta)}{\overline{\omega'(\zeta)}} \overline{\varphi'(\zeta)} + \overline{\psi(\zeta)}$$

$$= i \int_0^s (X_n + iY_n)\, ds, \qquad \zeta = \sigma \tag{4-8}$$

where σ is the value of ζ on the boundary λ in the ζ plane. By setting

$$\Phi(\zeta) = \frac{d\varphi_1(z)}{dz} = \frac{\varphi'(\zeta)}{\omega'(\zeta)} \tag{4-9}$$

and

$$\Pi(\zeta) = \frac{2\zeta^2}{\rho^2\, \overline{\omega'(\zeta)}} [\, \overline{\omega(\zeta)}\, \Phi'(\zeta) + \psi'(\zeta)] \tag{4-10}$$

one can write Muskehelishvili's (1963) general results for the components of stress referred to the curvilinear coordinates of transformation, as follows

$$\sigma_\xi + \sigma_\eta = 4\, \mathrm{Re}\, [\Phi(\zeta)] \tag{4-11}$$

$$\sigma_\eta - \sigma_\xi + 2i\tau_{\xi\eta} = \Pi(\zeta) \tag{4-12}$$

This approach is also suggested by Timoshenko and Goodier (1970), and Sih (1973). The components of stress are given explicitly by

$$\sigma_\xi = 1/2\, \{4\mathrm{Re}\, [\Phi(\zeta)] - \mathrm{Re}\, [\Pi(\zeta)]\} \tag{4-13}$$

$$\sigma_\eta = 1/2\, \{4\mathrm{Re}\, [\Phi(\zeta)] + \mathrm{Re}\, [\Pi(\zeta)]\} \tag{4-14}$$

$$\tau_{\xi\eta} = (1/2i)\, \mathrm{Im}\, [\Pi(\zeta)] \tag{4-15}$$

One can use the transformation (Muskhelishvili, 1963) in which $z = w(\zeta)$, is the analytic function. Thus

$$\omega(\zeta) = R\,(\zeta + m/\zeta), \quad R > 0, \quad m \geq 0 \tag{4-16}$$

For transformation of the exterior of an ellipse into an exterior of a unit circle

$$R = 1/2\ b \tag{4-17}$$

So that

$$z = \omega(\zeta) = (1/2)\ b\ (\zeta + m/\zeta), \quad 0 \leq m \leq 1 \tag{4-18}$$

which maps the exterior of the unit circle in the ζ plane

$$|\zeta| \geq 1$$

into the exterior of the ellipse

$$|y| \geq 1/2\ b\ (\rho - m/\rho)\ \sin\Theta \tag{4-19}$$

$$|x| \geq 1/2\ b\ (\rho + m/\rho)\ \cos\Theta \tag{4-20}$$

in the z plane, as shown in Figure (4-2). The cracking problem centers about the degenerate case $m = 1$, in which the unit circle $|\zeta| = 1$ corresponds to the double line segment $|x| < b$, $y = \pm 0$.

4.1.1 Case I: The Step Function

Consider first the case of a step distribution of self-equilibrating surface stresses on the degenerate ellipse, $m = 1$, $\rho = 1$. This case, shown in Figure (4-3), is described by

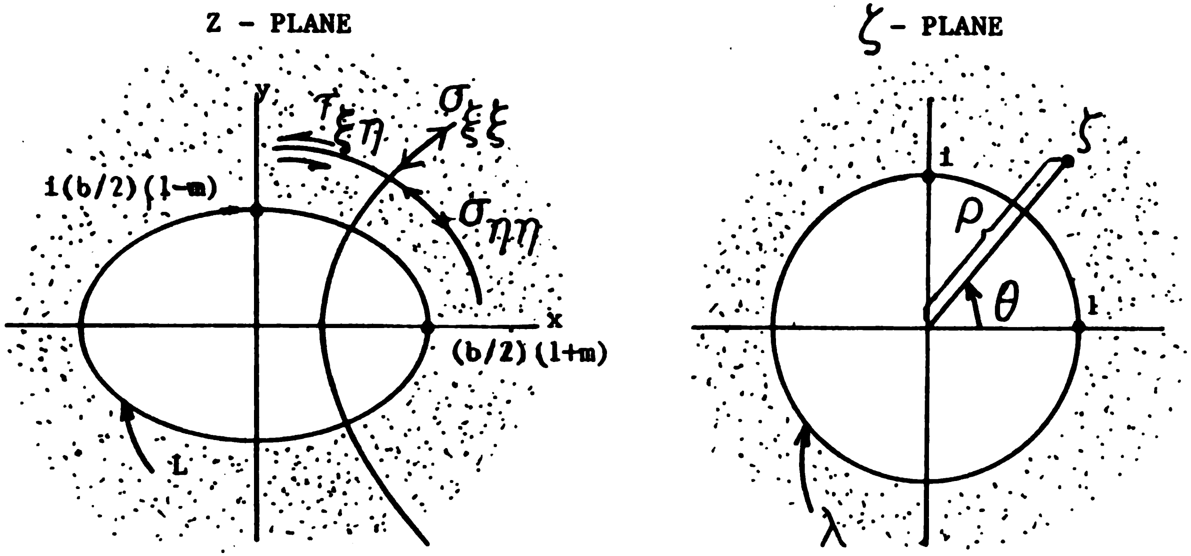

$$z = \omega(\zeta) = (1/2)\, b \left(\zeta + \frac{m}{\zeta}\right), \quad 0 \le m \le 1$$

Figure 4-2: Transformation Mapping of the Exterior of an Ellipse into the Exterior of A Unit Circle (Adapted from Muskhelelishvili, 1963).

$$Y_n = -P \qquad , \ |x| < a$$
$$\quad = 0 \qquad , \ a < |x| < b \tag{4-21}$$

$$X_n = 0$$

where P is a constant. Setting $\zeta = \sigma$ on the boundary, $\theta_0 = \cos^{-1}(a/b)$, and using the direction cosines, the surface stresses will be

$$X_n = -P_n \cos (n, x)$$

$$Y_n = -P_n \cos (n, y) \tag{4-22}$$

$$(X_n + iY_n)\, ds = -P\,(dy - idx) = iPdz \tag{4-23}$$

Substituting the surface stresses into equation 4-5 gives

$$f = i \int (X_n + iY_n)\, ds = -\,Pz = -\,PR\,(\sigma + m/\sigma) \tag{4-24}$$

For $m = 1$, $\rho = 1$, $R = 1/2\ b$ and $\zeta = \sigma$

$$\begin{aligned} f &= f_1 + if_2 = 1/2\ Pb\,(\sigma + 1/\sigma), && \begin{cases} \theta_0 < \theta < \pi - \theta_0 \\ \pi + \theta_0 < \theta < 2\pi - \theta_0 \end{cases} \\ &= Pa && -\theta_0 < \theta < +\theta_0 \\ &= -Pa && -\theta_0 + \pi < \theta < \theta_0 + \pi \end{aligned} \tag{4-25}$$

Using equation 4-8 and the general properties of the analytic function (Lachenbruch, 1961) leads to the derivation of the curvilinear stress components

$$\Phi = \frac{-Pb}{4\pi}\left\{ \frac{1}{\zeta}(2\pi-4\theta_0) + \frac{1}{i}\left(\frac{1}{\zeta} + 2\cos\theta_0 + \zeta\right)\right.$$

$$\left. \cdot \ \ln\frac{\sigma_0+\zeta}{\bar{\sigma}_0+\zeta} + \frac{1}{i}\left(\frac{1}{\zeta} - 2\cos\theta_0 + \zeta\right)\ln\frac{\sigma_0-\zeta}{\bar{\sigma}_0-\zeta}\right) \qquad (4\text{-}26)$$

and

$$\psi = \frac{-Pb}{4\pi}\left\{\frac{2\zeta}{\zeta^2-1}(2\pi-4\theta_0) + \frac{2}{i}\cos\theta_0\left[\ln\frac{\sigma_0+\zeta}{\bar{\sigma}_0+\zeta} - \ln\frac{\sigma_0-\zeta}{\bar{\sigma}_0-\zeta}\right]\right\},$$

where $\sigma_0 = e^{i\theta_0}$

After a long computation, the final result for the stress components is found to be

$$\sigma_\xi = P\left\{\frac{1}{\pi}[\alpha_4-\alpha_3+\alpha_2-\alpha_1] - \left[1-\frac{2}{\pi}\theta_0\right]\left[1-\frac{(\rho^2-1)^3(\rho^2+1)}{(\rho^4-2\rho^2\cos 2\theta+1)^2}\right]\right.$$

$$\left. + \frac{2\rho^2(\rho^4-1)\sin 2\theta_0(1-\cos 2\theta)[2\rho^2(\cos 2\theta-\cos 2\theta_0)-(\rho^2-1)^2]}{\pi(\rho^4-2\rho^2\cos 2\theta+1)[\rho^4-2\rho^2\cos 2(\theta-\theta_0)+1][\rho^4-2\rho^2\cos 2(\theta+\theta_0)+1)}\right\}$$

(4-27)

$$\sigma_\eta = P\left\{\frac{1}{\pi}[\alpha_4-\alpha_3+\alpha_2-\alpha_1] - \left[1-\frac{2}{\pi}\theta_0\right]\left[1-\frac{(\rho^4-1)[(\rho^2+1)^2 - 4\rho^2\cos 2\theta}{(\rho^4-2\rho^2\cos 2\theta+1)^2}\right]\right.$$

$$\left. - \frac{2\rho^2(\rho^4-1)\sin 2\theta_0(1-\cos 2\theta)[2\rho^2(\cos 2\theta-\cos 2\theta_0)-(\rho^2-1)^2]}{\pi(\rho^4-2\rho^2\cos 2\theta+1)[\rho^4-2\rho^2\cos 2(\theta-\theta_0)+1][\rho^4-2\rho^2\cos 2(\theta+\theta_0)+1)}\right\}$$

(4-28)

and

$$\tau_{\xi\eta} = P\{ \frac{2\rho^2(\rho^2-1)^2 \sin 2\theta}{(\rho^4 - 2\rho^2 \cos 2\theta + 1)} \quad [\frac{1 - (2/\pi)\theta_0}{(\rho^4 - 2\rho^2 \cos 2\theta + 1)}$$

$$- \frac{\sin 2\theta_0[2\rho^2(\cos 2\theta + \cos 2\theta_0) - (\rho^2+1)^2]}{\pi(\rho^4 - 2\rho^2\cos 2(\theta-\theta_0) + 1)(\rho^4 - 2\rho^2\cos 2(\theta+\theta_0) + 1)}]\} \qquad (4\text{-}29)$$

where

$$\alpha_1 = \tan^{-1} (\frac{\rho \sin \theta + \sin \theta_0}{\rho \cos \theta + \cos \theta_0}) \qquad (4\text{-}30)$$

$$\alpha_2 = \tan^{-1} (\frac{\rho \sin \theta - \sin \theta_0}{\rho \cos \theta + \cos \theta_0}) \qquad (4\text{-}31)$$

$$\alpha_3 = \tan^{-1} (\frac{\rho \sin \theta - \sin \theta_0}{\rho \cos \theta - \cos \theta_0}) \qquad (4\text{-}32)$$

$$\alpha_4 = \tan^{-1} (\frac{\rho \sin \theta + \sin \theta_0}{\rho \cos \theta - \cos \theta_0}) \qquad (4\text{-}33)$$

For the special case a = b, equations 4-27 to 4-29 reduce to those given by Muskhelishvili (1963) by setting $\theta_0 = 0$.

4.1.2 Case II: The Linear-Function

Consider the effect of a symmetrical linear distribution of normal pressures over the degenerate ellipse m = 1, $\rho = 1$, (see Figure 4-4). For this case

$$\begin{aligned} Y_n &= - (Q/b)\, x, && x > 0 \\ &= + (Q/b)\, x, && x < 0 \end{aligned} \qquad (4\text{-}34)$$

$$X_n = 0$$

where Q is an intensity parameter. Setting $\sigma = e^{i\theta}$, obtain from equation 4-5.

$$f_1 + if_2 = +1/8\ (Qb)\ (2 + \sigma^2 + 1/\sigma^2), \quad -\pi/2 < \theta < +\pi/2$$

$$= -1/8\ (Qb)\ (2 + \sigma^2 + 1/\sigma^2), \quad \pi/2 < \theta < 3\pi/2 \qquad (4\text{-}35)$$

This leads to the Lachenbruch (1961) derivation of the curvilinear stress components.

$$\varphi = +\ Qb\ \frac{1}{4\pi}[\zeta - \frac{1}{\zeta} + \frac{i}{2}\ (\zeta + \frac{1}{\zeta})^2\ \ln\frac{\zeta + i}{\zeta - i}] \qquad (4\text{-}36)$$

$$\psi = -\ Qb\ \frac{1}{4\pi}[\frac{1}{\zeta^2 - 1}\ (\zeta^3 + 6\zeta + \frac{1}{\zeta}) + i\frac{(\zeta^2 + 1)^2}{2\zeta^2}\ \ln\frac{\zeta + i}{\zeta - i}]$$

and finally

$$\sigma_\xi = \frac{+Q}{\pi(\rho^4 - 2\rho^2 \cos 2\theta + 1)}\{2(\rho^4-1)\ [1 - \frac{(\rho^2+1)^2 \sin^2\theta + 4\rho^2 \sin^4\theta}{\rho^4 - 2\rho^2 \cos 2\theta + 1)}]$$

$$- \frac{(\rho^2-1)^3}{4\rho}(\sin\theta + \sin 3\theta)\ \ \ln[\frac{\rho^2 + 2\rho \sin\theta + 1}{\rho^2 - 2\rho \sin\theta + 1}]$$

$$- \frac{1}{2\rho}\ [(\rho^6 + \rho^4 + \rho^2 + 1) \cos\theta$$

$$- (\rho^6 - 3\rho^4 - 3\rho^2 + 1) \cos 3\theta](\beta_1 - \beta_2)\} \qquad (4\text{-}37)$$

$$\sigma_\eta = \frac{+Q}{\pi(\rho^4 - 2\rho^2 \cos 2\theta + 1)}\{2(\rho^4-1)\ [1 + \frac{(\rho^2+1)^2 \sin^2\theta + 4\rho^2 \sin^4\theta}{\rho^4 - 2\rho^2 \cos 2\theta + 1)}]$$

$$- \frac{1}{4\rho} (\rho^2+1)(\rho^4-1)[3 \sin \theta - \sin 3\theta] \ln[\frac{\rho^2 + 2\rho \sin \theta + 1}{\rho^2 - 2\rho \sin \theta + 1}]$$

$$- \frac{1}{2\rho} [(3\rho^6 - \rho^4 - \rho^2 + 3) \cos \theta$$

$$- (\rho^6 + \rho^4 + \rho^2 + 1) \cos 3\theta](\beta_1 - \beta_2)\} \qquad (4\text{-}38)$$

$$\tau_{\xi\eta} = \frac{-2Q(\rho^2-1) \sin \theta}{\pi(\rho^4 - 2\rho^2 \cos 2\theta + 1)} \{\frac{(\rho^2-1) \cos \theta[(\rho^2-1)^2 - 4\rho^2 \cos^2 \theta]}{\rho^4 - 2\rho^2 \cos 2\theta + 1}$$

$$- \frac{1}{4\rho} (\rho^4-1) \sin 2\theta \ln[\frac{\rho^2 + 2\rho \sin \theta + 1}{\rho^2 - 2\rho \sin \theta + 1}]$$

$$- \frac{1}{2\rho} [(\rho^4+1) \cos 2\theta - 2\rho^2](\beta_1 - \beta_2)\} \qquad (4\text{-}39)$$

where

$$\beta_1 = \tan^{-1} (\frac{\rho \sin \theta + 1}{\rho \cos \theta}) \qquad (4\text{-}40)$$

$$\beta_2 = \tan^{-1} (\frac{\rho \sin \theta - 1}{\rho \cos \theta}) \qquad (4\text{-}41)$$

4.1.3 Tension Crack in an Infinite Medium

The problem of a stress-free crack interior to a totally infinite medium is considered in this section. Consider first case I, the step function. For this case the initial tensile stress is a constant, P, throughout a layer of half-width a, and the crack extends to $x = \pm b$, where b can be greater or less than a (see Figure 4-3). Thus

$$\begin{aligned} \tau(x) &= P, \qquad |x| < a \\ &= 0, \qquad |x| > a \end{aligned} \tag{4-42}$$

Interest relative to the thermal crack problem centers about the stress perturbation in the plane $x = 0$, since this is the plane in which cracks are assumed to originate. The result is obtained by setting $\theta = \pi/2$ in equations 4-27, 4-28, and 4-29, thus

$$\sigma_\xi(\frac{\pi}{2}) = -P\{[1 - \frac{2}{\pi}\theta_0][1 - \frac{(\rho^2-1)^3}{(\rho^2+1)^3}] - \frac{2}{\pi}\tan^{-1}(\frac{\sin 2\theta_0}{\rho^2 + \cos 2\theta_0}$$

$$+ \frac{4\rho^2(\rho^2-1)\sin 2\theta_0}{\pi(\rho^2+1)(\rho^4 + 2\rho^2 \cos 2\theta_0 + 1)} \tag{4-43}$$

$$\sigma_\eta(\frac{\pi}{2}) = -P\{[1 - \frac{2}{\pi}\theta_0][1 - \frac{(\rho^2-1)[(\rho^2+1)+4\rho^2]}{(\rho^2+1)^3}] - \frac{2}{\pi}\tan^{-1}(\frac{\sin 2\theta_0}{\rho^2 + \cos\theta_0})$$

$$- \frac{4\rho^2(\rho^2-1)\sin 2\theta_0}{\pi(\rho^2+1)(\rho^4 + 2\rho^2 \cos 2\theta_0 + 1)}\} \tag{4-44}$$

$$\tau_{\xi\eta} = 0 \tag{4-45}$$

where

$$y = 1/2\ b(\rho - 1/\rho), \qquad \Theta_0 = \cos^{-1}(a/b),$$

$\sigma_\xi(\pi/2)$ represents the tangential stress in the plane $x = 0$, i.e., the stress directed parallel to the y axis, $\sigma_\eta(\pi/2)$ is the normal stress (parallel to the x axis), and $\tau_{\xi\eta}(\pi/2)$ is the shear stress in the xy plane at $x = 0$.

For case II, the linear function, the initial tension in the medium is a linear function of $|x|$ (see Figure 4-4), thus

$$\tau(x) = (Q/b)\ |x| \tag{4-46}$$

Perturbation in the plane $x = 0$ is caused by a stress-free crack extending between $x = \pm b$ and is given by setting $\Theta = \pi/2$ in equation 4-37, 4-38, and 4-39, so that

$$\sigma_\xi = -\frac{8}{\pi} Q \frac{\rho^2(\rho^2 - 1)}{(\rho^2 + 1)^3} \tag{4-47}$$

$$\sigma_\eta = -\frac{4}{\pi} Q \frac{(\rho^2 - 1)}{(\rho^2 + 1)} \{1 + \frac{2\rho^2}{(\rho^2+1)^2} - \frac{(\rho^2+1)^2}{2\rho} \ \ln \frac{\rho^2+1}{\rho^2-1}\} \tag{4-48}$$

$$\tau_{\xi\eta} = 0 \tag{4-49}$$

By superimposing a linear combination of solutions for case 1, it is possible to achieve an approximation of any desired accuracy to the effect of an arbitrary symmetrical distribution of normal forces on a crack of finite depth, 2b, interior to an infinite medium under

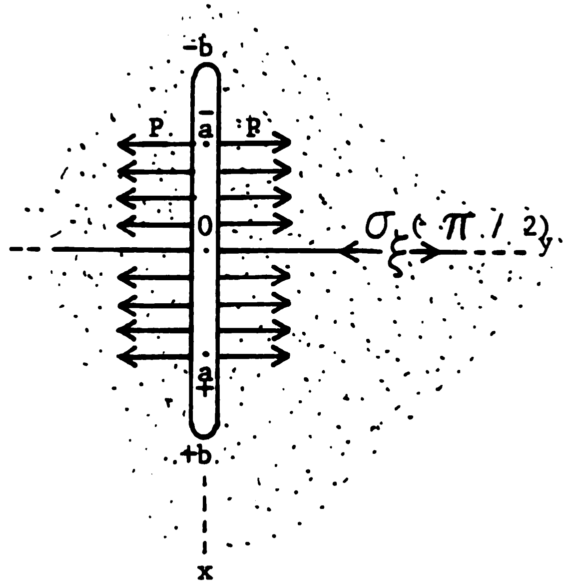

Figure 4-3: Case I: Step Function (Stress Distribution).

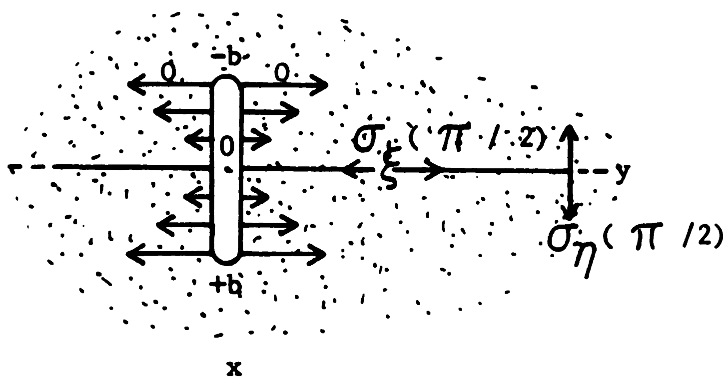

Figure 4-4: Case II: The Linear Function (Stress Distribution).

conditions of plane strain. Using results for case 2 simplifies the procedure if the function to be approximated is nearly linear.

For the above results, negative stresses are compressive, and positive stresses are tensile. P and Q are positive for compressive normal stresses on the crack surfaces.

For most applications the concern is with crack surfaces free of stress. To satisfy this condition the above solutions are superimposed on the stress that exists before cracking occurs. Thus, if the horizontal stress in the y direction at the time of cracking is $\tau(x)$ and is independent of y and z, the stresses in xy plane, after cracking, are obtained by superimposing on $\tau(x)$ the effect of the surface stresses $-\tau(x)$, distributed over the fracture surface.

4.1.4 Tension Crack at the Free Surface of a Semi-Infinite Medium

Most contraction cracks in frozen surface soils, which extend downward from the ground surface, can be assumed to be free of stress. A more realistic model of these phenomena, compared to the model in the preceding section, requires that normal stresses across the surface $x = 0$ be removed. In the present notation the stresses $\sigma_\eta(\pi/2)$ must be removed.

To illustrate the method, consider the solution of case 1 in the half-space. The procedure is illustrated schematically in Figure (4-5) which shows a step distribution of normal pressure, $-\tau(x)$, on the walls of the crack and its associated normal stresses, $\sigma_\eta(\pi/2)$, at $x = 0$ as given by equation (4-44). To nullify the normal stress, $\sigma_\eta(\pi/2)$, equal and opposite pressures $-\sigma_\eta(\pi/2)$ are applied at $x = 0$ as shown in Figure (4-5b). These pressures have the direct effect of changing the

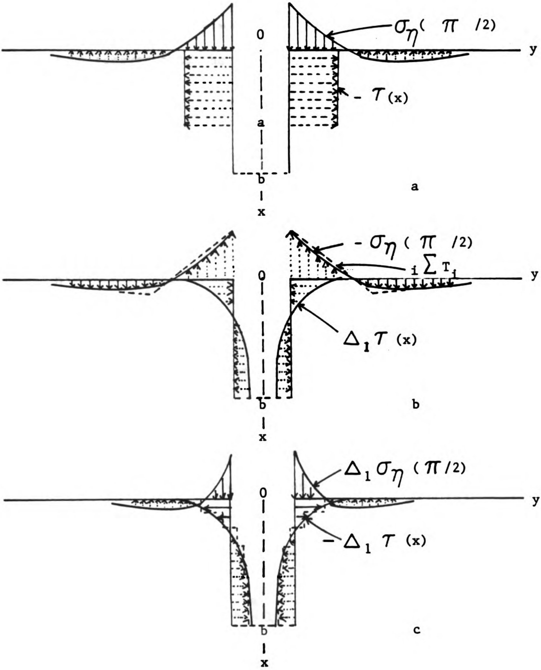

Figure 4-5: Reduction of The Solution for A Step Distribution of Stress on the Walls of A Crack in a totally Infinite Medium to the Corresponding Solution for a Semi-Infinite Medium (Lachenbruch, 1961).

horizontal surface stress from $\sigma_\xi(\pi/2)$ to $\sigma_\xi(\pi/2) - \sigma_\eta(\pi/2)$ at $x = 0$ for $y > 0$ and the indirect effect of producing new normal stresses, $\Delta_1\tau(x)$, at the walls of the fracture $y = \pm 0$, $0 < x < b$. These new stresses $\Delta_1\tau(x)$, must be removed from the fracture surface in order to maintain the initial step distribution of normal stress. This requires a method for computing $\Delta_1\tau(x)$ from $-\sigma_\eta(\pi/2)$. To do this $-\sigma_\eta(\pi/2)$ is approximated by a continuous even function of y composed of linear segments shown by broken lines in Figure (4-5b).

This gives

$$\sigma_\eta(\pi/2) \approx \sum_i T_i \tag{4-50}$$

where $T_i = P_i\,(1 - |y|/c_i)$ for, $|y| < c_i$ and

$T_i = 0$ for, $|y| > c_i$

Each term in equation 4-50 corresponds to a triangular distribution of normal pressures of half-width c_i centered at $y = 0$ on the plane $x = 0$. Starting with equation 4-1, and an assumed function which satisfies the equilibrium and compatibility equations, Carothers (1920) gave the solution for the new stresses at the fracture surface as

$$\Delta_1\tau(x) \approx -\frac{2}{\pi}\sum_i P_i\,\{\tan^{-1}\frac{c_i}{x} - \frac{x}{c_i}\ln\,[\frac{c_i^2}{x^2} + 1]\} \tag{4-51}$$

Having calculated $\Delta_1\tau(x)$, now remove it from the fracture face by applying normal stresses $-\Delta_1\tau(x)$. This is done by approximating $-\Delta_1\tau(x)$ by a step function, the effects of which can be described by a linear combination of solutions to case 1 of the preceding section (see Figure 4-5c). Removal of $\Delta_1\tau(x)$ results in a direct contribution $\Delta_1\sigma_\xi(\pi/2)$ to the tangential stress at $x = 0$. This is given by a linear combination of expressions of the form of equation 4-43.

The horizontal stress then becomes $\sigma_\xi(\pi/2) - \sigma_\eta(\pi/2) + \Delta_1\sigma_\xi(\pi/2)$ for $x = 0$, and $y > 0$. In addition, a new normal stress $\Delta_1\sigma_\eta(\pi/2)$, given by equation 4-44, appears on $x = 0$. However, $\Delta_1\sigma_\eta(\pi/2)$ decays much more rapidly with y than did the original normal stress $\sigma_\eta(\pi/2)$.

To refine the approximation, $- \Delta\sigma_\eta(\pi/2)$ is represented by an expression of the form of equation 4-50, and the entire process is repeated. All components of the stress in the medium bounded by the free surface $x = 0$ with the prescribed stress $-\tau(x)$ on the crack surfaces $y = \pm 0$, $0 < x < b$, may be approximated by superposition of the tensor components of the stresses resulting in the infinite medium from the surface stresses $-\tau(x)$, $-\sigma_\eta(\pi/2)$, $-\Delta_1\tau(x)$, $\Delta_1\sigma_\eta(\pi/2)$, etc. At present our interest centers on the horizontal stress at the free surface $x = 0$, which will be denoted by $\sigma_\xi^*(\pi/2)$. For N applications of the cycle described above, it is given by

$$\sigma_\xi^*(\pi/2) \approx \sum_{i=0}^{N} \{\Delta_i\sigma_\xi(\pi/2) - \Delta_i\sigma_\eta(\pi/2)\} \tag{4-52}$$

$$\text{for } x = 0, \quad y > 0$$

where $\Delta_0\sigma_\xi(\pi/2) = \sigma_\xi(\pi/2)$ and $\Delta_0\sigma_\eta(\pi/2) = \sigma_\eta(\pi/2)$

Values of $\sigma_\xi^*(\pi/2)$ for case 1 are summarized in Table (4-1) and are illustrated in Figure (4-6). For the linear distribution, case 2, values of $\sigma_\xi^*(\pi/2)$ are given by Table (4-2) and Figure (4-7). These numerical results are of course, approximate and unlike the results of the previous section, which were derived from exact solutions.

Table 4-1: Case 1, Step Function. Normalized Tangential Stress $\sigma_{\xi}*(\pi/2)/P$, on the Free Surface ($x = 0$) near a Crack of Depth b in a Semi-infinite Medium (Lachenbruch, 1961).

	a/b						
y/b	0.05	0.1	0.2	0.3	0.5	0.75	1.0
.05	−0.99						
.125	−0.68	−0.98					
.25	−0.36	−0.68	−0.98				
.5	−0.18	−0.36	−0.68	−0.89			
.75	−0.12	−0.24	−0.50	−0.67	−0.87		
1.0	−0.087	−0.18	−0.37	−0.51	−0.71	−0.88	−0.94
1.5	−0.051	−0.11	−0.21	−0.31	−0.45	−0.60	−0.65
2.0	−0.033	−0.065	−0.13	−0.20	−0.31	−0.40	−0.45
2.5	−0.024	−0.050	−0.10	−0.15	−0.22	−0.29	−0.32
3.0	−0.017	−0.034	−0.075	−0.11	−0.16	−0.22	−0.24
4.0	−0.010	−0.020	−0.040	−0.059	−0.088	−0.12	−0.15
5.0	−0.006	−0.012	−0.025	−0.036	−0.061	−0.082	−0.097
7.0	−0.003	−0.006	−0.014	−0.021	−0.029	−0.042	−0.049
10.0	−0.001	−0.003	−0.005	−0.008	−0.014	−0.020	−0.023

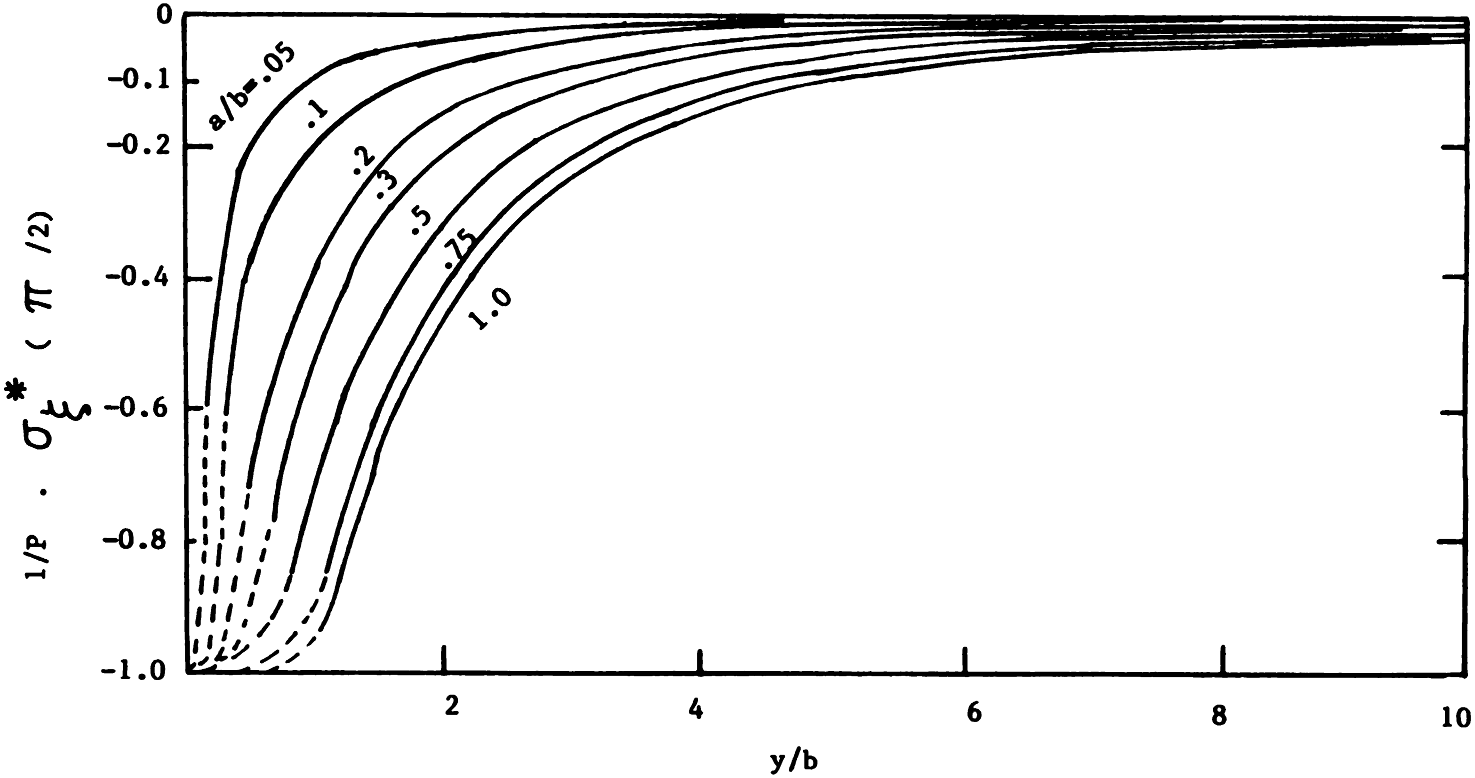

Figure 4-6: Tangential Stress on the Free Surface (x = 0) Due to A Step Distribution of Surface Stress on the Walls of a Crack (y = 0 $\pm$, 0 <x <b) in A Semi-infinite Medium (Lachenbruch, 1961).

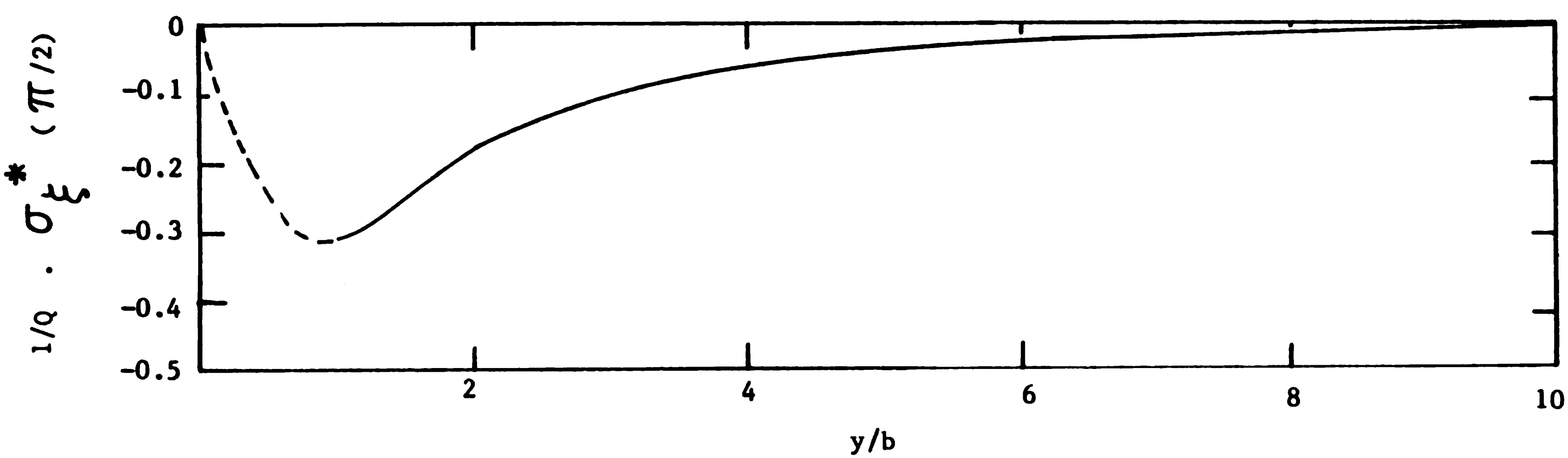

Figure 4-7: Tangential Stress on the Free Surface ($x = 0$) Due to a Linear Distribution of Surface Stress on the Walls of A Crack ($y = 0 \pm$, $0 < x < b$) in A Semi-infinite Medium (Lachenbruch, 1961).

Table 4-2: Case 2, Linear Function. Normalized Tangential Stress $\sigma_\xi^*(\pi/2)/Q$, on the Free Surface ($x = 0$) near a Crack of Depth b in a Semi-infinite Medium (Lachenbruch, 1961).

y/b	$\sigma_\xi^*(\pi/2)/Q$
0.50	-0.25
0.75	-0.30
1.0	-0.31
1.5	-0.25
2.0	-0.17
2.5	-0.13
3.0	-0.10
4.0	-0.056
5.0	-0.040
7.0	-0.018

4.2 Thermal Contraction and Fracture

4.2.1 The Elastic Problem

Vertical cracks form when tensile stresses exceed the frozen soil tensile strength. With colder temperatures and greater contraction at the ground surface (semi-infinite soil mass), the cracks will propagate downward into the frozen soil. Tensile stresses in the adjacent soil are reduced so as to give a crack spacing with stress over the entire surface reduced below the tensile strength of the frozen ground. With an increase in depth and overburden pressures, hydrostatic compressive stresses increase until they exceed the thermal tensile stresses. For these conditions, to what depth will the crack develop? How does crack development, with formation of new boundary conditions, alter the stress components? The problem can be formally stated in terms of the following boundary conditions:

$$\sigma_\xi(x,\, 0) = -\tau^*(x), \qquad y = 0, \quad 0 < x < b \qquad (4\text{-}53)$$

$$\sigma_\xi,\, \sigma_\xi,\, \tau_{\xi\eta} \longrightarrow 0 \qquad x,\, y \longrightarrow \infty \qquad (4\text{-}54)$$

$$v(x,\, 0) = 0 \qquad y = 0, \quad x > b \qquad (4\text{-}55)$$

$$\sigma_\eta(0,\, y),\ \tau_{\xi\eta}\,(0,\, y) = 0 \qquad x = 0 \qquad (4\text{-}56)$$

$$w(x,\, y) = 0 \qquad \text{all } x,\, y \qquad (4\text{-}57)$$

where v and w are displacements in the y and z directions, respectively. When the crack forms at $y = 0$ to a depth b, horizontal stress on the crack surface in the y direction must go to zero. This is formally satisfied by superposing a normal stress $\sigma_\xi(x, 0) = \tau^*(x)$ on the two crack surfaces as stated in equation 4-53. Equation 4-55 states that the crack penetrates only to a depth $x = b$. Equation 4-56 states that stress goes to zero at the horizontal ground surface. Equation 4-57 states that the medium is constrained in the direction of the crack such that the problem is one of plane strain.

Consider the horizontal stress relief at the ground surface in the direction normal to the crack, $\sigma_\xi(0, y)$. Equations 4-53 through 4-57 were solved using Muskebelishvili´s (1963) method as described in section 4.1. Consider first case 1 with a step pressure distribution of magnitude P, to the depth a, on the crack surface, i.e.,

$$\begin{aligned} \sigma_\xi(x,\, 0) &= -P\,, \qquad 0 < x < a < b, \quad y = 0 \qquad (4\text{-}58)\\ &= 0\,, \qquad a < x < b, \qquad y = 0 \end{aligned}$$

The corresponding values of stress relief at the ground surface, $\sigma_\xi(0, y)$ are summarized in Figure (4-6).

To illustrate use of these curves, assume that at the instant before fracture, the ground has a unit tension to some depth a, and no stress below a, i.e.,

$$\tau^*(x) = +1\ , \qquad 0 < x < a$$
$$= 0\ , \qquad a < x$$

Now assume that a crack forms and penetrates to a depth equal to twice the thickness of the stressed layer, i.e., $b = 2a$. The crack will relieve the tension at the ground surface as shown by curve $a/b = 0.5$ in Figure (4-6). Thus, at a horizontal distance of two crack depths ($y/b = 2$), formation of the crack will result in an instantaneous reduction of tension by 30 percent. Theoretical results in Figure (4-6) shows for a given crack depth, that the stress relief width is strongly dependent upon the depth-distribution of stress $\tau^*(x)$ at the time of fracture.

Consider the effect of varying the fracture depth b. Increasing b will reduce the ratio a/b. The lower a/b ratio will lower the percent stress relief as shown in Figure 4-6. In general, for a given initial stress distribution $\tau^*(x)$, the width of the zone of stress relief increases appreciably with increasing depth of the fracture.

For case 2 with a linear function, Equation 4-47 and Figure (4-7) shows that the stress relief, and the width of the zone of the stress relief, is dependent on crack depth b and the pressure Q at the bottom of the crack. An increase in crack depth b will reduce the y/b ratio which will in turn increase the percent stress relief as shown for $y/b > 1$ in Figure (4-7).

4.2.2 Crack Stress Intensity Factor

For the fracture process, the most important quantity to be derived from a stress analysis is the stress intensity across the plane of fracture in the neighborhood of the crack tip. In particular, the stress component σ_y in the crack tip vicinity must be determined. The stress-intensity factor K_I for a mode I crack is then defined

$$K_I = \lim_{r \to 0} (\sigma_y(r, 0) \sqrt{2\pi r}) \tag{4-59}$$

where r is the radial distance from crack tip (Hellan, 1984). The parameter K_I depends on the crack length and stress distribution in the soil medium. To determine K_I for problems under consideration, it is necessary to investigate the limit of $\sigma_\eta(\theta = 0)$ as $\rho \to 1$ where $\rho = 1$ and $\theta = 0$ are the coordinates of the crack tip. When stresses on the crack surface are represented by a step function for case 1, equation 4-28 yields

$$\sigma_\eta(0) = \lim_{\rho \to 1} \frac{2P}{\rho^2-1} \{1 - \frac{2}{\pi} \theta_0\} + \text{constant} \tag{4-60}$$

From equation 4-18 and Figure (4-2), it can be shown that as $\rho \to 1$, $r \to 0$, and

$$\frac{1}{\rho^2 - 1} \to \frac{\sqrt{b}}{2} \frac{1}{\sqrt{2r}} \tag{4-61}$$

Using equation 4-61 and $\theta_0 = \cos^{-1} a/b$ gives

$$\sigma_\eta = \lim_{r \to 0} p\sqrt{b} [1 - (2/\pi) \cos^{-1} (a/b)] 1/\sqrt{2}r + \text{constant} \tag{4-62}$$

where p is the tensile stress distribution on the crack surface, b is crack depth, and a is depth for stress distribution p. Using equations 4-59 and 4-62 leads to

$$K_I = p\sqrt{b}\,[1 - (2/\pi)\cos^{-1}(a/b)] \tag{4-63}$$

When stresses on the crack surface are represented by a linear function

$$\sigma_\eta = \lim_{r \to 0} (2Q/\pi)\,\frac{\rho^2 + 1}{\rho^2 - 1} + \text{constant} \tag{4-64}$$

where Q is the tensile stress (linear distribution) and ρ is the radius of curvature for the crack surface. Use of a linear stress function with equation 4-59 leads to

$$K_I = Q\sqrt{b}\,(2/\pi) \tag{4-65}$$

Along with Lachenbruch's (1961) solution for stress intensity factors, Sih (1973) summarized, in his handbook, stress-intensity factors for various cases. A combination of these cases and superposition permit use of these factors with the stress distribution on the crack surface of interest. For example, consider a partially loaded edge crack in a semi-infinite mass (Hartranft and Sih, 1973; Sih, 1973). Introduce K_I with F(a/b) as given in Table (4-4) for various values of (a/b). Then

$$K_I = 2/\pi \cos^{-1} a/b\,[1 + F(a/b)]\,\sigma\sqrt{b} \tag{4-66}$$

Koiter (1965), and Koiter and Benthem (1973) introduced the stress intensity factor K_I for stress distribution on a crack surface in a semi-infinite sheet (Figure 4-9) as

$$K_I = (1.1215\,\sigma_1 + 0.439\,\sigma_2)\sqrt{b} \tag{4-67}$$

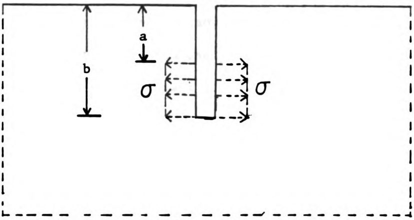

Figure 4-8: Partially Loaded Edge Crack Where F (a/b) is Given in Table (4-3) for Values of (a/b) (Sih, 1973).

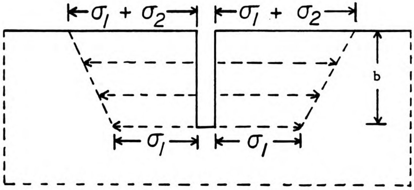

Figure 4-9: Crack in A Semi-Infinite Sheet (Koiter, 1973).

where b is crack length, σ_1 is stress at the crack tip, and $(\sigma_1 + \sigma_2)$ is stress at the mouth of the crack. For comparison, Sih's (1973), Koiter and Benthem's (1973), and Lachenbruch's (1961) stress intensity factors will be used later in the field example.

For the case of a crack extending downward from the surface of a semi-infinite medium, as described in the preceding section, it appears that K_I can be approximated as follows:

$$K_I \approx K_I(-\tau) + K_I(-\Delta_1\tau) + K_I(-\Delta_2\tau) + \ldots. \tag{4-68}$$

where $K_I(-\tau)$ is the value associated with stress distribution of $(-\tau)$ on the crack surface. Values of K_I, for a semi-infinite body, are presented in normalized form in Table (4-4) for both the linear and step functions.

Table 4-3: Values of F(a/b) as a Function of (a/b) (Hartranft and Sih, 1973).

a/b	F(a/b)	a/b	F(a/b)
0.0	0.12147	0.6	0.04624
0.1	0.10984	0.7	0.03408
0.2	0.09733	0.8	0.02244
0.3	0.08443	0.9	0.01383
0.4	0.07150	1.0	0.00000
0.5	0.05874		

Table 4-4: Normalized Crack-Edge Stress-Intensity Factor γ (Lachenbruch, 1961).

1. Step Function, Case 1

a/b	$\gamma(a/b) = K_I(a/b)/P\sqrt{b}$ + Infinite Body °	Semi-Infinite Body ° *
0.05	0.0317	0.04
0.1	0.0635	0.08
0.2	0.1285	0.16
0.3	0.1940	0.24
0.5	0.3335	0.41
0.75	0.5399	0.64
1.0	1.0000	1.1

2. Linear Function, Case 2

$\gamma(a/b) = K_I(a/b)/P\sqrt{b}$ #

Infinite Body	Semi-Infinite Body
0.6366	0.68

Notes:

+ $K_I = p\sqrt{b} \quad [1 - 2/\pi \cos^{-1} a/b]$

\# $K_I = Q\sqrt{b}\,(2/\pi)$

* $K_I \approx K_I(-\tau) + K_I(-\Delta_1\tau) + K_I(-\Delta_2\tau) + \ldots.$

° Infinite body (Exact solution)

° Semi-Infinite body (Approximate solution)

The stress intensity factor K_I, depends on the assumptions made in derivation of equation 4-59. In general, for uniform tension on the edge crack, the normalized value of K_I is in agreement with different methods used to calculate K_I from 1958 up to 1973 as shown in Table (4-5). The calculation for a normalized K_I, used by Hartranft and Sih (1973), is more reliable since they used different methods to check the results. Their results will be used later in the field example.

Table 4-5: K_I Values For Uniform Tension on an Edge Crack (Hartranft and Sih, 1973).

Source	$K_I/\sigma\sqrt{b}$
Irwin, 1958	1.1
Bueckner, 1960	1.13
Koiter, 1965	1.1215
Wigglesworth, 1957	1.122
Lachenbruch, 1961	1.1
Stallybrass, 1970	1.1215
Senddon, 1971	1.1215
Sih and Hartranft, 1973	1.1215

4.2.3 Crack Depth

To investigate some implied relationships between crack depth, stress distribution, and material properties, consider the simple case of a semi-infinite solid in which the stress is represented by a uniform tension p to some depth a. The tension can be thought of as resulting from thermal contraction.

For a long tension crack in an ideal elastic medium the rate of strain release energy with crack extension G (crack extension force), Young's modulus E, and Poisson's ratio ν, are related to the crack stress intensity factor K_I (Irwin, 1957; Hellan, 1984), thus

$$G = (\beta/E)\, K_I^{\,2} \tag{4-69}$$

where

$$\beta = \begin{cases} 1 & \text{for plane stress} \\ 1 - \nu^2 & \text{for plane strain} \end{cases}$$

For the step function and plane strain, equations 4-62 and 4-69 give

$$p \sqrt{b}\, [1 - (2/\pi) \cos^{-1} a/b] = [G\, E\, (1 - \nu^2)]^{1/2} \tag{4-70}$$

Solve for the crack extension force

$$G = \frac{b(1 - \nu^2)}{E} [p\, (1 - \frac{2}{\pi} \cos^{-1} \frac{a}{b})]^2 \tag{4-71}$$

which represents Lachenbruch's (1961) solution. Similarly, Hartranft and Sih (1973) derive the crack driving force as

$$G = \frac{b(1 - \nu^2)}{E} \{\frac{2}{\pi} \cos^{-1} \frac{a}{b} [1 + F(a/b)]\sigma\}^2 \tag{4-72}$$

In general, b in equation 4-71 will have two values. The larger value corresponds to the ultimate depth, the smaller value represents the critical crack depth b_c necessary for the onset of unstable propagation.

For a stable crack penetrating a semi-infinite solid with a constant homogenous initial stress, K_I will increase as the square root of crack depth. However, if the tensile stress decreases faster with depth x than $x^{1/2}$, K_I will decrease for a growing crack. Hence, under the present assumptions regarding stress, if K_I does not assume the critical value K_{IC} by the time the crack reaches depth a, it never will, and propagation will be stable and confined to the surficial layer $x <$ a. If the crack grows unstably to depth b_c in the surficial layer $x <$ a, it can generally be expected to propagate to some depth $b > a$ if a is not too large. It is likely that a thermal contraction-crack in frozen sand, formed by tension, will propagate unstably in response to surficial tension.

If the crack depth is small, it will be very sensitive to G_o, for "crack arresting" which is lower for more brittle and hence colder media. For the case $G_o = 0$, an upper limit to crack depth is given, as it represents an ideal medium in which no energy is consumed by the crack-extension process. Thus the crack continues to propagate until its crack-driving force falls below G_o. In general, G_o is expected to be less than the critical crack-driving force G_c needed for crack initiation.

4.2.4 Crack Growth Resistance Curve (R-Curve)

An R-curve is a continuous record of toughness development in terms of crack-extension resistance K_R plotted against crack extension in frozen soil as a crack is driven under a continuously increasing stress intensity factor K_I. Recall that K_R is a measure of the resistance of material to crack extension expressed in terms of the stress intensity factor, K_I.

Assuming that the frozen soil would remain predominantly elastic throughout the duration of a test and restricting our attention to a mode I failure and small-scale yield, the criterion of linear-elastic fracture mechanics can be written as

$$K_I = K_{IC} \tag{4-73}$$

where K_{IC} is stress fracture toughness. The value of K_{IC} is the value of K_R at the instability condition determined from the tangency between the R-curve and the applied K_I curve of the specimen Figure (4-10). The term K_{IC} is a function of load, sample geometry, and material properties. Equation 4-73 describes a necessary condition for the onset of crack propagation.

The fracture toughness K_{IC}, the R curve, and the critical length of the crack a_c, must be evaluated in order to obtain a complete picture of material behavior during crack propagation. ASTM standards E 616-82, E 399-83, and E 561-86 provide a standard method to evaluate the individual parameter for fracture mechanics of materials. These ASTM standards and information presented by Paris and Sih (1964) provide a procedure which appears to be suitable for determination of the fracture toughness of frozen soil. The R-curve can then be determined by drawing fracture toughness K_{IC} versus the change in crack length Δa.

When used for metals this procedure for determination of K_{IC} can be summarized as described below. Some modifications in the procedure may be required for frozen soil.

1. Run a uniaxial tensile test on the material at a strain rate close to 0.02 inch/min and determine the 0.2% offset yield strength σ_{ys} and the modulus of Elasticity E.
2. Based on the ratio σ_{ys}/E, select a crack length from the list given in Table (4-6), taking into consideration that our material is frozen Ottawa sand. Note that Table (4-6) is recommended for metals.
3. Select a crack length and run a fatigue test using stresses less than 1/2 the yield strength σ_y so as to give a sharp notch.
4. Run a uniaxial tensile test on a sample with a sharp notch. The load corresponding to a 2 % apparent increment of crack extension is established by a specified deviation from the linear portion of the record.
5. The K_{IC} value is calculated from this load by an equation that has been established on the basis of an elastic stress analysis of the specimen.

Superposition of the elastic solution for K_I on the R-curve (Figure 4-10) will give a value for the critical crack length at which the crack will form unstably.

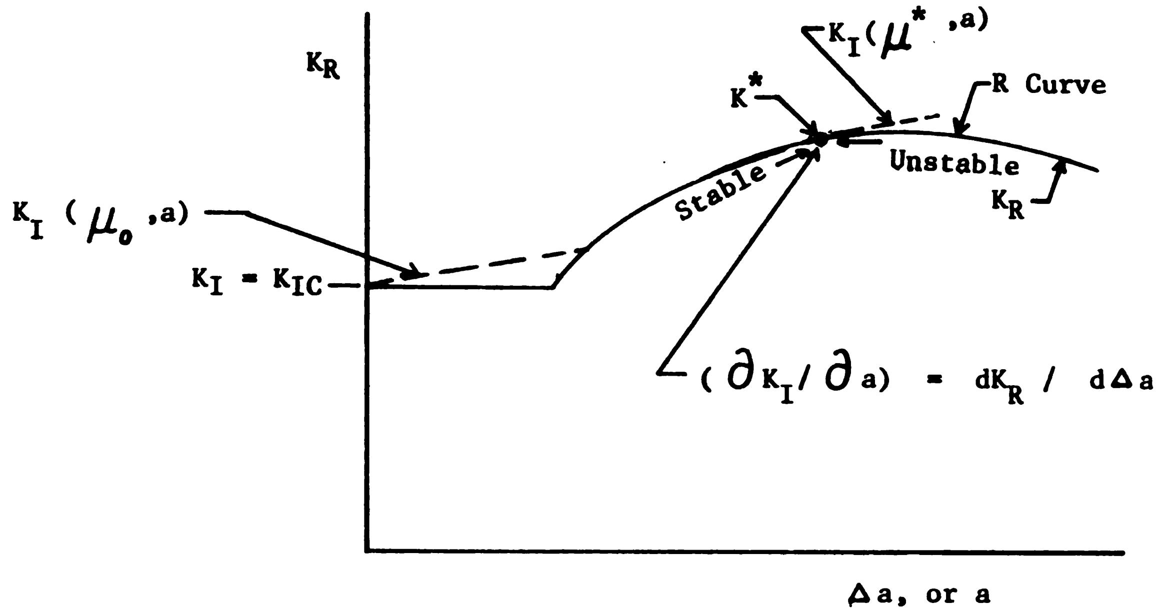

Figure 4-10: Crack Growth Resistance Curve (R-Curve).

Table 4-6: Minimum Recommended Crack Length (ASTM E 399-82).

σ_{ys}/E	Minimum Recommended Crack Length (in)	(mm)
0.0050 to 0.0057	3	75
0.0057 to 0.0062	2.5	63
0.0062 to 0.0065	2	50
0.0065 to 0.0068	1.75	44
0.0068 to 0.0071	1.5	38
0.0071 to 0.0075	1.25	32
0.0075 to 0.0080	1	25
0.0080 to 0.0085	0.75	20
0.0085 to 0.0100	0.5	12.5
0.0100 or greater	0.25	6.5

The elastic solution for K_I is a function of specimen geometry and the applied load. Paris and Sih (1964) introduce an elastic solution for a round bar subjected to tension, similar to the frozen sand tensile sample described in section (3.3). The stress intensity factor K_I for the specimen shown in Figure (4-11), is

$$K_I = \sigma_{net} (\pi/D)^{1/2} F(d/D) \tag{4-74}$$

where σ_{net} is the tensile stress on the sample, D is the outer diameter, d is the notched-section diameter, and F(d/D) is a function of the diameter ratio given in Table (4-7). One can regard equation (4-74) as

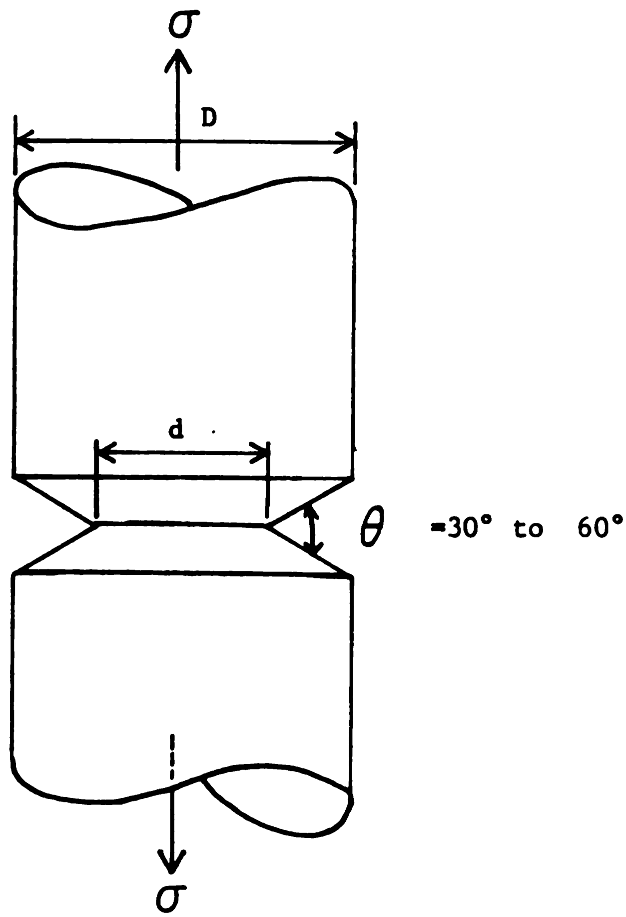

Figure 4-11: A Circumferentially Cracked Round Bar Subjected to Tension, (Paris and Sih, 1964).

$$K_I = f\,(\sigma_i \sqrt{\pi a}) \qquad i = 1, \ldots\ldots, n \qquad (4\text{-}75)$$

where a is crack length. If σ is variable, say (σ_1, σ_2, σ_3, ... ,σ_n), then one can generate a series of curves from equation (4-75) in which K_I and a_e (effective crack length) are variable for a fixed value of σ_i. As shown in Figure (4-12), the σ_i curve, which is tangent to the R-curve, will give the critical crack length a_c.

Table 4-7: Stress-Intensity Factor Coefficients for Notched Round Bars (Paris and Sih, 1964).

d/D	F(d/D)	d/D	F(d/D)
0	0	0.70	0.240
0.1	0.111	0.75	0.237
0.2	0.155	0.80	0.233
0.3	0.185	0.85	0.225
0.4	0.209	0.90	0.205
0.5	0.227	0.95	0.162
0.6	0.238	0.97	0.130
0.65	0.240	1.00	0

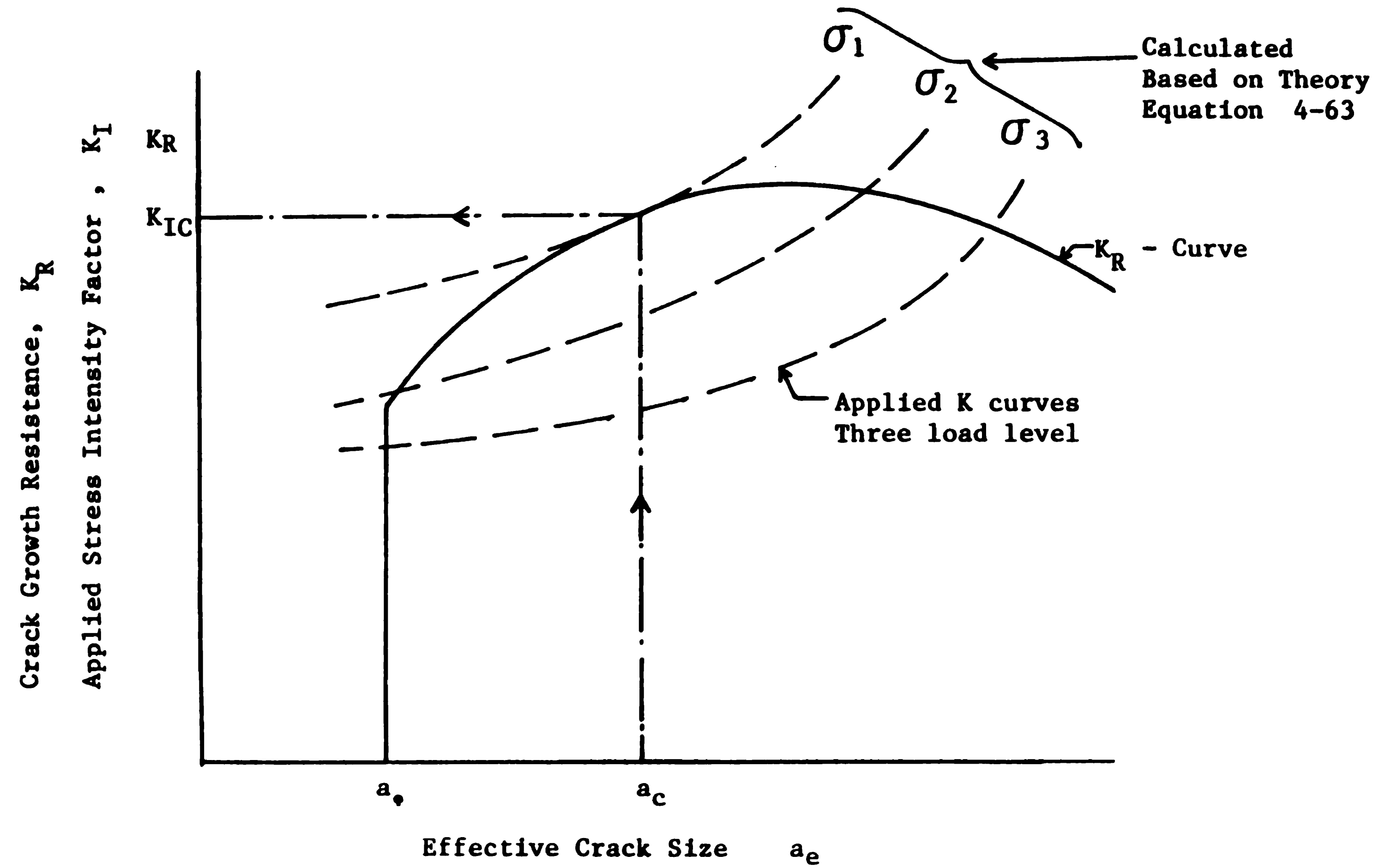

Figure 4-12: Schematic Representation of the R-Curve and Applied K Curve Used for Instability Prediction. Values For K_{IC}, σ_i, and a_c Correspond to an Initial Crack Size a_0.

4.2.5 Experimental Method to Determine the R-Curve

This method involves testing of notched specimens in tension that have been precracked in fatigue. Load versus displacement across the notch at the specimen edge is recorded autographically. The load, corresponding to a 2% apparent increment of crack extension, is established by a specified deviation from the linear portion of the record. The K_I value calculated from this load by equation 4-74 represents the fracture toughness K_{IC}. The validity of this determination of K_{IC} depends upon establishment of a sharp-crack condition at the tip of the fatigue crack in a specimen of adequate size. A sharp-crack under severe tensile constraint, will have a small plastic region at the crack tip compared to the crack size. Specimen size required for testing varies as the square of the ratio of toughness to yield strength of the material. More details are given in ASTM standard E 561-86.

As shown in Table (4-6), and based on earlier comments on dependence of fracture toughness on specimen geometry, information is needed to establish adequate size for frozen soil specimens. Note that Table (4-6) gives values for metal specimens. Recall that frozen soil has a lower yield stress and modulus of elasticity than metal. Highly computerized and controllable machines with an adequate load cell and standard fracture mechanics crack opening displacement transducers, such as the Material Test System (MTS) Units or Instron Units, are recommended for use in measurement of K_{IC}. This equipment was not available to this project and measurement of k_{IC} remains for future research. At this stage, a comparison of theoretical and experimental fracture mechanics for frozen soil is not available.

CHAPTER V

FIELD EXAMPLE

5.1 <u>Field Conditions -- Fargo, North Dakota</u>

Results of the last three chapters and available theories may now be applied to a numerical example. Among three different locations considered, temperature conditions for Fargo, North Dakota, was selected for the field example. No field sites in North Dakota were examined as to where cracking occurred. Thermal cracking has been observed in Michigan for less severe temperature conditions. The data selected may not represent a typical season, but thermal contraction cracking is predicted for the soil conditions assumed, as will be shown later in the numerical example.

5.1.1 Soil Profile Analyzed

The soil profile analyzed is frozen sand. "Frozen sand" is a term applied to those sands in which below freezing temperatures exist and in which at least a part of the water contained in the sand pores is frozen. The sand particle size ranged from 3.36 mm (0.132 inch) to 0.074 mm (0.0029 inch), which consists mainly of sub-angular quartz particles with specific gravity G_s equal 2.65. Unsaturated frozen sand is a complex four phase system consisting of four interrelated components: solid mineral particles and ice, liquid water, and air or gas. The ice matrix serves to cement the soil particles into a much more coherent mass (Tsytovich, 1975) which can resist large tensile stresses.

The physico-mechanical processes present in freezing sand produce properties and a structure which are quite different from those of unfrozen soils. A partial or almost complete change of water into ice is accompanied by the appearance of ice cementation bonds between the sand mineral particles, and by sharp changes in the physical and mechanical properties of the sand. With quartz as the primary component of sand, essentially all moisture will change to ice in frozen sand. During cooling of frozen sand, especially in zones of intensive phase change of water into ice, there occurs continuously a redistribution of moisture and water movement away from the plane of cooling as the water expands about 9 percent on freezing.

Changes in the frozen sand temperatures control the degree of ice cementation of particles. However, at any temperature below freezing, there always remain small amounts of unfrozen water (Tsytovich, 1975). Since the cementation bond in frozen sand is a function of the ice content, it is necessary to determine the amount of unfrozen water at any temperature. Methods for estimating unfrozen water contents were reviewed in section 2.2.1.

Below the water table the sand is completely or almost completely saturated. Above the water table the degree of saturation depends primarily on the grain size characteristics of the soil as shown in Figure (5-1). A typical degree of saturation for sand is between 30% to 35%. This will lead to a water content of 5.7% to 6.7% for sand with a specific gravity G_s of 2.65, an average void ratio e of 0.51, and effective grain size D_{10} of 0.2 mm to 0.3 mm, as shown in Figure (5-1).

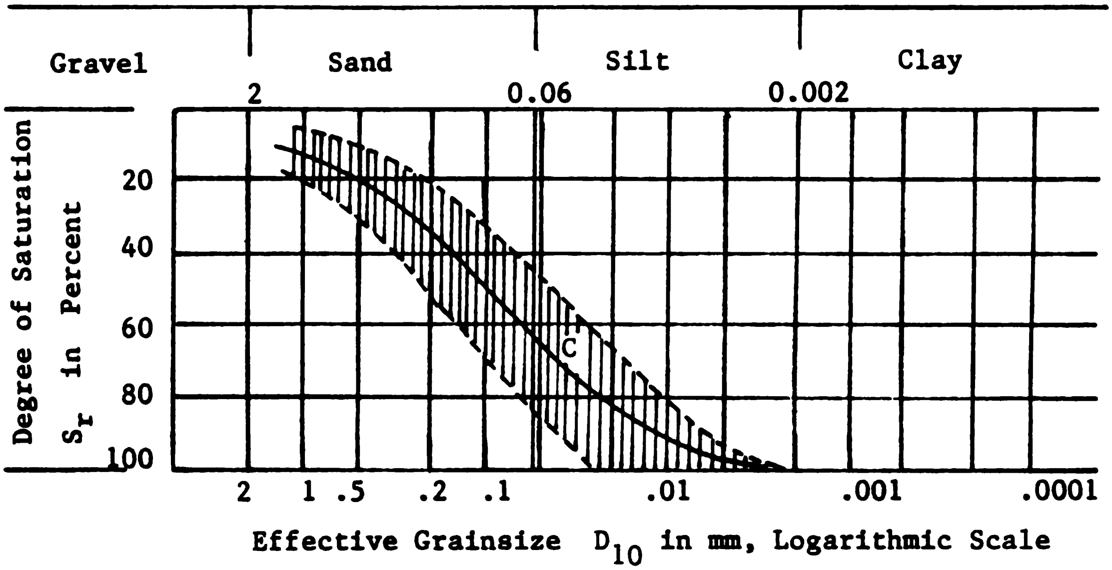

Figure 5-1: **Approximate Relationship between Effective Grain Size and Degree of Saturation in the Zone of Soil Moisture in Temperature Zones with Moderate Rainfall (Terzaghi, 1952).**

5.1.2 Surface and Ground temperatures.

"Temperatures at the air-ground interface exhibit random daily and yearly variations due to the partially independent fluctuation of climatological factors influencing these temperatures" (Aldrich and Paynter, 1953). For numerical computations it is convenient to assume a step change in surface temperature, and/or a sinusoidal change in surface temperature.

The step change in temperature approximates a sudden change in air (surface) temperature and can be used for calculation of the change in temperature of the soil mass which is assumed to be initially at a constant temperature. To avoid the nonlinearty problem due to latent heat, assume that during the period of interest the depth of frost penetration has a very limited fluctuation. It is convenient to describe the soil relative to two zones: frozen and unfrozen. For each surface temperature the frost depth represents the lower boundary for the frozen soil.

Now consider the semi-infinite soil mass as show in Figure (5-2), maintained at some initial uniform temperature T_o. The surface temperature is suddenly lowered and maintained at a temperature T_s. Now assume an expression for temperature distribution as a function of time. The one-dimensional differential equation for temperature distribution T(x, t) is

$$\frac{\partial^2 T}{\partial x^2} = \frac{1}{\alpha}\frac{\partial T}{\partial t} \qquad (5\text{-}1)$$

where symbols are defined after equation 5-2.

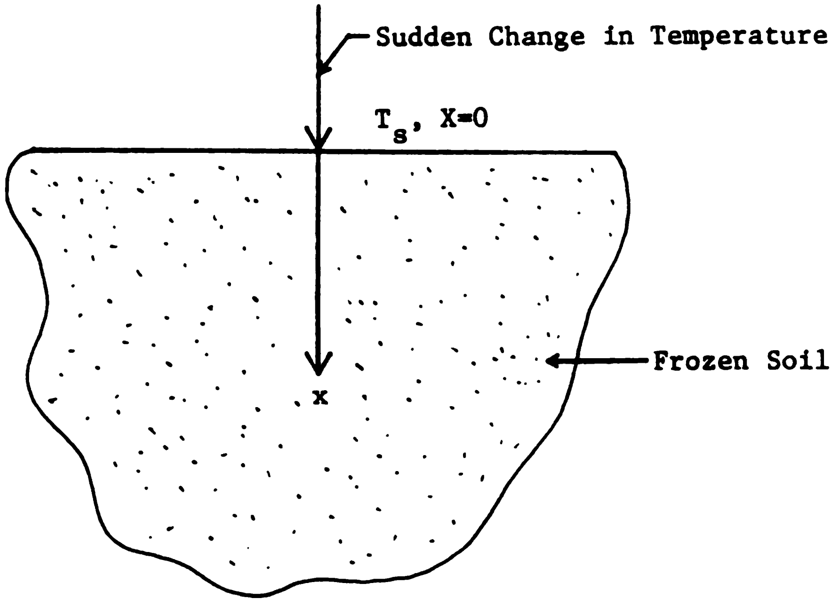

Figure 5-2: Transient Heat Flow in a Semi-Infinite Frozen Soil.

The boundary and initial conditions include

$$T(x, 0) = T_o, \text{ and } T(o, t) = T_s \text{ for } t > 0$$

Equation 5-1 has been solved by Arpaci (1966) using the Laplace transform technique with the result

$$\frac{T(x, t) - T_s}{T_o - T_s} = \operatorname{erf} \frac{x}{2\sqrt{\alpha t}} \tag{5-2}$$

where $T(x, t)$ is the ground temperature at depth x and time t, T_o is the initial uniform ground temperature in degrees Fahrenheit, T_s is the applied step surface temperature in degrees Fahrenheit, α is the soil mass coefficient of thermal diffusivity in ft^2/day,

$$\alpha = \begin{cases} \alpha_f \text{ , } & x \leq \text{ frost depth} \\ \alpha_{av} \text{ , } & x > \text{ frost depth} \end{cases} \tag{5-3}$$

and t is time after application of the step change in surface temperature in days, x is depth below surface in ft, and erf is the error function. The Gauss error function in equation (5-2) is defined as

$$\operatorname{erf} \frac{x}{2\sqrt{\alpha t}} = \frac{2}{\sqrt{\pi}} \int_0^{\frac{x}{2\sqrt{\alpha t}}} e^{-\eta^2} \, d\eta \tag{5-4}$$

where η is a dummy variable, and the integral is a function of its upper limit. It can be shown that

$$\int_0^{\infty} \sigma^{-\beta^2} \, d\beta = \frac{\sqrt{\pi}}{2} \tag{5-5}$$

and thus

$$\text{erf}\ \infty = \frac{2}{\sqrt{\pi}} \int_0^{\infty} \sigma^{-\beta^2}\, d\beta = \frac{2}{\sqrt{\pi}} \cdot \frac{\sqrt{\pi}}{2} = 1$$

The error function can be approximated as

$$\text{erf}\ x = \frac{2}{\sqrt{\pi}} \sum_{n=0}^{\infty} \frac{(-1)^n\, x^{2n+1}}{(2n+1)\, n!} = \frac{2}{\sqrt{\pi}} \left(x - \frac{x^3}{3} + \frac{x^5}{10} + \ldots\right) \qquad (5\text{-}6)$$

Thus if x is small

$$\text{erf}\ x \simeq (2/\sqrt{\pi})\ x \qquad (5\text{-}7)$$

To find the ground temperature in a frozen sand surface layer which contains little or no unfrozen water, equation 5-2 plus a geothermal gradient term, was utilized.

$$T(x,\ t) = T_s + (T_0 - T_s)\ \text{erf}\ (X/2\sqrt{\alpha t}) + GX \qquad (5\text{-}8)$$

where G is the average geothermal gradient = 1.8 °C/100 m was used. A computer program was written to compute the argument of the error function. The results are in tabulated form where the argument of the error function was a function of temperature, depth, and time.

Convenient access to air temperature records for Fargo, North Dakota; Madison, Wisconsin; and Lansing, Michigan, provided information on dates with rapidly decreasing temperatures. Air temperature data for three hour intervals, Max-Min temperatures, and thermal gradients (dT/dt) are summarized in Table (5-1). The Fargo, North Dakota, location was selected for the example based on its larger cooling rate. Ground temperatures were computed, using equation 5-8, to a depth of 90 cm and are summarized in Table (5-2), and Figure (5-3). The following example illustrates calculation for the ground temperatures.

Example 1.

To compute the ground temperature at a depth of 24 cm at hour 18 (Figure 5-3), the following steps were followed: Equation 2-30 gives the unfrozen water content $w_u = \alpha\, \theta^{\beta}$ where $\theta = 24.56$ °C.
Obtain α from equation 2-31, thus $\ln \alpha = 0.5519 \ln S + 0.2618$ where $S = 0.001\ m^3/g$ for sand and $\alpha = \mathrm{Exp}\,[0.5519 \ln 0.001 + 0.2618] = 0.0287$.
Compute β using equation 2-32, thus $\ln(-\beta) = -0.2640 \ln S + 0.3711$ and $\beta = -\mathrm{Exp}\,[-0.2640 \ln 0.001 + 0.3711] = -8.977$. Now compute the unfrozen water content $w_u = 0.0287\ (24.56)^{-8.977} \approx 0.0$ and the ratio
$W_u = w_u/w \approx 0.0$
From equation 2-43, the heat capacity for partially frozen soil will be

$$C_{vf} = \gamma_d\, [C_{ms} + C_{mi}\ (1 + W_u)\ w/100]$$

Use equation 2-44 to compute the mass heat capacity for the solids, thus

$$C_{ms} = C_p = 5.2 \times 10^{-4}\ T + 0.0247 \quad \text{where}$$

$$T = 273 + T_s = 273 - 22.7 = 250.3\ °K$$

and $$C_{ms} = (5.2 \times 10^{-4} \times 250.3 + .0247) \times \frac{67}{160 \times 10^{-4} \times 1000}$$

$$= 0.648\ J/g\ °K$$

Recall that $1\ cal/cm^3\ °C = \dfrac{67}{160 \times 10^{-4}}\ KJ/m^3\ °C$

From Table (2-5) obtain the equation for C_{mi}, thus
$C_{mi} = [1.76 \times 10^{-3}\ T + .0228] \times 4.1868$ where $T = 273 + T_s = 250.3$ °K and $C_{mi} = 1.94\ J/g\ °K$. Now compute the volumetric heat capacity for the sand,

$C_{vf} = 1693.18 \times 10^3\ [0.648 + (1.939)\ 21.13/100]\ 1/1000 = 1790.8\ KJ/m^3\ °C$

Using equations 2-36 and 2-37 compute the unfrozen and frozen thermal conductivities

$$k_u = 0.1442\ [0.7 \log \omega + 0.4]\ 10^{0.6243\gamma_d}$$

$$= 0.1442\ [0.7 \log 21.13 + 0.4]\ 10^{0.6243 \times 1.69318} = 2.182\ W/m\ °K$$

and

$$k_f = 0.01096\ (10)^{0.8116\gamma_d} + 0.00461\ (10)^{0.9115\gamma_d}\ \omega$$

$$= 0.01096 \times 10^{0.8116 \times 1.69318} + 0.00461 \times 10^{0.9115 \times 1.69318} \times 21.13$$

$$= 3.657\ W/m\ °K$$

For the frost depth computation obtain the average

$K = (2.182 + 3.657)/2 = 2.9195\ W/m\ °K$

Using equation 2-46 compute the soil thermal diffusivity

$$\alpha = \frac{K}{C} = \frac{2.9195}{1790.8 \times 1000} = 1.630 \times 10^{-6}\ m^2/sec$$

Note that 1 Watt (W) = 1 Joule (J)/sec (s). Using equation 5-8 compute the soil temperature. $T(x, t) = T_s + (T_o - T_s)\ \mathrm{erf}\ (x/2\sqrt{\alpha t}) + Gx$

For a depth of 24 cm and the 18th hour compute the soil temperature

$$T(20, 3) = -22.7$$
$$+ (-24.56 + 22.7)\ \mathrm{erf}\ (20/100/\ 2\sqrt{1.63 \times 10^{-6} \times 3 \times 3600})$$
$$+ 0.018 \times 20/100$$
$$= -22.7 - 1.86\ \mathrm{erf}\ (0.7536) + 0.0036 = -24.18\ °C$$

This temperature is shown in Table (5-2) for the 24 cm depth and the 18th hour. Ground temperatures at other soil depths are summarized in Table (5—2) and Figure (5-3).

Table 5-1: Air Temperature Data at 3-hr Intervals for Selected Dates at 3 Locations.

Fargo, ND 2-3 Feb. 1974			Madison, WI 10-11 Jan. 1979			Lansing, MI 10-11 Jan. 1984		
Time (hr)	*Temp. (°C)	dT/dt (°C/hr)	Time (hr)	*Temp. (°C)	dT/dt (°C/hr)	Time (hr)	*Temp. (°C)	dT/dt (°C/hr)
09	-14.4		12	-17.8		01	-12.8	
		0			+3.7			-0.187
12	-14.4		15	-16.7		04	-13.3	
		-0.187			-1.296			-0.926
15	-15.0		18	-20.6		07	-16.1	
		-0.259			-0.166			+1.853
18	-22.8		21	-25.6		10	-10.6	
		-2.223			-1.110			+0.556
21	-29.4		00	-28.9		13	- 8.9	
		-3.7			-0.373			-0.373
00	-30.6		03	-30.0		16	-10.0	
		-0.556			-0.553			-3.330
03	-32.2		06	-31.7		19	-20.0	
		-0.556			-0.740			-1.480
06	-30.6		09	-29.4		22	-24.4	
		-0.370			+3.746			-1.110
09	-31.7		12	-18.3		01	-27.8	
		+1.480			+0.370			+1.480
12	-27.2		15	-17.2		04	-23.3	
Min	-32.2			-31.7			-27.8	
Max	-14.4			-16.7			- 8.9	
Avg#	-24.56	-1.18		-24.3	-1.00		-16.0	-1.57

* Air temperature data from U.S. Dept. of Commerce, National Oceanic and Atmospheric Administration, Environmental Data Service

Average values are for the 24-hr period.

Table 5-2: Computed Ground Temperatures Based on Observed Air Temperatures, Fargo, ND

Depth (cm)	Time (hr) 09	12	15	18	21	00	03
	Ground Temperatures, °C						
0	-14.44	-14.44	-15.00	-22.70	-29.44	-30.55	-32.22
4	-16.05	-16.05	-16.57	-22.99	-28.62	-29.54	-30.94
8	-17.76	-17.76	-18.14	-23.31	-27.83	-28.58	-29.70
16	-20.70	-20.70	-20.92	-23.83	-26.49	-26.93	-27.59
20	-21.32	-21.32	-21.88	-24.03	-25.97	-26.29	-26.78
24	-22.60	-22.60	-22.71	-24.18	-25.55	-25.77	-26.11
30	-23.53	-23.53	-24.11	-24.36	-25.12	-25.24	-25.47
50	-24.48	-24.48	-24.49	-24.54	-24.60	-24.61	-24.62
70	-24.54	-24.54	-24.55	-24.55	-24.56	-24.56	-24.56
90	-24.55	-24.55	-24.55	-24.55	-24.56	-24.56	-24.56

Notes:

1. Sand with γ_d = 1693.18 kg/m^3, w = 21.13 %, and S = 100 %.
2. Surface temperatures for 2-3 Feb. 1974, Fargo, ND.
3. $T(x, t) = T_s + (T_o - T_s) \operatorname{erf}(x/2\sqrt{\alpha t}) + Gx$
4. T_o = -24.56 °C, G = 0.0018 °C/m

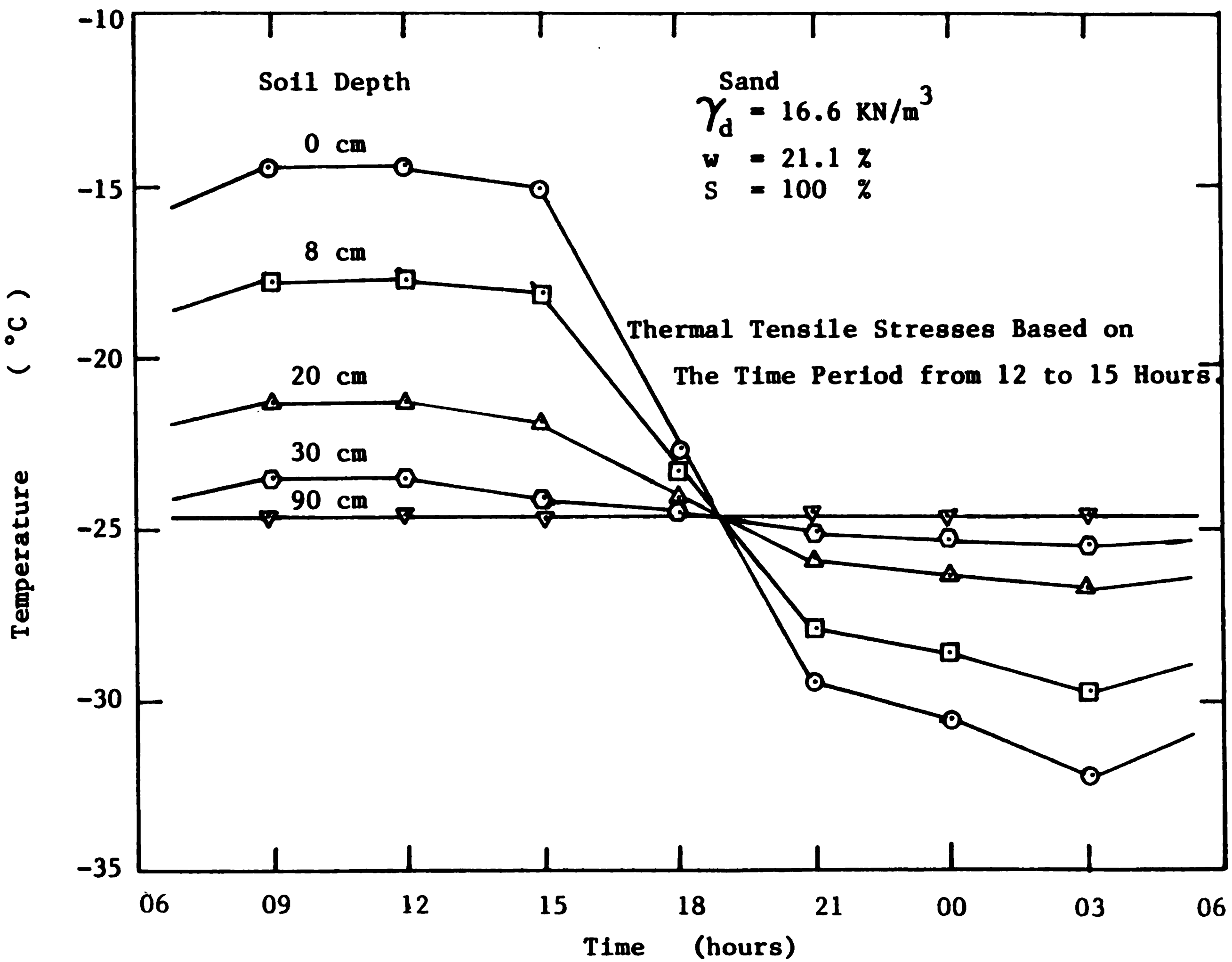

Figure 5-3: Computed Ground Temperature in Sand for Fargo, North Dakota, on 2-3 February, 1974.

5.1.3 Frost Depth Penetration

Seasonal temperature changes in the Northern states, Alaska and Canada, include a period were cold winter temperatures freeze surface soils to a depth dependent on the severity of the freezing season. The surface freezing index provides a measure of this severity and is commonly taken as the cumulative departure from a given reference, usually the freezing point of water (0 °C). The depth of freeze in soils depends upon the soil thermal properties, the surface temperature, and the initial soil temperature at the start of the freezing season. For convenience in calculation, the average initial ground temperature is generally assumed equal to the mean annual air temperature for the site.

The depth of ground freezing is given by the modified Berggren equation (Aldrich and Paynter, 1953). Assumptions include the following: (1) the soil mass is considered to be homogeneous and one dimensional, (2) the initial site surface temperature in the soil mass is constant at a value $V_o = (T_m - T_f)$ above freezing, (3) the change in surface temperature during the freezing period can be represented by a step change equal to V_s, (4) latent heat of the soil moisture is taken into consideration as a heat source (or sink) at the moving freezing interface, and (5) assumptions 1 to 4 take into account both volumetric heat capacity and the latent heat including changes in thermal properties which occur during freezing of the soil moisture.

The final form of the modified Berggren formula (Aldrich, and Paynter, 1953) is

$$x = \lambda \sqrt{7200\ knF/L} \qquad (5\text{-}9)$$

where x is the depth of freezing in m, k is the thermal conductivity of soil in J/s m°C, L is the volumetric latent heat of fusion in J/m^3, n is a dimensionless conversion factor for air index to ground surface index (see Table 5-3), F is the air-freezing index in degree-days, and λ is a coefficient which takes into consideration the effect of temperature changes in the soil mass. An average distribution of air-freezing indices are given in Figure (5-4) for the U.S.A. Common values for regional depths of frost penetration are given in Figure (5-5) for the U.S.A.

The λ coefficient is a function of the freezing index, mean annual temperature of site, and the soil thermal properties. To obtain λ from Figure (5-6), information is required on the thermal ratio α and fusion parameter μ.

$$\alpha = V_o/V_s = T_m/T_s \qquad (5\text{-}10)$$

$$\mu = V_s \times (C/L) = T_s\ (C/L) \qquad (5\text{-}11)$$

where V_o is the mean annual site temperature in degrees Celsius, V_s is the surface freezing index (nF) divided by the length of freezing season = nF/t, C is the average volumetric heat capacity of the soil in J/m^3 °C, t is time in hours, and L is volumetric latent heat in J/m^3.

Example 2.

To determine the frost depth at Fargo, ND, use the modified Berggren formula (equation 5-9). Thus $x = \lambda \sqrt{7200\ kn\ F/L}$ where

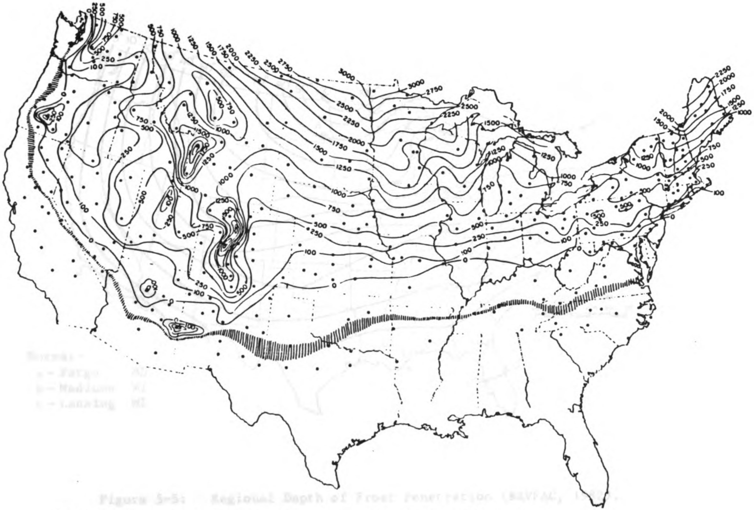

Figure 5-4: Distribution of Mean Freezing Index Values in Continental United States (Department of the Army, Corps of Engineers, 1958)

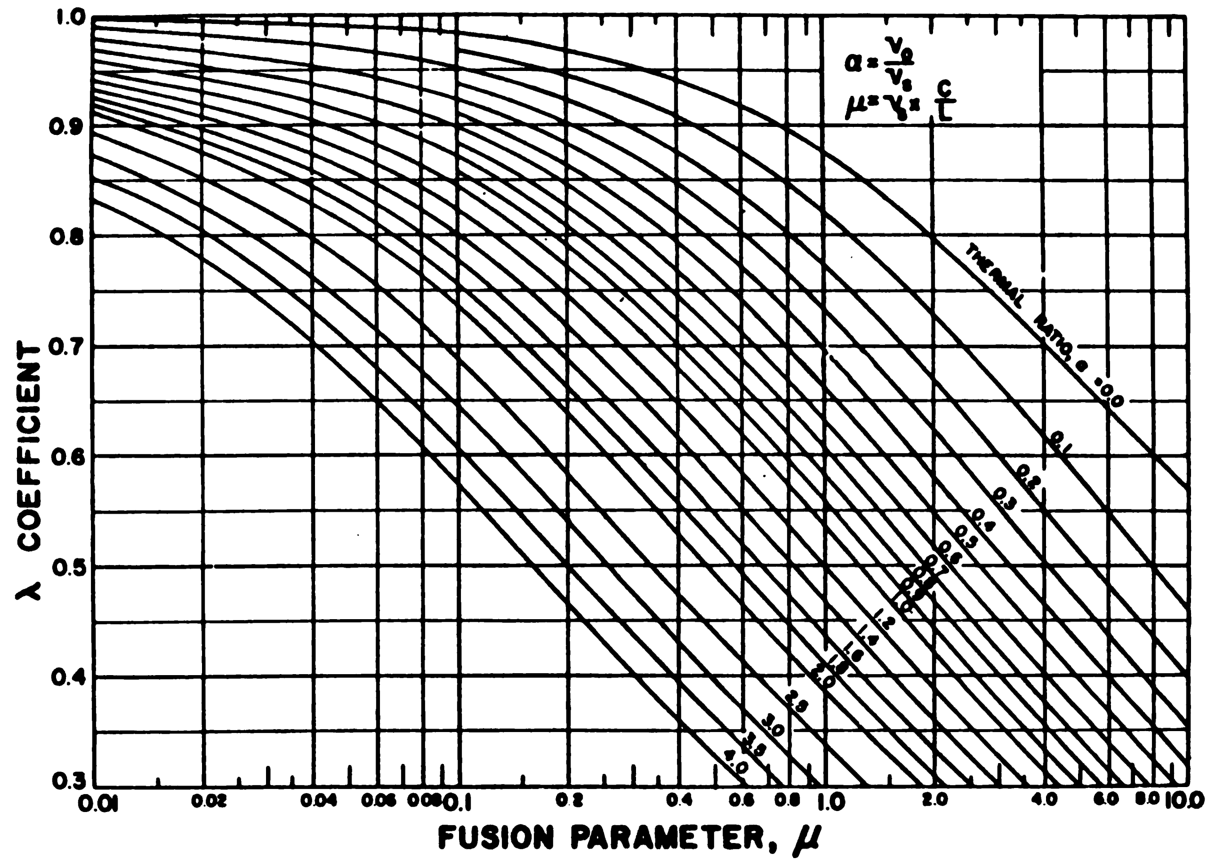

Figure 5-6: λ Coefficient in the Modified Berggren Formula (Department of the Army and the Air Force, 1966)

Table 5-3: n Factor Data, General Surfaces (Lunardini, 1981).

Surface Type	Freeze n	Freeze I_a +	Location
Sprue trees, brush moss over peat soil	.29	5042	Fairbanks, Alaska
Brush and tree cleared, moss in place, peat soil	.25	5042	Fairbanks, Alaska
Vegetation and 16 in. of soil stripped clean	.33	5042	Fairbanks, Alaska
Turf	.5	—	Alaska, and
Greenland			
Snow	1.0	—	Alaska, and
Greenland			
Sand and gravel	.9	—	Alaska, and
Greenland			
Gravel	.6	5042	Fairbanks, Alaska
Pavement without snow	.9	—	Fairbanks, Alaska
Sandy soil, with snow	.49	1908	Lakselv
	.02	2034	Os, Norway
	.53	342	Amli, 1974,
Norway			
	1.39	234	Amli, 1975,
Norway			

+ Ia = nF = freezing index for the ground surface.

n = 0.9 (from Table 5-3), k_f = 3.657 W/m°k (from Example 1), k_u = 2.182 W/m°k (from Example 1), and k_{av} = 2.915 W/m°k. Compute the freezing index based on local climatological data given in Table (5-4). From Table (5-4) note that the length of the winter season = 30 + 31 + 31 + 28 + 31 = 151 days. Now compute the freezing index

$FI = -15 \times 31 - 12.66 \times 28 - 4.44 \times 31 - 2.61 \times 30 - 10.66 \times 31$

$= -1365.88$ °C day. In the same manner compute the thaw index

TI = 3021.18 °C days. Using equation 2-38 compute the latent heat for the soil, thus

$L_f = \rho_d\ \omega\ L' = 1693.18\ (21.13/100)\ 333.7 = 1.193 \times 10^5\ kJ/m^3$

From example 1, obtain the volumetric heat capacity

$C_{vf} = 1790.8\ kJ/m^3\ °C$.

Using the freezing and thaw indexes compute the mean annual temperature

$T_m = (FI + TI)/365 = 4.535\ °C = V_o$. The equivalent step temperature

$V_s = n\ FI/t = 0.9\ (1365.88)/151 = 8.141\ °C$.

The thermal ratio $\alpha = V_O/V_S = 0.5570$ and the fusion parameter

$\mu = V_s \times C/L = 8.141 \times 1790.8/(1.193 \times 10^5) = 0.122$.

From Figure (5-6) read $\lambda = 0.9$ and compute the frost depth

$$X = 0.9 \sqrt{7200 \times 2.915 \times 0.9 \times 1365.88 \times 24/(1.193 \times 10^8)} = 2.05\ m,$$

which is in close agreement with the 80 inch depth shown in Figure (5-5). It is obvious that the depth of the frost for sand with 30% moisture saturation at Fargo, ND, will be the highest among the three locations, shown in Table (5-5).

Table 5-4: Average Monthly Temperature over 54 Years (1900-1954), in Fargo, N.D.

Month	Mean + Temperature (° F)	Days of Month
Jan.	-15.00	31
Feb.	-12.00	28
March	- 4.44	31
April	5.66	30
May	12.55	31
June	18.05	30
July	20.94	31
Aug.	19.77	31
Sep.	14.5	30
Oct.	7.22	31
Nov.	-2.61	30
Dec.	-10.66	31

+ Source: Local Climatological Data, U.S. Department of Commerce, National Oceanic and Atmospheric Administration, Environmental Data Service, National Climatic Center. Ashville, NC.

Table 5-5: Maximum Frost Depths for the Three Locations during the Year for Sand, Silt, and Clay Soils.

Location	Frost depth, cm		
	Sand γ_d = 16.6 kN/m^3 w = 21.13 % S = 100 %	Silt γ_d = 14.0 kN/m^3 w = 26.2 % S = 80.0 %	Clay γ_d = 16.0 kN/m^3 w = 24.2 % S = 100 %
Fargo, ND 1973-74	205	155	196
Madison, WI 1978-79	157	110	133
Lansing, MI 1983-84	116	83	100

Notes:

γ_d = soil dry density (kN/m^3),

w = water content (%, dry weight basis), and

S = degree of soil saturation (%), average from Figure (5-1).

The ground surface was assumed to have no snow or turf cover.

+ 1 kN/m^3 = 101.99 kg/m^3

5.2 Numerical Results

5.2.1 Thermal Stresses and Soil Strength

Contraction cracking is most likely to occur when surface temperatures are falling rapidly. A period of rapid cooling occurs in late fall, and others occur during winter storms, for example the period of February 2-3 in Figure (5-3). Although cooling rates are not appreciably greater during mid-winter fluctuations, thermal stresses are likely to be on the order of 100 percent greater in mid-winter when the ground is more solidly frozen.

For elastic behavior the thermal stress can be computed from

$$\tau^{*}(x) = - \frac{E}{1 - \nu} \alpha \Delta T \qquad (5\text{-}12)$$

where E is Young's modulus, ν is Poisson's ratio, α is the coefficient of thermal contraction, and ΔT represents changes in temperature. Values of E, ν and tensile strength for frozen Ottawa sand were selected from experimental results reported by Bragg (1980). The coefficient of thermal contraction is based on data reported in Chapter III, Figure (5-7), (5-8), and (5-9). These values permit calculation of thermal stresses at different soil depths as summarized in Table (5-6), and Figure (5-10).

Example 3.

The thermal stress and strength at a depth of 20 cm and hour 21 are computed as follows: At hour 21 the frozen soil temperature was -25.97 °C at a depth = 20 cm (Table 5-2). ΔT = -25.97 - 0 = -25.97 °C

From Figure (5-7) and (5-8) the experimental values of E and ν are,

$\nu = -0.08625$ (Average value) and

$E = [0.55 - 0.424\ T] \times 10^5 = [0.55 - 0.424\ (-25.97)] \times 10^5$

$= 11.561 \times 10^5$ psi

From Figure (3-4) obtain $\alpha = 25.80 \times 10^{-6}\ ^\circ C^{-1}$ at $T = -25.97\ ^\circ C$

Using Equation (5-12) compute the thermal tensile stress

$$\tau^*(x) = -\frac{E}{1 - \nu}\ \alpha\ \Delta T$$

$$= -\frac{11.561 \times 10^5}{1 - (-0.08625)}\ (25.8 \times 10^{-6})(-25.97) = 713.11 \text{ psi}$$

From Figure (5-9) read the tensile strength $\tau(x) = 750$ psi
From Figure (3-38) estimate the residual stress to be about 175 psi based on the -15 °C temperature prior to the winter storm. Therefore, the total tensile stress will be about $(713.11 + 175) \approx 888.11$ psi which is greater than 750 psi. Based on these calculations tensile failure will occur for frozen saturated sand. Partially saturated sand would have lower tensile strengths and would be much more susceptible to tensile failure.

5.2.2 Crack Depth Prediction

Temperature conditions recorded for 2-3 February 1974 at Fargo, North Dakota, have been selected for use in prediction of thermal contraction crack depth at a site with deep cohesionless soil (sand). No snow cover and a bare ground surface will be assumed. Air

Table 5-6: Comparison between Thermal Stresses, $\tau^*_{(x)}$, and Tensile Strengths, at the Respective Depths, for Temperatures at Fargo, N.D. on Feb. 2-3, 1974.

Depth (cm)	ΔT (deg C)	E x 10^5 (psi)	ν	α x 10^{-6} (deg C)$^{-1}$	$\tau^*(x)$ Stress (psi)	$\tau(x)$ Strength (psi)	remarks
0	-29.44	13.03	-.086	25.11	886	821	
4	-28.62	12.69	-.086	25.27	844	807	
8	-27.83	12.34	-.086	25.43	804	790	$\tau(x) < \tau^*(x) + \tau_R$
16	-26.49	11.78	-.086	25.70	738	780	
20	-25.97	11.56	-.086	25.80	713	750	Therefore Tensile
24	-25.55	11.38	-.086	25.89	693	740	failure occurs
30	-25.12	11.20	-.086	26.00	673	735	
50	-24.60	10.98	-.086	26.12	649	720	
70	-24.56	10.96	-.086	26.12	648	718	
90	-24.56	10.96	-.086	26.12	648	718	

Notes:

E = Young's modulus extrapolated from data (Bragg, 1980) for warmer temperatures and a strain rate of 1 x 10^{-4} sec^{-1}.

T = computed temperatures in the frozen sand at the given depth on Feb. 2-3, 1979, Fargo, N.D.

$\tau(x)$ = tensile strengths for saturated frozen sand extrapolated from data (Bragg, 1980) for warmer temperatures and a strain rate of 1 x 10^{-4} sec^{-1}.

α = linear thermal contraction coefficients, from Figure (3-4).

ν = Poisson's ratio (data from Bragg, 1980).

$\tau^*(x) = -\dfrac{E}{1-\nu}\,\alpha\,\Delta T$ = thermal stress assuming elastic soil behavior.

τ_R = residual stress ≃ 165 psi, (based on Figure (3-41) and T = -15°C.

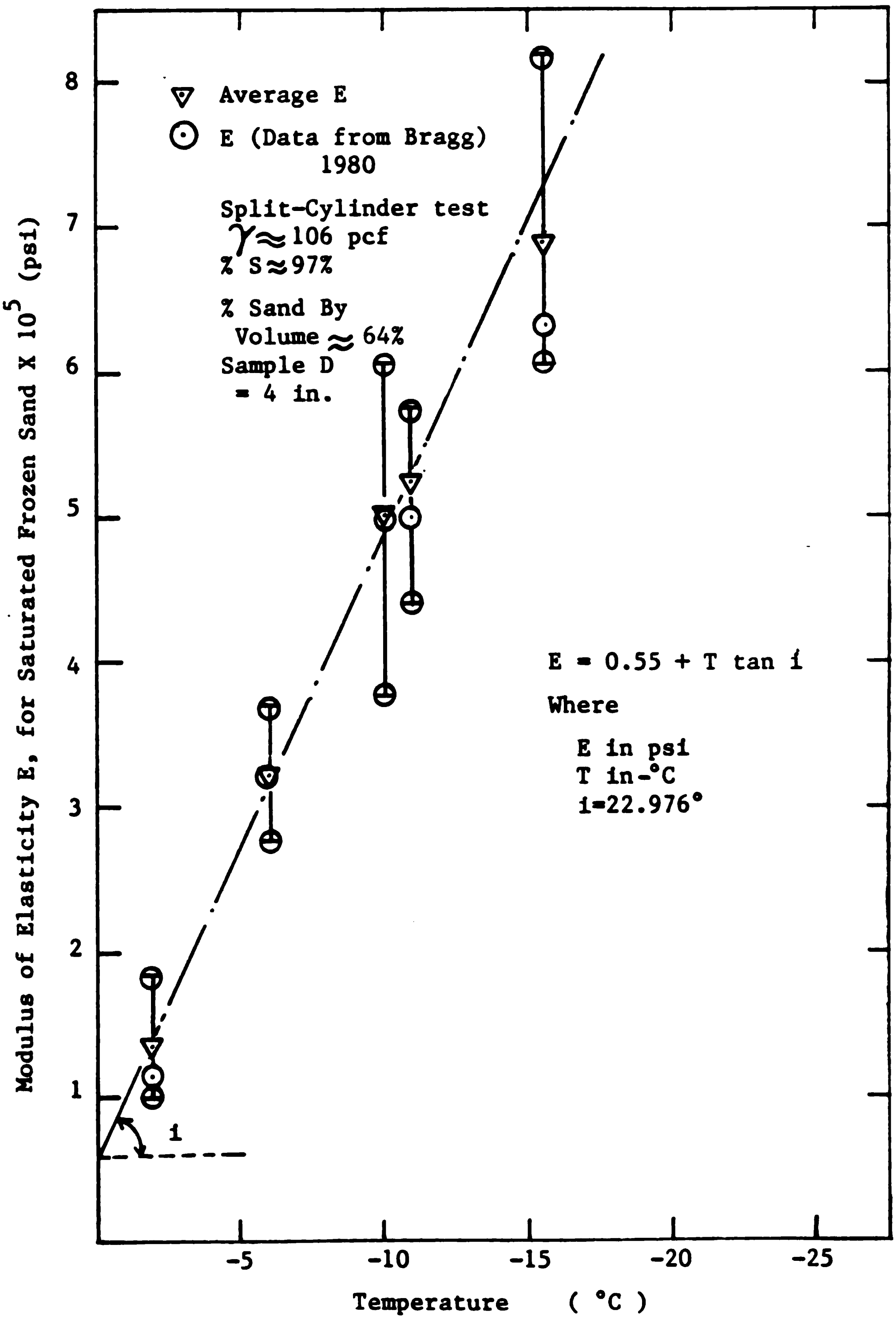

Figure 5-7: **Effect of Temperature on the Modulus of Elasticity of Saturated Frozen Sand (Data from Bragg, 1980).**

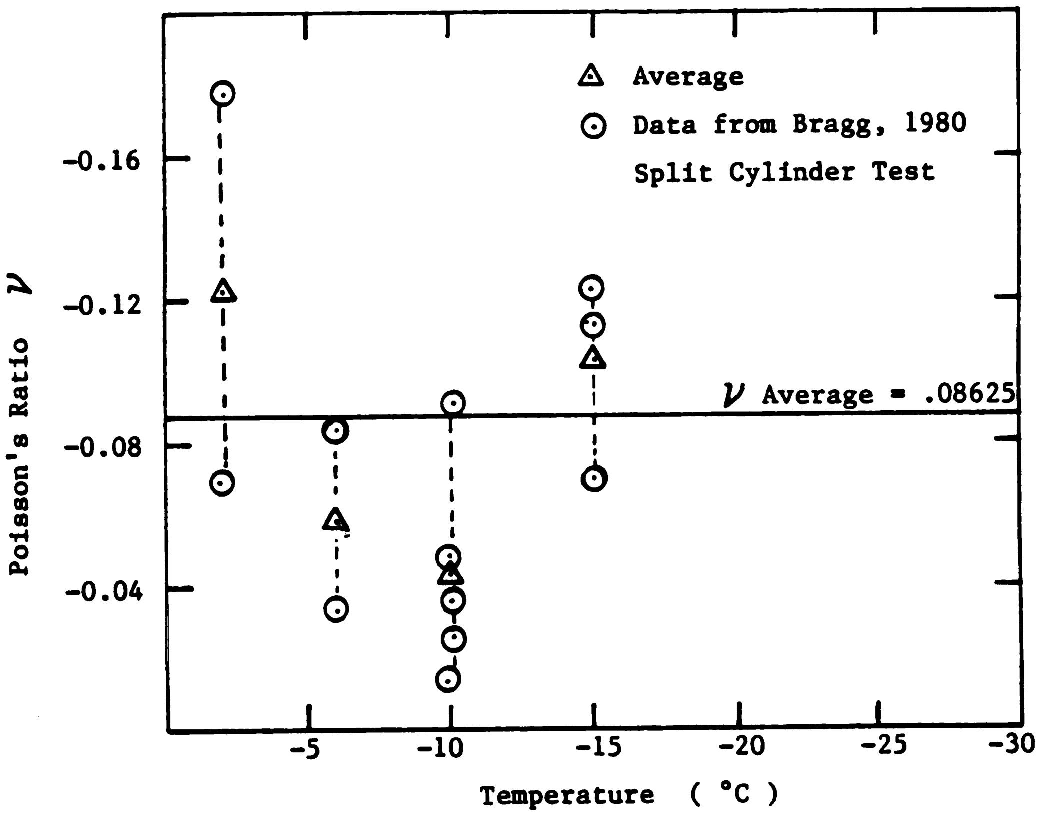

Figure 5-8: Effect of Temperature on Poisson's Ratio of Saturated Frozen Sand (Data from Bragg, 1980).

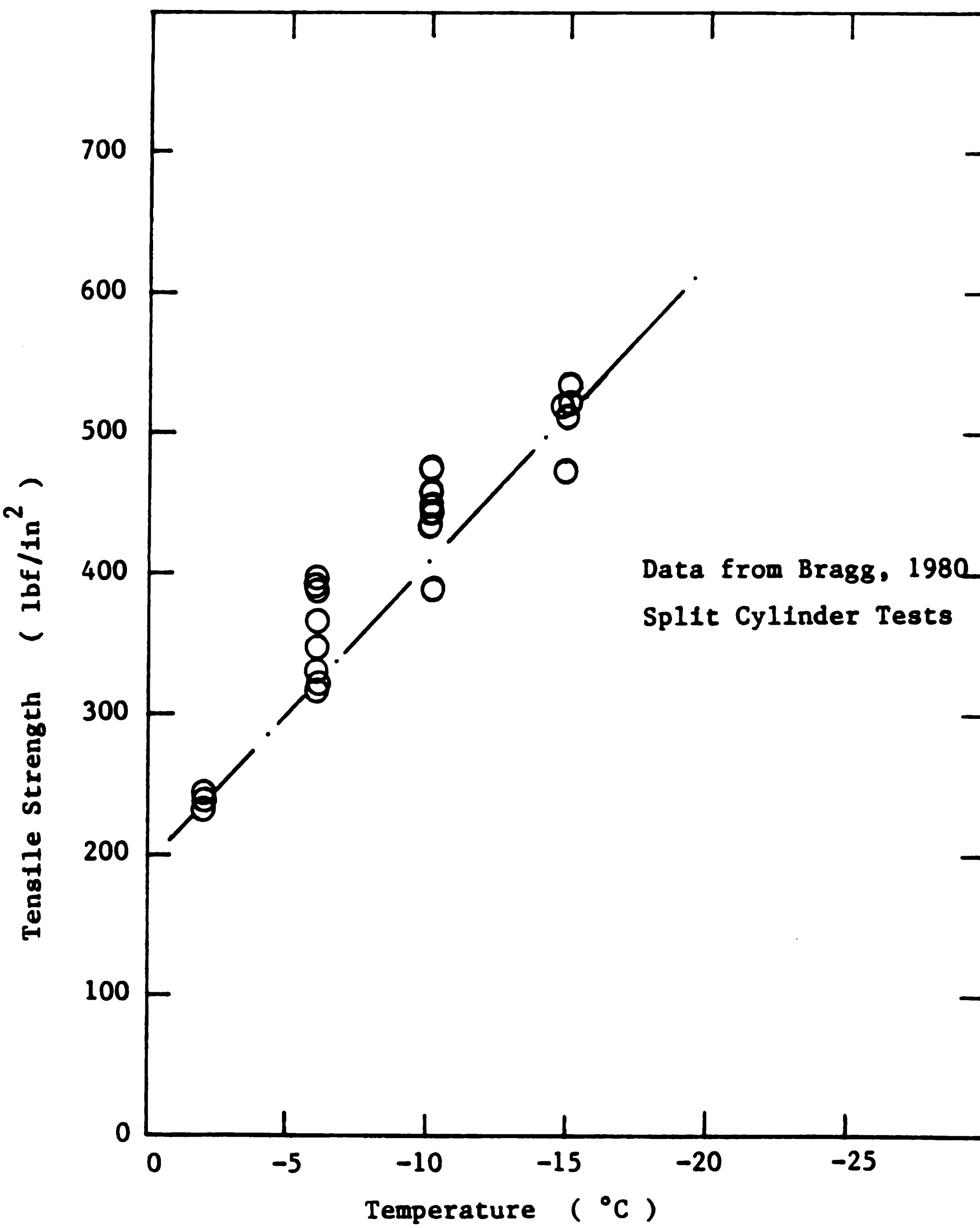

Figure 5-9: Effect of Temperature on Tensile Strength of Saturated Frozen Sand (Data from Bragg, 1980).

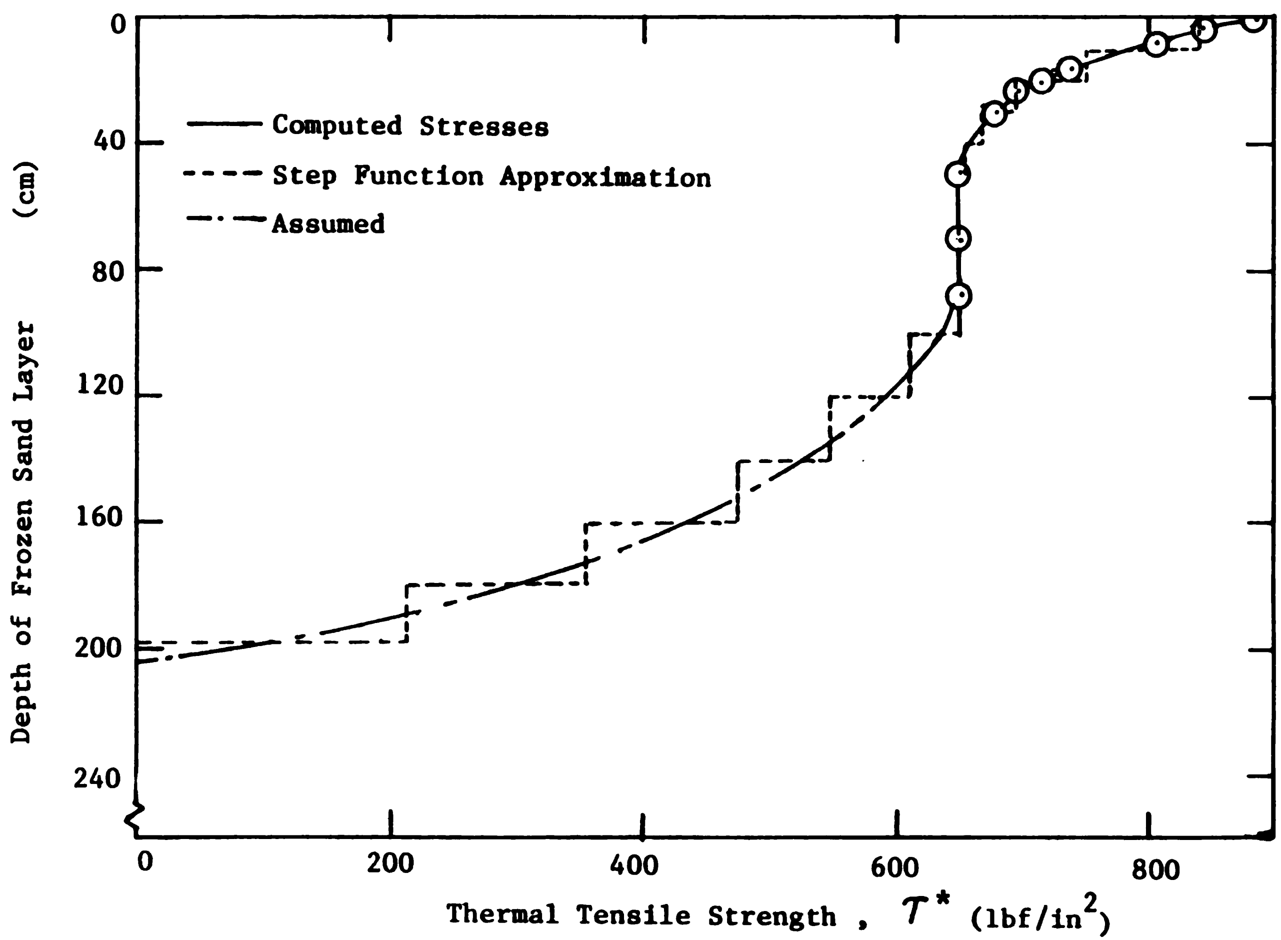

Figure 5-10: Thermal Tensile Stress versus Depth at Fargo, North Dakota, on 2-3 February, 1974 at 21 hours.

temperature data at 3-hr intervals are listed in Table (5-1) along with data for 2 other locations. Frost penetration in a sand deposit, above the water table, for Fargo, North Dakota, and the 1973-74 winter season would be close to 205 cm based on the modified Berggren equation (Aldrich and Paynter, 1953). Cooling rates for each 3-hr interval are listed in Table (5-1). Computed ground temperatures and thermal properties for the saturated sand (γ_d = 1693.18 kg/m^3 and w = 21.13 %) are given in Table (5-2).

The crack stress intensity factor, K_I, due to thermal stress, was calculated as a function of crack depth b using equation 4-66 with values tabulated in Table (5-7). The crack driving force, G, computed in terms of K_I using equation 4-69, is included in Table (5-7). Values for K_I and G are graphically represented in figure (5-11). The following example illustrates calculations required for estimating the crack depth.

<u>Example 4</u>.

Calculation of K_I and G for a crack depth b = 20 cm involves the following steps: From Equation 4-66

$K_I = 2/\pi \cos^{-1} a/b \, [1 + F(a/b)] \, \sigma\sqrt{b}$ and $K_I = 1.12147 \, \sigma\sqrt{b}$, for a = 0.

For b = 20 cm = 7.87 inch, and using the superposition method obtain

$K_I = 1.12147 \, (840) \sqrt{7.87} - 2/\pi \cos^{-1} 1/2 \, [1 + F(1/2)] \, (95) \sqrt{7.87}$

From Table (4-3) read F(1/2) = 0.05874 and K_I = 2454.63 Ib/in$^{3/2}$

Recall Equation 4-63 where $K_I = p \sqrt{b} \, [1 - 2/\pi \cos^{-1} (a/b)]$. Compute

$$K_I = 90 \sqrt{7.87} \, [1 - 2/\pi \cos^{-1} (1/10)]$$
$$+ 750 \sqrt{7.87} \, [1 - 2/\pi \cos^{-1} (1)]$$
$$+ 95 \sqrt{7.87} \, [1 - 2/\pi \cos^{-1} (1/2)] = 2040.62 \text{ Lb/in}^{3/2}$$

Table 5-7: Stress Intensity Factor K_I and Crack Driving Force G.

Crack Depth b (cm)	^+K_I ($lb/in^{3/2}$)	^+G (lb/in)	$^\#K_I$ ($lb/in^{3/2}$)	$^\#G$ (lb/in)
0	0.0	0.0	0.0	0.0
5	1342.6	2.579	1196.63	2.049
10	1838.7	4.838	1635.63	3.828
15	2176.2	6.778	1953.27	5.460
20	2454.63	8.623	2040.62	5.959
25	2653.3	10.075	2349.719	7.902
30	2822.57	11.402	2516.364	9.062
50	3489.19	17.42	3135.05	14.06
70	4032.30	23.27	3593.62	18.48
90	4552.84	29.66	4027.18	23.21

(1) $\nu = 0.08625$ = Poisson's ratio (Bragg, 1980).

(2) $E_{avg} = 6.935 \times 10^5$ lb/in^2 = average Young's modulus.

(3) $G = [(1 - \nu^2)/E]\, K_I^{\,2}$ = crack driving force for plane strain (Hellan, 1984).

\+ Values based on Koiter (1965) and Hartranft and Sih (1973) equations using superposition.

\# Values based on Lachenbruch (1962) equation for a semi-infinite media using a step function distribution where

$K_I = p\sqrt{b}\,[1 - (2/\pi)\cos^{-1}(a/b)]$ and superposition of stresses.

Note: Lachenbruch's solution gives values 10 percent less than the Koiter, Hartranft, and Sih solution due to different assumptions. The latter values are used in the field example.

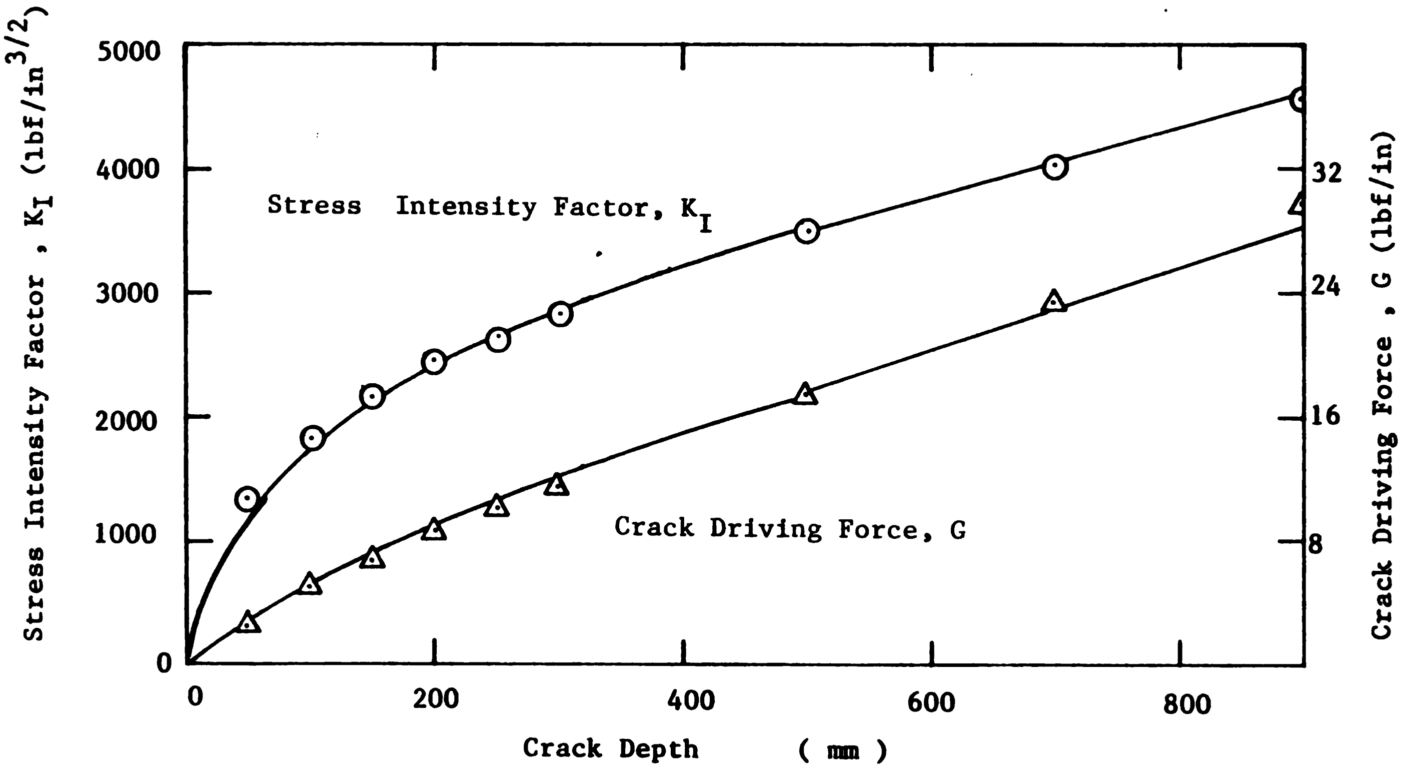

Figure 5-11: Crack Driving Force G, and Stress Intensity Factor k_I, as a Function of Depth b for The Temperature and Soil Conditions Assumed for Fargo, North Dakota, on 2-3 February, 1974.

Using Equation 4-69 $\quad G = [(1 - \nu^2)/E]\, k_I^2$

For the Koiter (1965) and Hartranft and Sih (1973) solutions, the stress intensity factor is $K_I = 2454.63$ Ib/in$^{3/2}$ and

$G = [(1 - (0.08625)^2)/6.935 \times 10^5]\ (2454.63)^2 = 8.623$ Lb/in

Using the Lachenbruch (1962) solution gives $K_I = 2040.62$ Lb/in$^{3/2}$ and $G = [(1 - (0.08625)^2)/6.935 \times 10^5]\ (2040.62)^2 = 5.959$ Lb/in

These values are listed in Table (5-7).

In Example 4 an assumed homogeneous layer of frozen sand with a depth of 2050 mm was analyzed. In the field other sites may involve a combination of different soil strata. Each layer will have different thermal properties with different unfrozen water contents. Hydrostatic pressures, in the form of compressive stresses on crack surfaces, will tend to close the cracks with increase in depth. In general, for more than one layer both K_I and the crack driving force will start from zero for the zero depth, increase to a peak value at some depth and then return to zero at a greater depth. Therefore, the crack depth will be controlled by values of G and G_0 as explained in Chapter III.

Table (5-6) shows that thermal tensile stress is higher than the sum of the tensile strength and residual stress down through the 90 cm section which was analyzed. The estimated residual stress of 175 psi was based on a temperature of -15 °C at the 90 cm depth were the ground temperature is -24.56 °C. This indicates that the residual stress of 175 psi is low and that failure would occur below the 90 cm depth.

The error function limitation in equation 5-8 prevents computation of ground temperatures below 90 cm. Temperature at the frost line would be at zero degrees Celsius. Lack of experimental work on fracture toughness evaluation limits the analysis of the critical crack depth, but it appears that for a partially saturated soil with lower strength and residual stresses from prior cooling that the crack would continue through the frozen layer.

5.2.3 Horizontal Stress Relief and Crack Spacing

Consider now the effect of the crack in relieving tensile stresses near the surface. Apply the multiple step-function approximation of $\tau^{*}(x)$ (Figure 5-10) for assumed crack depths b equal to 5, 10, 20, and 30 cm to calculate the stress at a given horizontal distance. The results using Figure (4-6), are given in Table (5-8) and shown in Figure (5-12). As may be expected, all four cracks relieve surface stress in the same way to a horizontal distance of about 5 cm. Beyond 5 cm the constraint at the bottom of the 30 cm cracks becomes apparent, and the stress relief drops sharply to 5 percent at a horizontal distance of about 200 cm. Similarly, the effect of the 20 cm crack does not differ from that for the 30 cm crack for horizontal distances much less than 30 cm. Five percent stress relief is achieved by the 10 cm crack at a horizontal distance of 82 cm and by the 5 cm crack at about 40 cm. Assuming that crack spacing was determined by the distance to points of 5 percent stress relief, the four crack depths would be associated with minimum spacing of 200, 170, 92, and 40 cm.

Varying the crack depth will effect the width of the zone of stress relief, but crack depth is a function of soil brittleness (G_0) so that in fine-grained soils the cracks will be more closely spaced as compared to coarse-grained soils. Part of the reason is due to the more plastic behavior of fine-grained soils under concentrated stress (higher G_0).

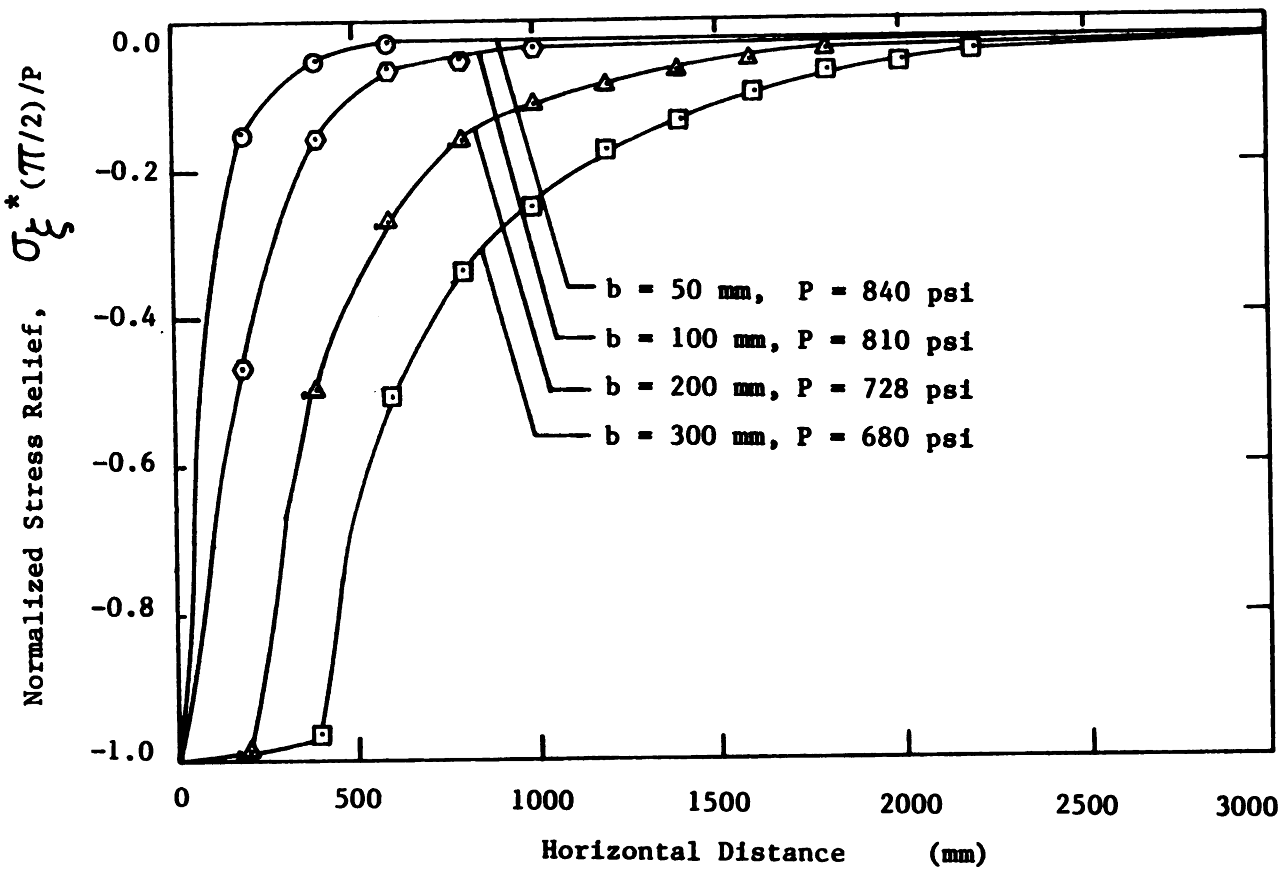

Figure 5-12: Calculated Stress Relief at the Ground Surface in the Direction Normal to the Crack (Based on Temperature Data for Fargo, North Dakota, 2-3 February, 1974).

Table 5-8: Normalized Stress Relief $\sigma_\xi^*(\pi/2)/P$

Horizontal Distance y (cm)	$\sigma_\xi^*(\pi/2)/P$ b = 5 cm, p = 853 psi	b = 10 cm, p = 840 psi	b = 20 cm, p = 728 psi	b = 30 cm, p = 680 psi
20	-0.150	-0.465	-0.995	-0.998
40	-0.050	-0.158	-0.499	-0.966
60	-0.025	-0.062	-0.267	-0.512
80	—	-0.051	-0.159	-0.341
100	—	-0.025	-0.109	-0.227
120	—	—	-0.086	-0.170
140	—	—	-0.065	-0.136
160	—	—	0.054	-0.101
200	—	—	0.031	-0.076
240	—	—	—	-0.056
300	—	—	—	-0.028

Although not illustrated in this example, the effect of varying the stress regime is just as important to the configuration of the zones of stress relief as is varying the crack depth. Thus, a crack forming early in the winter will have a narrow zone of stress relief, as most of the thermal tension will be confined to surficial layers. With the advancing season, thermal stress $\tau^*(x)$, crack depth b, and the surficial stress relief $\sigma_\xi(\pi/2)$, will change according to the complex interaction of other factors. Calculations for stress relief are illustrated in example 5.

Example 5.

The following steps were used to find the normalized stress relief at a given horizontal distance y from the crack. For a crack depth b = 10 cm and y = 40 cm, the average uniform pressure P on the crack surface, Figure (5-10) gives P = 840 psi. From Figure (5-10), a = 10 cm and b = 10 cm. Therefore a/b = 1 and y/b = 40/10 = 4. From Figure (4-6) for a/b = 1 and y/b = 4 read $\sigma_\xi^*(\pi/2)/P = -0.1556$ as shown in Table (5-8). Values of normalized stress relief are given in Table (5-8) for different value of crack depth b.

5.2.4 Inelastic Effects after Soil Rupture

For previous computations horizontal stress relief was computed from Figure (4-6), which applies strictly only to elastic media. Once a crack has been initiated in a solidly frozen soil, it probably propagates rapidly to an equilibrium depth, b, leaving little time for large-scale inelastic effects. The stress relief depicted in Figure (5-12) shows the stresses which would be obtained immediately after fracturing.

Although the crack acts to decrease distortional stresses near the surface, it concentrates them near its tip. Thus, under a constant thermal-stress regime, a crack that propagated rapidly to some initial equilibrium depth would close slowly from the bottom at a progressively decreasing rate as the large shears near its tip relaxed. This would be accompanied by a corresponding contraction of the zone of stress relief. However, the stress perturbation caused by the crack could still be approximated by superposition using the new reduced value of crack depth.

5.3 Discussion with Design Implications

In cold regions, special attention must be directed to the disturbing effects of ground freezing, subsequent thermal contraction, and potential cracking. A substatial decrease in effectiveness of soil covers for limiting water and gas migration may result from cracking. Lutton (1982) suggested that cover thickness be 1 ft more than the average annual maximum depth of freezing to avoid disturbance of the cover. It is likely that thermal contraction cracks will penetrate the frozen layer as shown in Section 5.2.2.

5.3.1 Landfill Covers

Landfill covers designed for hazardous waste landfills serve multiple functions. The surface layer (Figure 5-13) is intended for vegetation, the clay serves as a barrier for infiltration of water and prevents escape of gases, and the gravel serves as a gas channel. Layering serves as a technique for designing solid waste landfill covers. By combining two or three distinct materials in layers, the designer mobilizes favorable characteristics of each material together at minimal expense.

The cover top soil typically will be a loose, 6-12 inch, loamy soil suitable for supporting vegetation. The underlying clay barrier layer is a critical cover component because it is intended to minimize the transmission of water that would contribute to leachate generation and of gas that might kill vegetation and pose an explosion or other hazard. A buffer or foundation layer, sand or other soil, protects the barrier from damage. A buffer soil may also be placed above the clay barrier layer to increase depth in areas of deep frost penetration. Soil

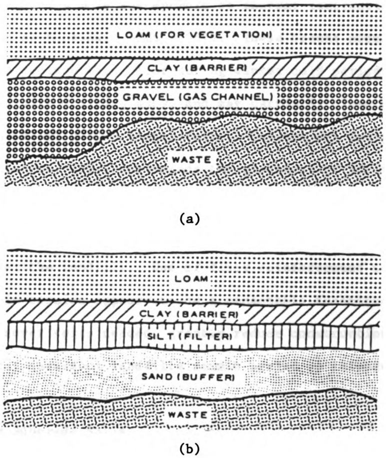

Figure 5-13: Two Representative Systems for Layered Solid Waste Covers (Lutton, 1982).

densities will correspond to those accomplished during spreading of cover soil with dozers and other compacting equipment. The top soil is placed in a loose condition and not compacted.

For surface soils, including landfill covers and exposed soil liners located above the water table, partial soil ice saturation make these earth structures more susceptable to thermal contraction cracking (Andersland and Al-Moussawi, 1985, 1987). These cracks normally would not be observed because they occur during winter cold periods, may be quickly covered with drifting snow, and may partially close as spring approachs with warmer ground temperatures. Current EPA design (Lutton, et al., 1979; Lutton, 1982) recommends the placement of additional cover soils to prevent freezing and potential cracking of the clay barrier. This can be rather expensive due to the large soil volumes required to adequately cover the landfill. Use of fiber reinforcement to enhance soil behavior in tension appears to be a reasonable technique to reduce the volume of cover soils needed, greatly reduce construction costs, and help insure that hazardous landfills remain sealed as intended.

5.3.2 Highway Subgrade Soils

Modern highway design involves the placement of special pavement layers over subgrade soils. These layers are designated as surface, binder, and base courses as indicated in Figure (5-14). The upper layer may consist of a deep layer of asphalt concrete pavement placed directly on an aggregate base course or Portland cement concrete placed on a granular base. These materials generally have higher thermal conductivities than soils and contain little or no moisture, hence little or no latent heat effects or heat conduction are present. The

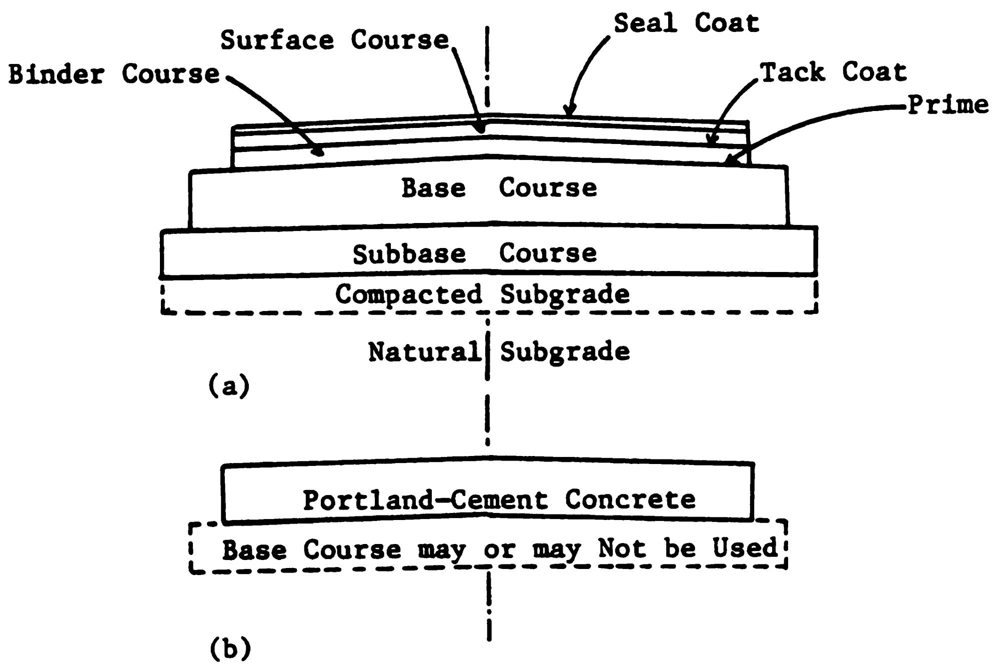

Figure 5-14: Components of (a) Flexible and (b) Rigid Pavements (Yoder and Witczak, 1975).

result is that freezing temperatures will penetrate more quickly and to greater depths into and below the pavement structure.

Pavement structures, typically about 600 mm in thickness, are placed directly on suitable subgrade soils. Good drainage is designed into system so that detrimental effects of high water contents on soil subgrade support are avoided. Good drainage will decrease soil water contents to levels shown in Figure (5-14) with values approaching zero percent for coarse sand materials. Compression tests on partially saturated frozen sand (Alkire and Andersland, 1973) show that strength of unconfined samples decreases almost linearly with decrease in ice content. Since the ice matrix is primarily responsible for frozen soil tensile strengths, it is reasonable to assume that tensile strengths for the pavement subgrade soils would normally be very low and conducive to failure in tension.

Transverse pavement cracking, caused by thermal contraction at low temperatures, has been reported as the second principal nontraffic associated mode of distress in highway structures (NCHRP synthesis 26, 1974). Most of the highway agencies surveyed in this synthesis reported that contraction cracks significantly affected the serviceability of their roads and that the seriousness of the problem had been recognized only within the past 10 to 15 years. Fromm and Phang (1972) and Nady (1972) called attention to the fact that transverse contraction cracks penetrate into the subgrade soils. The lower tensile strengths of these subgrade soils in the zone of seasonal frost depth penetration can only contribute to the thermal cracking problem.

There is clearly a need for extension of the work reported herein on prediction of thermal crack depth to multiple layered frozen soil and/or pavement systems. The highway engineer should be able to predict potential thermal cracking for highway structures in his state based on local freezing indices, pavement structure, and soil conditions. When thermal cracking is found to be a problem, then techniques must be developed on how to avoid the problem or to minimize the cracking effects on pavement structures so as to avoid costly highway maintenance problems.

The preliminary compression tests on fiber reinforced frozen sand samples suggest one approach for strengthening frozen subgrade soils in tension. Stress-strain data for saturated frozen sand (Eckardt, 1982) and for silt (Yuanlin and Carbee, 1987) in tension shows failure at strains ranging from 1/2 to 2 percent. Fiber reinforcement would increase the axial strain at failure. Now add the increase in tensile strength contributed by the fibers and thermal cracking should be limited, possibly prevented. With a reduced post-peak loss in strength, the strain which does occur will help reduce tensile stresses and thus help prevent the formation of thermal cracks. With seasonal (summer) thaw the highway subgrade soils would return to their normal unfrozen stress conditions before a repeat of lowered temperatures and thermal contraction during the following winter season.

CHAPTER VI

SUMMARY AND CONCLUSIONS

6.1 Summary

The earth's surface temperatures fluctuate on the order of 25 °C about the mean through the combined effects of changing seasons and shorter period random and diurnal changes. For those regions with mean annual temperatures a few degrees above zero degrees Celsius, for example 4.4 °C for Fargo, ND, winter temperatures will freeze surface soils to depths of 2 m and more. During periods of decreasing winter temperatures, cooling of surface soils with thermal contraction can increase tensile stresses to levels greater than the tensile strength. For those soils located above the water table with reduced degrees of ice saturation and lower tensile strength, the potential for crack formation is fairly high. This phenomenon creates engineering problems for landfill covers, highway subgrade soils, and hydraulic earth structures (dams, dikes, etc.).

To provide more information on this problem, preliminary experimental work was conducted which included thermal contraction/ expansion measurements along with some thermal tensile and stress relaxation tests on a frozen sand. These tests have provided information useful for an analyses of the problem. Compression tests on fiber reinforced frozen sand provided limited information on one technique which appears to be suitable for prevention of thermal cracking in surface soils.

An example calculation (Chapter V) for prediction of crack depth and stress relief adjacent to the crack is based on theoretical work reported by Muskhelishvili (1963). This work assumes that the crack involves two parallel lines in an infinite media. By pulling these two lines apart, a crack shape will form an ellipse. The ellipse is mathematically hard to formulate, therefore complex variables are utilized to map an ellipse into a circle. Then a solution for the stress in the region was formulated. By mapping the circle back to an ellipse and taking a limit for the minor axis of the ellipse, the problem is returned to the square (one), i.e. (two parallel lines). Using superposition, and considering an attraction free surface for the crack, the solution for the stress, in a semi-infinite media, was formulated from the infinite media solution. Data from experimental work, and theoretical considerations leads to the thermal crack solution presented in Chapter V, the field example.

This example illustrates the complexity of the problem and confirms that thermal cracking will occur in the frozen surface soil assumed for the Fargo, ND, example. In the field example local air temperatures were used with the Stefan equation to calculate the depth of frost. The error function, with a sudden step change in temperature was used to calculate temperature of the ground versus time.

To calculate the stress intensity factor k_I, crack driving force G, and horizontal stress relief distance, stresses were approximated by a step function. For case 1, the step function solution from Muskhelishvili (1963) was utilized. Increasing the crack depth from 50 mm to 300 mm, reduced the instability for crack growth, and increased the distance needed for stress relief. For a crack depth of 30 cm, a distance of 180 cm was needed to decrease the stress to 10% of it's initial value, while for a crack depth of 50 cm a distance of 232 cm was needed to decrease the stress to 10% of it's value.

Compression tests on reinforced frozen soil, showed that fiber reinforcement improved the compressive strength and increased the strain to failure for frozen sand. Adding fiber to frozen soils will be one of the more promising solutions available to help overcome the thermal cracking problem in frozen surface soils.

6.2 Conclusions

The conclusions from this study involve several areas ranging from soil behavior to fracture mechanics. They are given below under the following headings: thermal cracking, crack depth, thermal contraction coefficients, soil tensile behavior, and soil property enhancement.

Thermal Cracking:

Frozen surface soils under decreasing winter temperatures are subject to thermal contraction, increase in tensile stresses, and potential crack formation. Recorded air temperatures for three sites -- Fargo, ND, Madison, WI, and Lansing, MI -- all showed temperature changes which have the potential for initiating crack formation. The surface soils for these sites are generally above the water table with only partial saturation. Frozen soil tensile strengths are reduced in proportion to the degree of ice saturation, thus adding to the probability of crack formation when subjected to decreasing temperatures.

Crack Depth:

An understanding of the fracture process and prediction of crack depth involves use of a "crack stress-intensity factor". This parameter characterizes the elastic stress across the plane of the crack at a small distance in advance of the crack edge. A reasonable crack depth was predicted in the frozen sand using assumed values for the parameter based on information reported for other materials. Use of crack depth or a high potential for thermal cracking as a limiting criterion in the modification of soils used in landfill covers, liners, and other earth structures appears to be a reasonable future objective.

Thermal Contraction Coefficients:

Thermal contraction is that change in length, or volume, of a material resulting from a decrease in temperature. Frozen sand is a composite material in which contraction involves both the quartz particles and the ice matrix, each with its own coefficient of thermal contraction. The effect of temperature on the coefficient for a saturated frozen sand was very small, ranging from 34×10^{-6} °C^{-1} at -5 °C to 26×10^{-6} °C^{-1} at -25 °C. A change in dry density (1.96 mg/m^3 to 2.28 mg/m^3) involved a change in the coefficient by less than 2×10^{-6} °C^{-1}. For natural sands with densities in the above range, this change in the coefficient can be assumed to be negligible for many projects. A change in the degree of soil saturation will effect the coefficient in proportion to the change in volume fraction of water in the soil. For a sand specific gravity of 2.65 and a change in degree of ice saturation from 60 to 100 percent, the coefficient of thermal contraction would increase by about 8.5×10^{6} °C^{-1}.

Soil Tensile Behavior:

Frozen soil behavior in tension was observed using thermal tensile tests and stress relaxation tests on saturated frozen quartz sand. The cross-plot of tensile stress versus temperature showed the dependence of stress increase on rate of cooling and concurrent uniaxial creep and stress relaxation. The increase in $d\sigma/dT$ at colder temperatures reflects greater material stiffness with a more rapid stress increase on cooling and agrees with field observations (Lachenbruch, 1961) that thermal cracking occurs more readily in colder frozen soils.

The stress relaxation tests confirmed that an accumulation of permanent strain over a number of load cycles leads to a decrease in tensile strength. During a series of winter storms, cyclic temperature changes along with an accumulation of strain may lead to rupture when the total tensile strain approaches one percent. The study showed that thermal stresses can be higher than soil strengths, which is the main reason for crack initiation and propagation. But more important than the thermal tensile stress is the thermal history for a given site.

Soil Property Enhancement:

Frozen soils with partial ice saturation have low tensile strengths, hence they are susceptible to cracking when temperatures decrease by several degrees. Preliminary compression tests on cylindrical frozen sand specimens showed that fiber reinforcement greatly improved their strength properties. The frozen sand with randomly distributed discrete fibers showed an increase in compressive strength, an increase in axial strain at failure, and a reduced post-peak loss of strength. A similar behavior would be anticipated for frozen soils in tension. All three factors would then contribute to a reduction in the probability of cracking due to high tensile stresses caused by thermal contraction.

6.3 Recommended Research

The application of fracture mechanics to the thermal cracking problems in frozen surface soils has shown the need for information on several topics. The fracture process involves a stress-intensity factor which characterizes the stress across the plane of the crack at a small distance in advance of the crack edge. How should this parameter be evaluated for frozen soils? Other factors involve the energy required to extend a crack, first to overcome cohesive forces and to produce new surfaces, and second, to do the work of plastic deformation at the crack tip. How is this energy related to the strain energy released from the frozen soil when tensile stresses are relieved? Questions remain relative to determination of a crack growth resistance (R) curve for the frozen soil. If the frozen soil mechanical properties are enhanced by fiber reinforcement, how will this alter the stress-intensity factor and the crack driving force?

A numerical example was used to illustrate factors effecting crack depth and stress relief with distance from the crack in a sand frozen to a finite depth. Parameters are needed which will permit crack depth prediction and stress relief in multiple layered systems, such as highway pavement structures and landfill covers with different soil types. How will the interaction of layers effect stress relief with distance from the crack and crack spacing?

Crack formation creates serious engineering problems relative to landfill covers, exposed liners, highway subgrade soils, and hydraulic earth structures exposed to winter climatic conditions. Fiber reinforcement represents a potential method by which the thermal cracking problem can be mitigated in many areas. There is a need for information on the type of fiber reinforcement most suitable and the volume fraction of fibers required to provide the soil properties needed to eliminate or minimize the effects of thermal cracking. Specific information needed relates to fiber volume fraction and (a) increase in tensile strength, (b) increase in axial strain at failure, and (c) the effect on post-peak tensile strength for the fiber reinforced frozen sand.

BIBLIOGRAPHY

BIBLIOGRAPHY

Aldrich, Harl P. Jr., and Paynter, Henry M. 1953. Analytical studies of freezing and thawing of soils. Artic Construction and Frost Effects Laboratory, Boston, Mass., Technical Report No. 42.

Alkire, B. D., and Andersland, O. B. 1973. The effect of confining pressure on the mechanical properties of sand-ice materials. Journal of Glaciology, Vol. 12, No. 66, pp. 469-481.

AL-Moussawi, Hassan M., and Andersland, O. B. 1988. Discussion of "Behavior of fabric versus fiber-reinforced sand", J. of Geotechnical Engineering, American Society of Civil Engineers, 114 (3).

Andersland, O. B. 1987. Frozen ground engineering. Chapter 8 in GROUND ENGINEER'S REFERENCE BOOK, edited by F. G. Bell. Butterworths, London, pp. 8/1 - 8/24.

Andersland, O. B., and AL-Moussawi, Hassan M. 1985. Thermal contraction and crack formation potential in soil landfill covers. Proceedings, International Conference on New Frontiers for Hazardous Waste Management, U.S. Environmental Protection Agency. Publication EPA/600/9 - 85/025(SEP.), pp. 274-281.

Andersland, O. B., and Al-Moussawi, Hassan M. 1987. Crack formation in soil landfill covers due to thermal contraction. Waste Management and Research, J. of the International Solid Wastes and Public Cleansing Association, Academic Press Inc. (London) Ltd., 5, pp. 445-452.

Andersland, O. B., and Al-Moussawi, Hassan. 1988. Cyclic thermal strain and crack formation in frozen soils. Fifth international symposium on ground freezing, (26th - 28th, July), Nottingham, England, (Accepted, 1987).

Andersland, O. B., and Anderson, D. M. 1978. GEOTECHNICAL ENGINEERING FOR COLD REGIONS, McGraw-Hill Book Co., New York.

Anderson, D. M., and Tice, A. R. 1972. Predicting unfrozen water contents in frozen soils from surface area measurements. Highway Research Board, Washington, D. C., Record No. 393. pp. 12-18.

Anderson, D. M., Tice, A. R., and McKim, H. L. 1973. The unfrozen water and the apparent specific heat capacity of frozen soils. PERMAFROST, North Am. Contrib. 2nd. Int. Conf., Yakutsk, U.S.S.R., National Academy of Sciences, Washington, D.C., pp. 289-295.

Arpaci, Vedat S. 1966. CONDUCTION HEAT TRANSFER. Addison-Wesley Publishing Company, Reading, Massachusetts.

ASTM Desination E 616-82. Standard terminology relating to fracture testing.

ASTM Desination E 399-83. Standard Test Method for Plane-Strain Fracture Toughness of Metallic Materials.

ASTM Desination E 561-86. Standard practice for R-curve determination.

Bragg, Richard A. 1980. Material properties for sand-ice structural systems. Unpublished Ph.D. dissertation, Michigan State University, East Lansing, Michigan.

Bragg, Richard A.; and Andersland, O.B. 1981. Strain rate, temperature, and sample size effects on compression and tensile properties of frozen sand. Engineering Geology, Elservier Scientific Publishing Company, Amsterdam, The Netherlands, pp. 35-46, Vol. 18.

Butkovich, T. R. 1957. Linear Thermal Expansion of Ice. U.S. Army Snow Ice and Permafrost Research Establishment, Corps of Engineers, Wilmette, Illinois, Research Report 40.

Carothers, S. D. 1920. Plane Strain; The direct determination of stress. Proceedings of the Royal Society of London, Series A. Vol. XCVII, pp. 110-123.

Department of the Army and the Air Force. 1966. Calculation methods for determination of depths of freeze and thaw in soils. U. S. Government Printing Office, Technical Manual, TM 5-852-6 (Jan.).

Department of the Army, Corps of Engineers. 1958. Frost Conditions, Chapter 4, in Airfield Pavement Design. U.S. Government Printing Office, Engineering Manual, EM 1110-345-306 (Mar.).

Eckardt, H. 1982. Creep tests with frozen soils under uniaxial tension and uniaxial compression. The Roger J. E. Brown, Memorial Volume, Proceedings, 4th Canadian Permafrost Conference. Calgary, Alberta (March 2-6, 1981), H. M. French (editor), National Research Council of Canada, Ottawa, pp. 394-405.

Farouki, O. T. 1981. Thermal Properties of Soils. U.S. Army Cold Regions Research and Engineering Laboratory, Hanover, New Hampshire, CRREL MONOGRAPH 81-1 (Dec.).

Farouki, O. T. 1982. Evaluation of methods for calculating soil thermal conductivity. U.S. Army cold Regions Research & Engineering Laboratory, Hanover, New Hampshire, CRREL Report 82-8.

Fromm, H. J.; and Phang, W. A. 1972. A study of transverse cracking of bituminous pavements, Proc. Assoc. Asphalt Paving Tech. Vol. 41, pp. 383-423.

Fuchs, H. O.; and Stephens, R. I. 1980. METAL FATIGUE IN ENGINEERING, John Wiley and Sons, New York.

Hartranft, R. J.; and Sih, G. C. 1973. Alternating method applied to edge and surface crack problems. Chapter 4 in MECHANICS OF FRACTURE 1, METHODS OF ANALYSIS AND SOLUTIONS OF CRACK PROBLEMS, edited by G. C. Sih. Noordhoff International Publishing, Leydon, The Netherlands, pp. 179-238.

Haynes, F. D.; Carbee, D. L.; and Vanpelt, D. J. 1980. Thermal diffusivity of frozen soil, U.S. Army Cold Regions Research and Engineering Laboratory, Hanover, New Hampshire, CRREL, SR 80-38.

Haynes, F. D.; Karalius, J. A.; and Kalafut, J. 1975. Strain rate effect on the strength of frozen silt. U.S. Army Cold Regions Research and Engineering Laboratory, Hanover, New Hampshire. CRREL, RR 350.

Haynes, F. D.; and Karalius, Jack A. 1977. Effect of temperature on the strength of frozen silt, U.S. Army Cold Regions Research and Engineering Laboratory, Hanover, New Hampshire, CRREL, Report 77-3.

Hellan K. 1984. INTRODUCTION TO FRACTURE MECHANICS, McGraw-Hill Book Company, New York.

Hoekstra, P. 1969. The physics and chemistry of frozen soils. Effects of Temperature and Heat on Engineering Behavior of Soils, Proceedings of an International Conference, Highway Research Board. Washington, D.C., Special Report 103, pp. 78-90.

Hooks, C. C. 1965. Laboratory thermal expansion measuring techniques applied to bituminous concrete. Unpublished MSCE thesis, Purdue University, West Lafayette, Indiana.

Irwin, G. R. 1957. Analysis of stress and strain near the end of a crack traversing a plate. J. of Applied Mechanics, ASME, Vol. 24, pp. 361-364.

Johansen, Ø.; and Frivik, P. E. 1980. Thermal properties of soils and rock materials. Preprints, the 2nd International Symposium on Ground Freezing. The Norwegian Institute of Technology, Trondheim, Norway, Jun 24-26.

Jones, G. M., Darter, M. I., and Littlefield, G. 1968. Thermal expansion of asphalt concrete. Proceedings of the Association of Asphalt Paving Technologists, Vol. 37, pp. 56-100.

Kachanov, L. M. 1986. INTRODUCTION TO CONTINUUM DAMAGE MECHANICS. Martinus Nijhoff Publishers, Dordrecht, The Netherlands.

Kaplar, Chester W. 1971. Some strength properties of frozen soil and effect of loading rate. U.S. Army Cold Regions Research and Engineering Laboratory, Special Report 159, Hanover, New Hampshire.

Kay, B. D.; and Goit, J. B. 1975. Temperature-dependent specific heats of dry soil materials. Canadian Geotechnical Journal, Vol. 12, pp. 209-212.

Kersten, M. S. 1949. Laboratory research for the determination of the thermal properties of soils, Univ. Minn. Eng. Exp. 5th, Final Rep.

Koiter, W. T., and Benthem, J. P. 1973. Asymptotic approximations to crack problems. Chapter 3 in MECHANICS OF FRACTURE 1, METHODS OF ANALYSIS AND SOLUTIONS OF CRACK PROBLEMS, edited by G. C. Sih, Noordhoff International Publishing, Leydon, The Netherlands, pp. 131-178.

Koiter, W. T. 1965. Rectangular tensile sheet with symmetric edge cracks. Journal of Applied Mechanics, Vol. 32, p. 237.

Lachenbruch, A. H. 1961. Depth and spacing of tension cracks. J. of Geophysical Research, Vol. 66, No. 12, pp. 4273-4292.

Lachenbruch, A. H. 1962. Mechanics of thermal contraction cracks and ice-wedge polygons in permafrost. Special GSA Papers, No. 70, New York.

Lachenbruch, A. H. 1963. Contraction theory of ice-wedge polygons: A qualitative discussion, PERMAFROST, Proceedings International Conference, National Academy of Sciences - National Research Council, Washington, D.C., Publication No. 1287.

Ladanyi, B. 1972. An engineering theory of creep of frozen soils, Canadian Geotechnical Journal, Vol. 9, pp. 63-80.

Lunardini, J. Virgil. 1981. HEAT TRANSFER IN COLD CLIMATES. Van Nostrand Reinhold Company, New York.

Lutton, R. J. 1982. Evaluation Cover Systems for Solid and Hazardous Waste. U.S. Environmental Protection Agency, Cincinnati, Ohio, Report SW-867.

Lutton, R. J.; Regan, G. L.; and Jones, L. W. 1979. Design and Construction of Covers for Sold Waste Land Fills. U.S. Environmental Protection Agency, Cincinnati, Ohio, Report EPA-600/2-79-165.

Muskhelishvili, N. I. 1963. SOME BASIC PROBLEMS OF THE MATHEMATICAL THEORY OF ELASTICITY. P. Noordhoff, Groningen, Holland.

Nady, R. M. 1972. Discussion to a study of transverse cracking of bituminous pavements. Proc. Assoc. Asphalt Paving Tech. Vol. 41, p. 424.

NAVFAC. 1982. Design Manual DM 7.2: Foundations and Earth structures, Department of the Navy, Naval Facilities Engineering Command, Alexandria, Va.

NCHRP Synthesis 26, 1974. ROADWAY DESIGN IN SEASONAL FROST AREAS, Transportation Research Board, National Research Council, Washington, D.C.

Paris, Paul C.; and Sih, George C. 1964. Stress analysis of cracks. Fracture Toughness Testing and Its Application, American Society for Testing and Materials, Special Technical Publication, No. 381.

Pounder, E. R. 1967. THE PHYSICS OF ICE. Pergamon Press, Oxford, England.

Roethlisberger, Hans. 1972. Seismic exploration in cold regions. U.S. Army Cold Regions Research and Engineering Laboratory, Hanover, New Hampshire, CRREL, Monograph II-A2a.

Sayles, Francis H. 1973. Triaxial and creep tests on frozen Ottawa sand, North Am. Contrib. 2nd Int. Conf. Permafrost, Yakutsk, U.S.S.R., National Academy of Sciences, Washington.

Sneddon, I. N. 1946. The distribution of stress in the neighbourhood of a crack in an elastic solid. Proceedings of the Royal Society of London, Series A., Vol. 187, pp. 229-260.

Sih, C. G. 1973. HANDBOOK OF STRESS-INTENSITY FACTORS. Institute of Fracture and Solid Mechanics, Lehigh University, Bethlehem, Pennsylvania

Terzaghi, K. 1952. Permafrost. J. of the Boston Society of Civil Engineers, Vol. 39, No. 1, Jan. 1952, pp. 1-40.

Timoshenko, S. P.; and Goodier, J. N. 1970. THEORY OF ELASTICITY. McGraw-Hill Book Co., New York.

Tsytovich, N. A. 1975. THE MECHANICS OF FROZEN GROUND. McGraw-Hill Book Co., New York.

Vyalov, S. S. 1986. REHOLOGIAL FUNDAMENTALS OF SOIL MECHANICS. Translated from the Russian by O. K. Sapunov, Elsevier, New York.

Yoder, E. J.; and Witczak, M. W. 1975. PRINCIPLES OF PAVEMENT DESIGN, 2nd Ed., John Wiley and Sons, Inc., New York.

Yuanlin, Zhu;, and Carbee, David. 1987. Tensile strength of frozen silt. U.S. Army Cold Regions Research and Engineering Laboratory. Hanover, New Hampshire, CRREL, REPORT 87-15, pp. 1-23.

APPENDIX - DATA

A. Thermal Contraction Measurements

B. Fiber Reinforcement Tests.

C. Thermal Tensile and Stress Relaxation Tests.

D. Temperature Data, Fargo, ND.

Table A-1: Thermal Contraction Measurements.

SAMPLE NO. 1

Type of Sand = Ottawa Sand
Water Content % = 21.6
Degree of Saturation = 100%
Density = 2.257 g/cm^3
Test Duration = 36 hr.

Temperature (°C)	Coefficient of Thermal Contraction x 10^6 (°C^{-1})
-4.95	34.25
-7.45	31.86
-15.05	28.06
-17.17	27.77
-20.18	28.26
-23.47	26.18

SAMPLE NO. 2

Type of Sand = Ottawa Sand
Water Content % = 14.46
Degree of Saturation = 75.13%
Density = 2.13 g/cm^3
Test Duration = 36 hr.

Temperature (°C)	Coefficient of Thermal Contraction x 10^6 (°C^{-1})
-5.80	28.21
-16.09	23.37
-18.94	22.21
-25.97	21.44

SAMPLE NO. 3

Type of Sand = Ottawa Sand
Water Content % = 11.34
Degree of Saturation = 60.12%
Density = 1.96 g/cm^3
Test Duration = 36 hr.

Temperature (°C)	Coefficient of Thermal Contraction x 10^6 (°C^{-1})
-8.63	19.57
-12.7	19.87

SAMPLE NO. 3 (cont'd.)

-15.43	22.18
-17.43	22.83
-20.65	20.85
-23.47	20.25

SAMPLE NO. 4

Type = Ice, form from distilled water
Density = 0.916
Test Duration = 36 hr.

Temperature (°C)	Coefficient of Thermal Contraction x 10^6 (°C^{-1})
-6.45	58.70
-14.14	57.56
-16.29	56.51
-17.99	57.42
-21.78	55.39
-25.00	54.99

SAMPLE NO. 5

Type = Snow
Density = 0.846 g/cm^3
Test Duration = 36 hr.

Temperature (°C)	Coefficient of Thermal Contraction x 10^6 (°C^{-1})
-7.55	55.25
-14.35	53.12
-17.26	55.65
-18.77	54.29
-20.44	52.87
-24.03	51.70

SAMPLE NO. 6

Type = Snow
Density = 0.856 g/cm^3
Test Duration = 36 hr.

Table A-1 (cont'd.)

SAMPLE NO. 6 (cont'd.)

Temperature (°C)	Coefficient of Thermal Contraction x 10^6 (°C^{-1})
-10.36	56.42
-12.66	55.21
-13.83	51.03
-14.52	55.73
-16.27	52.40
-20.53	54.48
-23.83	53.57

Table A-2: Sieve Analysis for Ottawa Sand Used to Measure the Coefficient of Thermal Contraction.

U.S. Standard Sieve Number	Percent Finer by Weight
30	99.80
40	47.80
50	8.20
70	1.50
100	0.32
140	0.10
200	0.04
Pan	0.00

Table B-1: Fiber Reinforcement Tests

SAMPLE NO. 1

Data Invalid -

SAMPLE NO. 2

Type of the Fiber = Steel Wire Gage 28
Fiber Diameter = 0.016"
Fiber Length = 0.250"
Temperature = -6.2 °C
Nom. Strain Rate = 1.11 x 10^{-4} sec^{-1}
Ave. Strain Rate = 1.65 x 10^{-4} sec^{-1}
Sample Diameter = 1.13"
Initial Length = 2.260"
Final Length = 2.157"
Percent Sand (by Vol.) = 61
Percent Fiber (by Vol.) = 3
Percent Ice (by Vol.) = 36
Time to Failure = 275 sec

Strain (%)	Stress (psi)
0.0	0
1.27	209
1.45	380
1.63	578
1.91	746
2.09	897
2.36	997
2.73	1067
3.09	1128
3.37	1176
3.73	1216
4.00	1246
4.55	1261
4.73	1259
5.10	1255
5.46	1241
5.83	1222
6.19	1199
6.55	1185
6.74	1173

SAMPLE NO. 3

Data Invalid - Membrane Leak

SAMPLE NO. 4

Type of the Fiber = Steel Wire Gage 28

SAMPLE NO. 4 (cont'd.)

Fiber Diameter = 0.016"
Fiber Length = 0.250"
Temperature = -6.1 °C
Nom. Strain Rate = 1.11 x 10^{-4} sec^{-1}
Ave. Strain Rate = 0.87 x 10^{-4} sec^{-1}
Sample Diameter = 1.13"
Initial Length = 2.26"
Final Length = 1.92"
Percent Sand (by Vol.) = 55
Percent Fiber (by Vol.) = 9
Percent Ice (by Vol.) = 36
Time to Failure = 837 sec.

Strain (%)	Stress (psi)
0.0	0
0.096	4
0.096	4
0.096	8
0.288	184
0.480	287
0.865	559
1.154	852
1.346	1020
1.442	1147
1.731	1220
1.923	1268
2.116	1316
2.308	1351
2.404	1384
2.597	1406
2.789	1429
3.078	1454
3.366	1466
3.559	1484
3.751	1502
3.943	1515
4.136	1533
4.426	1553
4.617	1566
4.809	1592
5.098	1603
5.290	1616
5.482	1629
5.675	1642
5.693	1658
6.156	1670
6.348	1675
6.540	1684
6.733	1688

Table B-1 (cont'd.)

SAMPLE NO. 4 (cont'd.)

6.925	1693
7.118	1696
7.310	1698
7.502	1698
7.791	1693
7.983	1689
8.176	1686

SAMPLE NO. 5

Type of the Fiber = Steel Wire
Gage 24
Fiber Diameter = 0.23"
Fiber Length = 0.25"
Temperature = -6.1 °C
Nom. Strain Rate = 1.11 x 10^{-4} sec^{-1}
Ave. Strain Rate = 1.26 x 10^{-4} sec^{-1}
Sample Diameter = 1.13"
Initial Length = 2.260"
Final Length = 2.099"
Percent Sand (by Vol.) = 55
Percent Fiber (by Vol.) = 9
Percent Ice (by Vol.) = 36
Time to Failure = 562 sec.

Strain (%)	Stress psi)
0.0	0
0.192	124
0.577	257
0.769	413
0.961	614
1.154	796
1.442	947
1.635	1060
1.923	1137
2.308	1187
2.693	1229
3.174	1260
3.559	1288
4.136	1359
5.290	1359
5.770	1377
6.156	1387
6.637	1392
7.118	1389
7.406	1389
7.695	1380
8.080	1367
9.040	1313

SAMPLE NO.5 (cont'd.)

9.522	1271
10.100	1220

SAMPLE NO. 6

Type of the Fiber = Steel Wire
Gage 17
Fiber Diameter = 0.054"
Fiber Length = 0.25"
Temperature = -6.1 °C
Nom. Strain Rate = 1.11 x 10^{-4} sec^{-1}
Ave. Strain Rate = 1.51 x 10^{-4} sec^{-1}
Sample Diameter = 1.13"
Initial Length = 2.26"
Final Length = 2.14"
Percent Sand (by Vol.) = 55
Percent Fiber (by Vol.) = 9
Percent Ice (by Vol.) = 36
Time to Failure = 350 sec.

Strain (%)	Stress (psi)
0.0	0
0.384	17
0.577	111
0.769	202
0.961	337
1.154	532
1.346	820
1.539	1031
1.827	1134
2.212	1167
2.597	1192
2.981	1225
3.462	1252
3.847	1268
4.136	1281
4.617	1282
5.001	1285
5.194	1291
5.290	1286
6.159	1246
6.925	1167
7.887	1048

SAMPLE NO. 7

Type of the Fiber = Steel Wire
Gage 17
Fiber Diameter = 0.054"
Fiber Length = 0.25"

Table B-1 (cont'd.)

SAMPLE NO. 7 (Cont'd.)

Temperature = -6.0 °C
Nom. Strain Rate = 1.11 x 10^{-4} sec^{-1}
Ave. Strain Rate = 1.42 x 10^{-4} sec^{-1}
Sample Diameter = 1.13"
Initial Length = 2.260"
Final Length = 2.146"
Percent Sand (by Vol.) = 61
Percent Fiber (by Vol.) = 3
Percent Ice (by Vol.) = 36
Time to Failure = 350 sec.

Strain (%)	Stress (psi)
0.0	0
0.096	305
0.288	541
0.480	703
0.769	842
1.058	955
1.250	1047
1.635	1098
2.116	1147
2.500	1189
3.078	1220
3.462	1252
3.943	1283
4.328	1303
4.809	1304
5.001	1314
5.290	1302
6.252	1228
7.502	1020
8.176	898

SAMPLE NO. 8

Data Invalid - Membrane Leak

SAMPLE NO. 9

Type of the Fiber = Steel Wire Gage 17
Fiber Diameter = 0.054"
Fiber Length = 0.25"
Temperature = -6.1 °C
Nom. Strain Rate = 1.11 x 10^{-4} sec^{-1}
Ave. Strain Rate = 1.38 x 10^{-4} sec^{-1}
Sample Diameter = 1.13"
Initial Length = 2.26"
Final Length = 2.14"
Percent Sand (by Vol.) = 55

SAMPLE NO. 9 (cont'd.)

Percent Fiber (by Vol.) = 9
Percent Ice (by Vol.) = 36
Time to Failure = 369 sec.

Strain (%)	Stress (psi)
0.0	0
0.096	137
0.192	245
0.480	441
0.673	663
0.961	819
1.154	946
1.539	1056
2.020	1119
2.404	1157
2.693	1191
3.078	1220
3.559	1251
3.943	1279
4.328	1290
4.809	1296
5.098	1296
5.482	1291
5.867	1282
6.444	1250
6.733	1230
7.502	1156
8.464	1049
9.138	959
9.619	888
10.58	767

SAMPLE NO. 10

Type of the Fiber = Steel Wire Gage 17
Fiber Diameter = 0.054"
Fiber Length = 0.25"
Temperature = -6.1 °C
Nom. Strain Rate = 1.11 x 10^{-4} sec^{-1}
Ave. Strain Rate = 1.44 x 10^{-4} sec^{-1}
Sample Diameter = 1.13"
Initial Length = 2.26"
Final Length = 2.12"
Percent Sand (by Vol.) = 58
Percent Fiber (by Vol.) = 6
Percent Ice (by Vol.) = 36
Time to Failure = 413 sec.

Table B-1 (cont'd.)

SAMPLE NO. 10 (cont'd.)

Strain (%)	Stress (psi)
0.0	0
0.0	198
0.192	387
0.577	578
0.865	777
1.250	919
1.539	1014
1.923	1086
2.212	1142
2.693	1203
2.981	1242
3.462	1290
3.943	1325
4.232	1354
4.617	1385
5.098	1407
5.290	1420
5.675	1427
5.963	1431
6.252	1430
7.310	1370
7.791	1327
8.272	1249
8.657	1189
10.003	1000

SAMPLE NO. 11

Type of the Fiber = Steel Wire Gage 17
Fiber Diameter = 0.054"
Fiber Length = 0.5"
Temperature = -6.0 °C
Nom. Strain Rate = 1.11×10^{-4} sec^{-1}
Ave. Strain Rate = 1.42×10^{-4} sec^{-1}
Sample Diameter = 1.13"
Initial Length = 2.26"
Final Length = 2.11"
Percent Sand (by Vol.) = 55
Percent Fiber (by Vol.) = 9
Percent Ice (by Vol.) = 36
Time to Failure = 444 sec.

Strain (%)	Stress (psi)
0.0	0
0.96	133

SAMPLE NO. 11 (cont'd.)

0.384	240
0.673	406
0.961	559
1.154	707
1.539	831
1.923	980
2.404	1102
2.789	1198
3.270	1271
3.655	1324
4.136	1380
4.520	1420
4.905	1459
5.290	1494
5.579	1510
5.963	1536
6.348	1546
6.637	1545
6.925	1540
7.214	1519
7.599	1489
8.080	1418
8.849	1288
9.522	1150
9.907	1064
10.388	958
11.254	807

SAMPLE NO. 12

Type of the Fiber = Steel Wire Gage 17
Fiber Diameter = 0.054"
Fiber Length = 0.5"
Temperature = -6.1 °C
Nom. Strain Rate = 1.11×10^{-4} sec^{-1}
Ave. Strain Rate = 1.43×10^{-4} sec^{-1}
Sample Diameter = 1.13"
Initial Length = 2.26"
Final Length = 2.11"
Percent Sand (by Vol.) = 58
Percent Fiber (by Vol.) = 6
Percent Ice (by Vol.) = 36
Time to Failure = 463 sec.

Strain (%)	Stress (psi)
0.0	0
0.096	111
0.384	201

Table B-1 (cont'd.)

SAMPLE NO. 12 (cont'd.)

0.673	278
0.961	448
1.154	605
1.346	757
1.635	915
1.827	1041
2.212	1163
2.597	1221
2.885	1264
3.270	1305
3.655	1341
3.993	1374
4.328	1406
4.617	1439
4.905	1463
5.194	1491
5.482	1511
5.771	1527
6.060	1538
6.348	1542
6.637	1545
6.829	1538
7.118	1529
7.406	1516
7.599	1501
8.080	1450
8.272	1427
8.657	1370
9.234	1275
9.619	1207
10.196	1114

SAMPLE NO. 13

Type of the Fiber = Steel Wire Gage 17
Fiber Diameter = 0.054"
Fiber Length = 0.5"
Temperature = -6.1 °C
Nom. Strain Rate = 1.11 x 10^{-4} sec^{-1}
Ave. Strain Rate = 1.30 x 10^{-4} sec^{-1}
Sample Diameter = 1.13"
Initial Length = 2.26"
Final Length = 2.12"
Percent Sand (by Vol.) = 61
Percent Fiber (by Vol.) = 3
Percent Ice (by Vol.) = 36
Time to Failure = 450 sec.

SAMPLE NO. 13 (cont'd.)

Strain (%)	Stress (psi)
0.0	0
0.096	137
0.288	232
0.577	334
0.865	440
1.154	600
1.731	711
1.827	918
1.923	997
2.212	1087
2.404	1182
2.693	1250
2.981	1309
3.270	1363
3.559	1409
3.847	1450
4.040	1485
4.328	1517
4.713	1556
4.905	1586
5.194	1606
5.386	1615
5.867	1619
5.963	1617
6.540	1607
7.052	1587
7.599	1354

SAMPLE NO. 14

Type of the Fiber = Sand only
Temperature = -6.1 °C
Nom. Strain Rate = 1.11 x 10^{-4} sec^{-1}
Ave. Strain Rate = 1.48 x 10^{-4} sec^{-1}
Sample Diameter = 1.13"
Initial Length = 2.26"
Final Length = 2.13"
Percent Sand (by Vol.) = 64
Percent Fiber (by Vol.) = 0
Percent Ice (by Vol.) = 36
Time to Failure = 362 sec.

Strain (%)	Stress (psi)
0.0	0
0.096	99
0.288	189

Table B-1 (cont'd.)

SAMPLE NO. 14 (cont'd.)

0.577	317
0.867	547
1.154	801
1.539	1031
1.923	1217
2.308	1263
2.789	1315
3.174	1344
3.559	1384
4.040	1414
4.424	1433
4.905	1451
5.386	1464
5.482	1458
5.771	1454
6.060	1441
6.540	1402
7.021	1346
7.695	1265
7.983	1217
8.272	1162
9.428	1104

SAMPLE NO. 15

Data Invalid - Tilted in the Loading Cups

SAMPLE NO. 16

Type of the Fiber = Sand only
Temperature = -6.0 °C
Nom. Strain Rate = 1.11 x 10^{-4} sec^{-1}
Ave. Strain Rate = 1.44 x 10^{-4} sec^{-1}
Sample Diameter = 1.13"
Initial Length = 2.26"
Final Length = 2.12"
Percent Sand (by Vol.) = 64
Percent Fiber (by Vol.) = 0
Percent Ice (by Vol.) = 36
Time to Failure = 418 sec.

Strain (%)	Stress (psi)
0.0	0
0.096	77
0.384	107
0.673	115
1.154	153
1.442	335
1.731	495

SAMPLE NO. 16 (cont'd.)

2.020	650
2.308	779
2.500	924
2.693	1057
3.174	1193
3.559	1279
3.847	1313
4.328	1348
4.713	1376
5.001	1392
5.290	1408
5.579	1416
5.867	1420
6.060	1421
6.156	1415
6.444	1407
6.829	1389
7.502	1331
7.887	1298
8.176	1266

SAMPLE NO. 17

Type of the Fiber = Steel Wire Gage 28
Fiber Diameter = 0.016"
Fiber Length = 0.25"
Temperature = -6.05 °C
Nom. Strain Rate = 1.11 x 10^{-4} sec^{-1}
Ave. Strain Rate = 1.45 x 10^{-4} sec^{-1}
Sample Diameter = 1.13"
Initial Length = 2.26"
Final Length = 2.11"
Percent Sand (by Vol.) = 58
Percent Fiber (by Vol.) = 6
Percent Ice (by Vol.) = 36
Time to Failure = 437 sec.

Strain (%)	Stress (psi)
0.0	0
0.096	193
0.288	318
0.577	458
0.865	658
1.154	822
1.442	968
1.731	1105
2.020	1216
2.308	1280

Table B-1 (cont'd.)

SAMPLE 17 (cont'd.)

2.789	1324
3.078	1353
3.462	1373
3.751	1389
4.232	1420
4.520	1436
4.809	1452
5.098	1460
5.386	1472
5.675	1480
5.963	1483
6.252	1483
6.348	1485
6.444	1484
6.637	1481
7.118	1469
7.599	1455
7.887	1425
8.464	1385

SAMPLE NO. 18

Type of the Fiber = Steel Wire Gage 24
Fiber Diameter = 0.023"
Fiber Length = 0.25"
Temperature = -6.0 °C
Nom. Strain Rate = $1.11 \times 10^{-4} sec^{-1}$
Ave. Strain Rate = $1.35 \times 10^{-4} sec^{-1}$
Sample Diameter = 1.13"
Initial Length = 2.26"
Final Length = 2.14"
Percent Sand (by Vol.) = 61
Percent Fiber (by Vol.) = 3
Percent Ice (by Vol.) = 36
Time to Failure = 368

Strain (%)	Stress (psi)
0.0	0
0.096	198
0.384	352
0.577	552
0.865	760
1.154	954
1.346	1097
1.635	1212
1.923	1285
2.212	1323
2.597	1373

SAMPLE NO. 18 (cont'd.)

2.885	1402
3.270	1430
3.559	1455
3.751	1481
4.040	1501
4.328	1517
4.617	1533
5.001	1543
5.098	1542
5.579	1530
6.060	1494
6.733	1415
7.118	1357
7.695	1269
8.080	1212
8.176	1203

SAMPLE NO. 19

Type of the Fiber = Steel Wire Gage 28
Fiber Diameter = 0.016"
Fiber Length = 0.25"
Temperature = -6.05 °C
Nom. Strain Rate = $1.11 \times 10^{-4} sec^{-1}$
Ave. Strain Rate = $1.36 \times 10^{-4} sec^{-1}$
Sample Diameter = 1.13"
Initial Length = 2.26"
Final Length = 2.13"
Percent Sand (by Vol.) = 61
Percent Fiber (by Vol.) = 3
Percent Ice (by Vol.) = 36
Time to Failure = 394 sec.

Strain (%)	Stress (psi)
0.0	0
0.096	142
0.288	245
0.673	441
0.865	636
1.154	839
1.346	1029
1.635	1225
1.923	1302
2.212	1353
2.597	1381
2.885	1406
3.174	1431
3.559	1463

Table B-1 cont'd.

SAMPLE NO. 19 (cont'd.)

3.943	1499
4.232	1523
4.520	1543
4.809	1555
5.001	1568
5.290	1571
5.386	1574
5.482	1572
5.771	1563
5.963	1548
6.252	1527
6.540	1506
7.310	1402
7.983	1316
8.176	1274

SAMPLE NO. 20

Type of the Fiber = Steel Wire Gage 24
Fiber Diameter = 0.023"
Fiber Length = 0.25"
Temperature = -6.05 °C
Nom. Strain Rate = $1.11 \times 10^{-4} sec^{-1}$
Ave. Strain Rate = $1.33 \times 10^{-4} sec^{-1}$
Sample Diameter = 1.13"
Initial Length = 2.26"
Final Length = 2.11"
Percent Sand (by Vol.) = 58
Percent Fiber (by Vol.) = 6
Percent Ice (by Vol.) = 36
Time to Failure = 475 sec.

Strain (%)	Stress (psi)
0.0	0
0.096	189
0.288	318
0.673	496
0.961	725
1.250	868
1.539	997
1.827	1096
2.116	1177
2.404	1236
2.693	1287
3.078	1328
3.366	1358
3.655	1383
4.040	1410

SAMPLE NO. 20 (cont'd.)

4.328	1431
4.617	1455
4.905	1475
5.194	1495
5.386	1513
5.675	1520
6.060	1530
6.348	1542
6.540	1535
6.829	1530
7.021	1519
7.310	1506
7.502	1491
8.080	1442

SAMPLE NO. 21

Type of the Fiber = Steel Wire Gage 24
Fiber Diameter = 0.023"
Fiber Length = 0.5"
Temperature = -6.0 °C
Nom. Strain Rate = $1.11 \times 10^{-4} sec^{-1}$
Ave. Strain Rate = $1.29 \times 10^{-4} sec^{-1}$
Sample Diameter = 1.13"
Initial Length = 2.26"
Final Length = 2.13"
Percent Sand (by Vol.) = 61
Percent Fiber (by Vol.) = 3
Percent Ice (by Vol.) = 36
Time to Failure = 437

Strain (%)	Stress (psi)
0.0	0
0.096	17
0.577	214
0.673	534
0.865	756
1.058	946
1.346	1067
1.635	1115
1.923	1128
2.212	1138
2.500	1147
2.789	1169
3.078	1190
3.366	1212
3.655	1229
3.943	1250

Table B-1 (cont'd.)

SAMPLE NO. 21 (cont'd.)

4.136	1276
4.424	1301
4.713	1322
4.905	1340
5.194	1352
5.482	1360
5.675	1366
5.771	1364
6.156	1359
6.829	1345
7.021	1290
7.599	1218
7.887	1183
8.080	1161

SAMPLE NO. 22

Type of the Fiber = Steel Wire Gage 17
Fiber Diameter = 0.023"
Fiber Length = 0.5"
Temperature = -6.0 °C
Nom. Strain Rate = $1.11 \times 10^{-4} sec^{-1}$
Ave. Strain Rate = $1.29 \times 10^{-4} sec^{-1}$
Sample Diameter = 1.13"
Initial Length = 2.26"
Final Length = 2.09"
Percent Sand (by Vol.) = 55"
Percent Fiber (by Vol.) = 9
Percent Ice (by Vol.) = 36
Time to Failure = 550 sec.

Strain (%)	Stress (psi)
0.0	0
0.096	215
0.288	373
0.480	557
0.769	804
1.250	1085
1.539	1158
1.827	1201
2.116	1223
2.404	1236
2.693	1250
2.981	1267
3.270	1280
3.559	1297
3.751	1315
4.136	1338

SAMPLE NO. 22 (cont'd.)

4.424	1355
4.713	1367
5.098	1390
5.482	1401
5.771	1413
5.963	1418
6.156	1424
6.444	1427
6.737	1431
7.118	1425
7.790	1411

SAMPLE NO. 23

Data Invalid - Membrane Leak

SAMPLE NO. 24

Type of the Fiber = Steel Wire Gage 17
Fiber Diameter = 0.054"
Fiber Length = 0.25"
Temperature = -6.1 °C
Nom. Strain Rate = $1.11 \times 10^{-4} sec^{-1}$
Ave. Strain Rate = $1.31 \times 10^{-4} sec^{-1}$
Sample Diameter = 1.13"
Initial Length = 2.26"
Final Length = 2.13"
Percent Sand (by Vol.) = 55
Percent Fiber (by Vol.) = 9
Percent Ice (by Vol.) = 36
Time to Failure = 431 sec.

Strain (%)	Stress (psi)
0.0	0
0.192	181
0.480	296
0.673	423
0.961	555
1.250	689
1.442	811
1.731	940
2.020	1034
2.597	1192
2.885	1243
3.174	1285
3.366	1324
3.655	1358
3.943	1383
4.136	1413

Table B-1 (cont'd.)

SAMPLE NO. 24 (cont'd.)

4.424	1437
4.713	1458
4.905	1475
5.194	1487
5.386	1500
5.579	1506
5.675	1508
5.771	1507
5.867	1505
6.060	1498
6.156	1500
6.540	1466
6.925	1424
7.118	1389
8.560	1064

SAMPLE NO. 25

Type of the Fiber = Steel Wire Gage 24
Fiber Diameter = 0.023"
Fiber Length = 0.25"
Temperature = -6.0 °C
Nom. Strain Rate = $1.11 \times 10^{-4} sec^{-1}$
Ave. Strain Rate = $1.49 \times 10^{-4} sec^{-1}$
Sample Diameter = 1.13"
Initial Length = 2.26"
Final Length = 2.10"
Percent Sand (by Vol.) = 55
Percent Fiber (by Vol.) = 9
Percent Ice (by Vol.) = 36
Time to Failure = 462

Strain (%)	Stress (psi)
0.0	0
0.192	116
0.480	188
0.769	286
1.058	396
1.345	531
1.635	665
1.923	799
2.212	914
2.500	1021
2.789	1102
3.174	1164
3.462	1206
3.751	1248
4.040	1282

SAMPLE NO. 25 (cont'd.)

4.328	1315
4.617	1344
4.905	1369
5.194	1389
5.480	1409
5.771	1425
5.963	1439
6.252	1450
6.540	1454
6.925	1456
7.021	1450
7.118	1449
7.695	1432
8.178	1405

SAMPLE NO. 26

Type of the Fiber = Steel Wire Gage 28
Fiber Diameter = 0.016"
Fiber Length = 0.25"
Temperature = -6.0 °C
Nom. Strain Rate = $1.11 \times 10^{-4} sec^{-1}$
Ave. Strain Rate = $1.36 \times 10^{-4} sec^{-1}$
Sample Diameter = 1.13"
Initial Length = 2.26"
Final Length = 2.12"
Percent Sand (by Vol.) = 58
Percent Fiber (by Vol.) = 6
Percent Ice (by Vol.) = 36
Time to Failure = 450 sec.

Strain (%)	Stress (psi)
0.0	0
0.096	116
0.384	190
0.577	304
0.865	440
1.058	592
1.346	748
1.635	894
1.923	1002
2.116	1092
2.500	1164
2.789	1219
3.078	1270
3.366	1308
3.655	1345
3.943	1383

Table B-1 cont'd.

SAMPLE NO. 26 (cont'd.)

4.232	1416
4.520	1440
4.809	1464
5.098	1481
5.386	1496
5.579	1514
5.771	1523
6.060	1526
6.156	1533
6.252	1531
6.540	1518
7.214	1487
7.599	1449
7.983	1396
8.176	1365

SAMPLE NO. 27

Type of the Fiber = Steel Wire Gage 24
Fiber Diameter = 0.023"
Fiber Length = 0.5"
Temperature = -6.0 °C
Nom. Strain Rate = 1.11 x 10^{-4} sec^{-1}
Ave. Strain Rate = 1.29 x 10^{-4} sec^{-1}
Sample Diameter = 1.13"
Initial Length = 2.26"
Final Length = 2.04"
Percent Sand (by Vol.) = 55
Percent Fiber (by Vol.) = 9
Percent Ice (by Vol.) = 36
Time to Failure = 744 sec.

Strain (%)	Stress (psi)
0.0	0
0.192	137
0.673	252
1.154	417
1.635	644
2.212	918
2.597	1112
3.174	1248
3.655	1337
4.136	1409
4.520	1477
5.001	1531
5.482	1585
5.867	1635
6.252	1685

SAMPLE NO. 27 (cont'd.)

6.637	1730
7.021	1767
7.406	1808
7.695	1838
8.080	1862
8.464	1878
8.753	1892
9.138	1895
9.426	1901
9.619	1901
9.715	1899
10.677	1856
11.158	1823

SAMPLE NO. 28

Data Invalid - Membrane Leak

SAMPLE NO. 29

Data Invalid - Membrane Leak

SAMPLE NO. 30

Type of the Fiber = Steel Wire Gage 28
Fiber Diameter = 0.016"
Fiber Length = 0.5"
Temperature = -6.1 °C
Nom. Strain Rate = 1.11 x 10^{-4} sec^{-1}
Ave. Strain Rate = 1.09 x 10^{-4} sec^{-1}
Sample Diameter = 1.13"
Initial Length = 2.26"
Final Length = 2.13"
Percent Sand (by Vol.) = 61
Percent Fiber (by Vol.) = 3
Percent Ice (by Vol.) = 36
Time to Failure = 519 sec.

Strain (%)	Stress (psi)
0.0	0
0.096	94
0.384	157
0.673	244
0.961	345
1.250	464
1.539	589
1.731	720
2.020	844
2.308	951

Table B-1 (cont'd.)

SAMPLE NO. 30 (cont'd.)

2.500	1025
2.789	1089
3.078	1144
3.366	1195
3.559	1226
3.847	1260
4.040	1294
4.328	1319
4.520	1341
4.809	1362
5.001	1380
5.194	1397
5.482	1409
5.675	1419
5.771	1417
5.963	1414
6.060	1413
6.540	1394
7.406	1305

SAMPLE NO. 31 (cont'd.)

3.943	1519
4.328	1542
4.713	1565
5.098	1587
5.579	1594
5.963	1617
6.348	1622
6.637	1634
6.925	1641
7.214	1651
7.599	1653
7.983	1658
8.176	1658
8.272	1656
8.752	1652
9.041	1644
9.330	1641
9.522	1638
9.715	1630

SAMPLE NO. 31

Type of the Fiber = Steel Wire Gage 28
Fiber Diameter = 0.016"
Fiber Length = 0.5"
Temperature = -6.0 °C
Nom. Strain Rate = 1.11 x 10^{-4} sec^{-1}
Ave. Strain Rate = 1.59 x 10^{-4} sec^{-1}
Sample Diameter = 1.13"
Initial Length = 2.26"
Final Length = 2.07"
Percent Sand (by Vol.) = 58
Percent Fiber (by Vol.) = 6
Percent Ice (by Vol.) = 36
Time to Failure = 513 sec.

Strain (%)	Stress (psi)
0.0	0
0.192	258
0.384	502
0.673	770
1.154	1005
1.442	1185
1.827	1200
2.308	1360
2.693	1417
3.174	1456
3.559	1488

SAMPLE NO. 32

Type of the Fiber = Steel Wire Gage 28
Fiber Diameter = 0.016"
Fiber Length = 0.5"
Temperature = -6.0 °C
Nom. Strain Rate = 1.11 x 10^{-4} sec^{-1}
Ave. Strain Rate = 1.26 x 10^{-4} sec^{-1}
Sample Diameter = 1.13"
Initial Length = 2.26"
Final Length = 2.04"
Percent Sand (by Vol.) = 55
Percent Fiber (by Vol.) = 9
Percent Ice (by Vol.) = 36
Time to Failure = 769 sec.

Strain (%)	Stress (psi)
0.0	0
0.288	159
0.673	299
1.058	473
1.442	718
1.827	884
2.212	1020
2.597	1137
2.981	1237
3.462	1315
3.847	1363

Table B-1 (cont'd.)

SAMPLE NO. 32 (cont'd.)

4.232	1395
4.617	1414
5.001	1433
5.386	1443
5.675	1463
5.963	1487
6.348	1505
6.733	1523
7.021	1539
7.310	1558
7.695	1567
7.887	1576
8.176	1587
8.464	1594
8.753	1600
9.041	1607
9.330	1610
9.619	1613
9.715	1615
9.811	1613
9.907	1611
10.196	1610
10.386	1610
10.677	1609

SAMPLE NO. 33

Type of the Fiber = Steel Wire Gage 28
Fiber Diameter = 0.016"
Fiber Length = 0.5"
Temperature = -6.1 °C
Nom. Strain Rate = 1.11 x 10^{-4} sec^{-1}
Ave. Strain Rate = 0.80 x 10^{-4} sec^{-1}
Sample Diameter = 1.13"
Initial Length = 2.26"
Final Length = 2.10"
Percent Sand (by Vol.) = 55
Percent Fiber (by Vol.) = 9
Percent Ice (by Vol.) = 36
Time to Failure = 881 sec.

Strain (%)	Stress (psi)
0.0	0
0.096	99
0.288	223
0.480	411
0.673	633
0.961	853

SAMPLE NO. 33 (cont'd.)

1.154	1026
1.442	1151
1.635	1238
1.923	1302
2.212	1365
2.500	1429
2.693	1489
2.981	1551
3.270	1605
3.559	1658
3.751	1709
4.040	1758
4.328	1802
4.520	1839
4.809	1875
5.098	1910
5.386	1937
5.675	1959
6.060	1976
6.252	2000
6.540	2010
6.829	2020
7.118	2022
7.214	2019
7.406	2019
7.983	2003
8.176	1991

SAMPLE NO. 34

Type of the Fiber = Steel Wire Gage 24
Fiber Diameter = 0.023"
Fiber Length = 0.5"
Temperature = -6.1 °C
Nom. Strain Rate = 1.11 x 10^{-4} sec^{-1}
Ave. Strain Rate = 0.85 x 10^{-4} sec^{-1}
Sample Diameter = 1.13"
Initial Length = 2.26"
Final Length = 2.14"
Percent Sand (by Vol.) = 58
Percent Fiber (by Vol.) = 6
Percent Ice (by Vol.) = 36
Time to Failure = 575 sec.

Strain (%)	Stress (psi)
0.0	0
0.096	124
0.288	253

Table B-1 (cont'd.)

SAMPLE NO. 34 (cont'd)	
0.480	416
0.673	603
0.769	817
0.961	1003
1.154	1146
1.442	1236
1.635	1318
1.827	1392
2.020	1457
2.308	1516
2.597	1570
2.885	1624
3.174	1673
3.366	1720
3.559	1758
3.751	1796
4.040	1820
4.232	1841
4.424	1854
4.617	1858
4.905	1861
5.001	1855
5.386	1839
5.771	1795
6.540	1672

Table B-2: Sieve Analysis for Ottawa Sand Used in Fiber Reinforcement Tests.

U.S. Standard Sieve Number	Percent Finer by Weight
30	99.85
40	43.41
50	5.30
70	1.32
100	0.24
140	0.04
200	0.01
Pan	0.00

Table C-1: Thermal Tensile Tests

SAMPLE NO. 1

Initial Diameter = 2.0"
Final Diameter = 2.0"
Rate of Cooling = -0.63 °C/min
Degree of Saturation = 98.71 %
Cooling Agent = Dry Ice
Time to Failure = 182.46 min.
Temperature at which
Failure Occur = -19.5 °C
Maximum Thermal Tensile
Stress = 258.3 psi

Stress (psi)	Temperature (Ave. °C)	Time (min.)
0.0	-9.00	0.00
14.51	-10.40	0.56
34.63	-11.00	1.36
47.27	-11.10	1.70
51.95	-11.50	2.71
54.76	-11.70	3.39
58.04	-11.80	4.60
58.98	-12.00	4.95
64.13	-14.60	5.80
74.42	-14.90	7.51
118.40	-16.10	12.11
149.30	-16.80	25.56
197.07	-18.00	53.46
240.60	-18.20	89.33
258.30	-19.50	182.46

SAMPLE NO. 2

Initial Diameter = 1"
Final Diameter = 1"
Rate of Cooling = -3.01 °C/min
Degree of Saturation = 98.90 %
Cooling Agent = Dry Ice
Time to Failure = 3.96 min.
Temperature at which
Failure Occur = -18.5 °C
Maximum Thermal Tensile
Stress = 211 psi

Stress (psi)	Temperature (Ave. °C)	Time (min.)
0.00	-5.60	0.00
33.62	-6.50	0.00
46.77	-8.25	0.70
59.77	-9.75	1.38
89.66	-11.60	1.93
121.40	-13.40	2.55

SAMPLE NO. 2 (cont'd.)

175.50	-16.50	3.36
184.90	-17.60	3.70
211.00	-18.50	3.96

SAMPLE NO. 3

Initial Diameter = 1"
Final Diameter = 1"
Rate of Cooling = -4.31 °C/min
Degree of Saturation = 98.50 %
Cooling Agent = Dry Ice
Time to Failure = 1.86 min
Temperature at which
Failure Occur = -13.4 °C
Maximum Thermal Tensile
Stress = 138.5 psi

Stress (psi)	Temperature (Ave. °C)	Time (min.)
0.00	-5.3	0.00
71.15	-6.5	0.216
74.89	-7.0	0.316
84.25	-7.6	0.416
89.87	-7.8	0.516
99.23	-8.7	0.633
102.98	-9.7	0.833
106.72	-10.2	0.933
108.59	-11.0	1.150
127.30	-12.3	1.560
131.00	-12.7	1.660
132.94	-13.0	1.760
138.50	-13.4	1.860

SAMPLE NO. 4

Initial Diameter = 2"
Final Diameter = 2"
Rate of Cooling = -0.422 °C/min
Degree of Saturation = 98.31 %
Cooling Agent = Dry Ice
Time to Failure = 152.19 min.
Temperature at which
Failure Occur = -66.9 °C
Maximum Thermal Tensile
Stress = 490.8 psi

Stress (psi)	Temperature (Ave. °C)	Time (min.)
0.00	-3.45	0.00
14.94	-3.60	0.85

Table C-1 (cont'd.)

SAMPLE NO. 4 (cont'd.)

22.88	-3.65	1.48
19.61	-3.30	2.11
18.21	-3.00	2.74
19.14	-2.40	3.47
15.41	-2.00	4.37
13.54	-3.30	4.98
14.00	-9.50	5.61
22.88	-14.00	6.24
30.82	-17.50	6.97
40.62	-22.50	7.58
51.83	-28.00	8.21
62.10	-28.50	8.84
70.50	-29.50	9.45
79.85	-30.00	10.18
87.79	-30.50	10.81
95.26	-31.00	11.42
101.80	-31.50	12.05
108.80	-31.75	12.68
116.28	-32.25	13.29
124.68	-33.50	14.02
134.02	-33.50	14.46
141.03	-33.50	15.07
148.96	-33.50	15.70
156.44	-34.25	16.31
164.38	-34.50	17.04
169.98	-35.50	17.65
175.12	-36.00	18.28
180.25	-36.50	18.89
186.32	-36.75	19.52
190.53	-37.50	20.25
191.93	-38.00	20.86
193.80	-39.00	21.55
193.33	-39.25	22.33
247.50	-47.50	39.78
323.62	-51.00	69.78
374.99	-58.00	84.78
413.75	-61.25	99.78
450.64	-64.50	119.78
482.86	-66.25	144.78
488.93	-66.80	149.78
490.80	-66.90	152.19

SAMPLE NO. 5

Initial Diameter = 2"
Final Diameter = 2"
Rate of Cooling = -0.021 °C/min
Degree of Saturation = 98.1 %
Cooling Agent = Freezer
Time to Failure = 465 min.

SAMPLE NO. 5 (cont'd.)

Temperature at which
Failure Occur = -15.05 °C
Maximum Thermal Tensile
Stress = 77.05 psi

Stress (psi)	Temperature (Ave. °C)	Time (min.)
0.00	-5.05	0.00
6.00	-6.05	45.00
7.90	-7.55	120.00
9.80	-8.55	135.00
18.20	-9.45	150.00
21.40	-10.20	165.00
27.50	-11.55	195.00
29.80	-12.05	210.00
43.80	-13.20	255.00
54.10	-14.00	300.00
77.05	-15.05	465.00

Table C-2: Stress Relaxation Tests

SAMPLE NO. 1

Temperature = -15 °C
Degree of Saturation = 98.1 %
Initial Diameter = 2"
Final Diameter = 1.99"
Initial Length = 15.25"
Final Length = 15.286"
No. of Cyclic Strain,
Prior to Failure = 1
Time to Failure = 3.75 min.
Failure Stress = 722.43 psi
Failure Strain = 24.19 x 10^{-4} in/in

Stress (psi)	Strain x 10^4 (in/in)	Time (min.)
116.28	0.000	0.000
171.38	1.612	0.250
220.88	3.225	0.480
259.69	4.838	0.730
396.47	8.064	1.100
454.38	8.064	1.333
461.85	12.904	1.583
506.68	12.900	1.816
580.00	14.510	2.186
598.68	17.740	2.780
641.64	19.350	3.150
644.44	19.350	3.260
722.43	24.190	3.750

SAMPLE NO. 2

Temperature = -15 °C
Degree of Saturation = 98.51 %
Initial Diameter = 2"
Final Diameter = 1.95"
Initial Length = 15.250"
Final Length = 15.309"
No. of Cyclic Strain,
Prior to Failure = 2
Time to Failure = 4233.316 min.
Failure Stress = 709.19 psi
Failure Strain = 38.7 x 10^{-4} in/in
Average Cyclic
Strain = 10 x 10^{-4} in/in

Stress (psi)	Strain x 10^4 (in/in)	Time (min.)
0.00	0.00	0.0
84.49	3.20	1.88
159.60	6.40	2.36
217.90	8.00	3.94

SAMPLE NO. 2 (cont'd.)

269.52	9.60	4.30
Cycle No. -1-		
250.84	9.60	4.53
236.82	9.60	6.53
218.14	9.60	12.96
212.53	9.60	16.82
195.72	9.60	38.11
176.07	11.30	98.11
155.99	11.30	458.11
127.40	12.90	1418.11
118.58	14.50	1718.11
116.25	14.50	1838.11
105.51	14.50	2318.11
104.11	14.50	2419.16
Cycle No. -2-		
104.11	14.50	0.00
120.45	14.50	0.133
162.91	16.10	0.245
186.72	16.10	0.361
225.9	17.70	0.611
250.63	17.70	.844
258.06	19.30	1.094
268.79	19.30	1.210
250.43	19.35	1.326
229.59	19.35	2.892
212.79	19.35	11.942
192.26	19.35	43.942
177.79	19.35	93.942
152.13	19.35	393.942
143.26	19.35	693.942
128.79	19.35	993.942
122.73	19.35	1533.942
122.73	19.35	1804.942
End of Cycle No. -2-		
136.73	19.35	1808.142
225.39	19.35	1808.375
337.80	20.96	1808.625
354.08	22.58	1809.108
488.27	25.80	1809.319
534.65	30.64	1811.029
566.40	33.87	1814.040
709.91	38.70	1814.156
Total Time		4233.316

Table C-2 (cont'd.)

SAMPLE NO. 3

Temperature = -15 °C
Degree of Saturation = 98.31 %
Initial Diameter = 2"
Final Diameter = 1.92"
Initial Length = 15.25"
Final Length = 15.323"
No. of Cyclic Strain, Prior to Failure = 4
Time to Failure = 5596.86 min.
Failure Stress = 700.8 psi
Failure Strain = 48.38 x 10^{-4} in/in
Average Cyclic Strain = 10 x 10^{-4} in/in

Stress (psi)	Strain x 10^4 (in/in)	Time (min.)
118.61	0.00	0.00
261.0	8.06	4.86
Cycle No. -1-		
288.60	8.06	4.97
288.60	8.06	4.97
245.16	8.06	5.10
201.73	8.06	5.33
187.26	8.06	5.82
166.71	8.06	6.67
154.10	8.06	7.75
146.16	8.06	8.83
134.96	8.06	12.98
119.08	8.06	20.98
107.40	8.06	36.98
105.07	8.06	1466.95
Cycle No. -2-		
118.45	11.29	0.000
248.58	12.90	0.366
310.14	12.90	0.616
346.93	14.51	1.099
412.15	16.12	1.332
443.31	17.74	1.448
334.75	16.12	1.698
313.36	14.51	3.031
304.50	14.51	4.347
283.51	14.51	10.680
259.26	14.51	27.680
237.81	14.51	57.680
213.10	14.51	117.680
182.29	16.12	207.680
165.51	16.12	387.680

SAMPLE NO. 3 (cont'd.)

159.91	16.12	1077.680
153.85	16.12	1257.680
151.52	16.12	1377.680
Cycle No. -3-		
155.69	17.740	0.000
157.56	17.740	0.750
252.61	19.350	0.980
363.48	20.960	1.096
477.76	22.580	1.229
519.05	22.580	1.345
596.66	25.806	1.461
488.68	24.190	1.577
467.72	24.190	1.943
466.29	24.190	3.026
423.93	24.190	5.159
399.24	24.190	9.159
376.41	24.190	15.159
347.53	24.190	28.159
325.17	24.190	43.159
302.34	24.190	58.159
284.64	24.190	83.159
262.27	24.190	113.159
233.86	24.190	173.159
204.51	24.190	263.159
186.34	24.190	383.159
163.98	24.190	653.159
143.01	24.190	953.159
133.70	24.190	1103.150
132.77	24.190	1403.150
Cycle No. -4-		
135.09	24.19	0.000
166.72	27.41	0.980
363.19	29.03	1.100
484.18	30.64	1.216
541.82	32.25	1.332
613.50	32.25	1.465
469.20	32.25	1.948
445.46	32.25	3.148
422.19	32.25	5.514
401.71	32.25	8.614
377.04	32.25	14.614
354.23	32.25	24.614
309.54	32.25	58.614
285.80	32.25	88.614
266.72	32.25	118.614
229.01	32.25	238.614
202.95	32.25	448.614

Table C-2 (cont'd.)

SAMPLE NO. 3 (cont'd.)

181.53	32.25	658.614
179.64	33.87	1108.614
178.25	33.87	1168.614
172.66	33.87	1228.614
168.94	33.87	1288.614
164.31	33.87	1348.614
End of Cycle No. -4-		
168.7	35.48	0.00
365.51	41.93	0.233
700.80	48.38	0.466
Total Time		5596.86

Table C-3: Sieve Analysis for Ottawa Sand Used in Thermal Tensile, and Stress Relaxation Tests.

U.S. Standard Sieve Number	Percent Finer by Weight
30	96.00
40	47.98
50	20.44
70	10.36
100	3.26
140	0.56
200	0.07
Pan	0.00

Table D-1: Air Temperature at Fargo, North Dakota (2-3 February, 1974)

Hour		Air Temperature + (°F)
00		03
03		03
06		03
09		06
12	2 Feb., 1974	06
15		05
18		-09
21		-21
00		-23
03		-26
06		-23
09	3 Feb., 1974	-25
12		-17
15		-14
18		-20
21		-26

+ Data from Local Climatological Data
U.S. Department of Commerce